DAMAGE AND REPAIR EVOLUTION OF COLD FORMED LINEPIPE STEEL

By

Huan LI

A thesis submitted to

The University of Birmingham

For the degree of

DOCTOR OF PHILOSOPHY

School of Mechanical Engineering

College of Engineering and Physical Sciences

The University of Birmingham

October 2009

UNIVERSITY OF
BIRMINGHAM

University of Birmingham Research Archive

e-theses repository

This unpublished thesis/dissertation is copyright of the author and/or third parties. The intellectual property rights of the author or third parties in respect of this work are as defined by The Copyright Designs and Patents Act 1988 or as modified by any successor legislation.

Any use made of information contained in this thesis/dissertation must be in accordance with that legislation and must be properly acknowledged. Further distribution or reproduction in any format is prohibited without the permission of the copyright holder.

SYNOPSIS

The main aim of this research is to model the internal micro damage accumulated during cold deformation and the degree of reduction of damage that can be achieved by heat treatment of linepipe steel. A set of unified viscoplastic constitutive equations was developed to simulate microstructural evolution and the effect on mechanical properties due to cold deformation followed by annealing. In addition, practical experiments have been performed to validate the constitutive equations.

Firstly, the industrial motivation for the project was previewed and damage-modelling techniques were reviewed to identify the research objectives. A group of interrupted uniaxial tensile tests were conducted to study the effect of different annealing times on reducing the degree of damage and improving mechanical properties of a cold formed single phase linepipe steel. From the experimental results, it was observed that healing by subsequent annealing enables a significant improvement in the mechanical properties of the deformed steel that has experienced only light damage, but has no significant effect on heavily damaged steel.

Following this, a set of constitutive equations describing accumulation and annihilation of dislocations, grain size evolution, recrystallisation, plasticity induced damage and their effects on viscoplastic flow of materials was developed, for uniaxial stress conditions and by numerical integration experimental results were used to determine material constants for these equations, for the particular steel.

Secondly, the constitutive equations were expanded to enable damage nucleation, growth and plastic flow to be predicted for various stress states. The constitutive equations were implemented in a commercial FE solver (ABAQUS) using the VUMAT user-subroutine. The numerical results reproduce the essential features of necking phenomena and provide a physical insight into damage evolution within a tensile test-piece under given necking conditions.

Dual phase steel is of greater importance industrially, than a single phase steel, but because of the greater complexity in its microstructure, the development of microstructural constitutive equations for it is very difficult. Thus, in this work, some knowledge of damage initiation in a dual phase steel was obtained by practical investigation of microstructure. It showed that damage is due to ductile cracking characterised by the nucleation of micro-voids near the ferrite-pearlite interface. Using the mesoscopic modelling technique, by simulation, it was possible to determine likely sites for damage initiation.

ACKOWLEDGEMENTS

I extend gratitude to my university supervisors Prof. J. Lin and Prof. T. A. Dean for their support and advice during the project.

Corus R, D & T provided the industrial problem, has helped steer the project with good advice and supplied the test material. Particularly, Dr. S. Wen and Mr A. C. Bannister are thanked for their academic assistance during this research.

I thank my colleagues and friends for their kind advices and assistance during this work.

Finally and very importantly, I would like to thank my wife, parents and lovely newborn son, for their love, support, encouragement and tolerance throughout the years of my research.

CONTENTS

NOMENCLATURE

ε_T	Total strain
ε_e	Elastic strain
ε_p	Plastic strain
ε_f	Strain to failure
σ	Stress (MPa)
σ_{ij}	Cauchy stress (MPa)
σ_y	Initial yield stress (MPa)
σ_e	Equivalent stress (MPa)
σ_H	Hydrostatic stress (MPa)
σ_1	Maximum principal stress (MPa)
σ^{dev}	Stress deviator tensor (MPa)
k	Yield stress (MPa)
K	Strength factor (MPa)
$\hat{\sigma}$	Internal stress (MPa)
D_T	Total damage
D_N	Damage nucleation variable
D_G	Damage growth variable
$\mathbf{D}$	Damage tensor
$\dot{D}^*$	Damage rate considering stress state
f	Current void volume fraction
f_{growth}	Void volume fraction growth
f_{nucl}	Void volume fraction nucleation
f_c	Critical damage level
d_0	Grain size dependence (μm)
d	Average grain size (μm)
d_{dia}	Original diameter of a round test-piece (mm)

Δd_{dia}	Variation of diameter (mm)
$d_{dia}^{\ x}$	Diameter at x position (mm)
d_{ref}	Diameter at reference position (mm)
ρ	Dislocation density
$\overline{\rho}$	Normalised dislocation density
$\overline{\rho}_c$	Normalised critical dislocation density
ρ_i	Initial dislocation density
ρ_c	Critical dislocation density
l	Dislocation mean free path
E	Young's modulus
a_1, a_2, n_1, n_2, n_3	Damage growth material constants
G_1, G_2, ψ_1, ψ_2	Material constants in grain size evolution
x	Recrystallisation onset parameter
X_1	Material constants in recrystallisation onset
S	Recrystallised volume fraction variable
H, λ_1	Material constants in recrystallisation
k_1, δ_1	Material constants in dislocation accumulation
C_r, δ_2	Dislocation recovery material constants
C_S	Recrystallisation recovery material constants
R	Isotropic hardening variable
B	Isotropic hardening material constant
γ, n_d	Material constants exponents
n	Strain hardening exponent
N_x	Necking variable at x position
M	Texture of the polycrystalline structure
G	Shear modulus
b	Burger's vector
α	Material constant
K_1, K_2	Material constants

r	Static recovery coefficient
r_0, U_0, K_B, β	Static recovery coefficient material constants
T	Temperature
T_m	Material-melting temperature
σ_{surf}, τ, d^*	Material constants
F_R	Driving pressure for recrystallisation
p, q	Material constants in Avrami equation
Z	Zener-Hollomon parameter
C, a, e, c	Material constants
N, f_1	Grain size evolution material constants
m, γ_0	Material constants in grain growth equation

LIST OF ILLUSTRATIONS

LIST OF TABLES

CHAPTER 1

Project preview

1.1 Introduction

In this chapter a perspective of the global industry of steel manufacture is given, with a special focus on linepipe steel. The current linepipe cold forming process is described and the aim of the research is defined.

1.2 The global steel industry

Steel has high strength, good formability and machinability and iron, its main constituent, is relatively abundant in its natural form. In terms of strength per unit currency it remains the most inexpensive metals. Alloying elements and heat treatment provide a wide variety of mechanical properties and level of corrosion resistance, making it exceptionally versatile. New steel products, such as foams, may even see steel becoming competitive in weight sensitive applications currently dominated by aluminium, magnesium and titanium.

Because of the critical role played by steel in infrastructural and overall economic development, steel industry is often considered to be an indicator of economic progress. However, the global steel market is changing rapidly. The economic boom in China and India has caused a massive increase in the demand for steel in recent years. Between 2000 and 2005, world steel demand increased by 6%. Since 2000, several Indian and Chinese steel firms have risen to prominence like Tata Steel (which bought Corus Group in 2007), Shanghai Baosteel Group Corporation and Shagang Group.

ArcelorMittal is however the world's largest steel producer (Fig. 1.1). At the time of writing in 2009, global steel output was 1.3267 billion tons, a drop of 1.2 percent over 2007 and the first-ever decline in the past two decades since 1988 (ISSB, 2008), due to the world economic downturn. In this difficult environment, companies must choose to differentiate on quality or price of product. Given the high cost of UK labour and the trend within UK manufacturing to focus on high value added products it makes most sense to concentrate on providing superior grades of steel and to optimise the production process of the products.

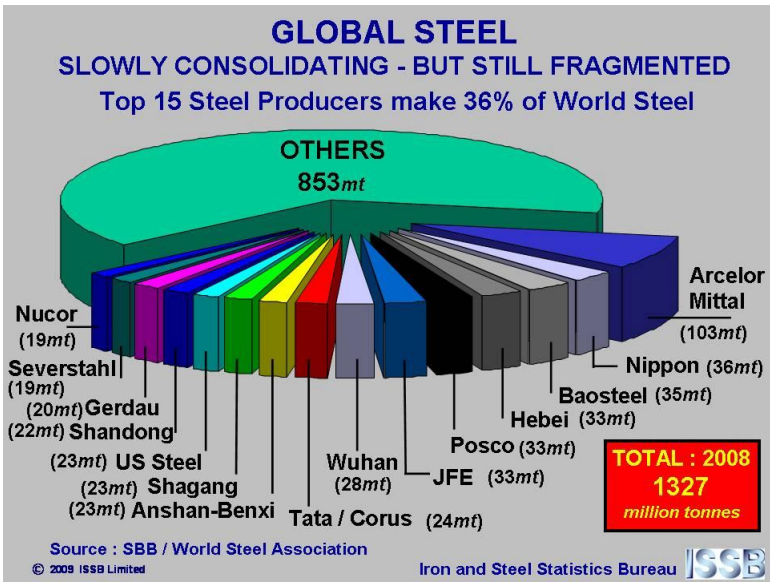

Fig. 1.1. Global steel producers (2008). (Source: ISSB 2008)

Corus is Europe's second largest steel producer with annual revenues of around £12 billion and a crude steel production of over 20 million tonnes, primarily in the UK and the Netherlands. A variety of innovative solutions are supplied to a broad range of markets, including: construction, automotive, packaging, aerospace, energy and engineering industries. However, with increasing competitiveness between steel

producers and rising quality demands from customers, it is required that raw materials of consistent high quality be produced. One factor undermining high quality is damage that can arise during forming operations; the ability to predict and obviate this is of great importance. A predictive ability would allow optimisation of forming processes and one way of obtaining this is to use finite element simulation. Material and process simulation can be used to determine process conditions to decrease the likelihood of poor quality material. Also, simulation can be used to reduce cost, improve the product and ultimately increase profitability by the ability to operate right first time processes. In an increasingly safety conscious, liability mindful and information ready world, quoting as-supplied micro-damage levels of steel products to customers can offer customers peace of mind.

1.3 Industrial background

1.3.1 Linepipe

As global demand for key energy sources such as oil and gas increases, a large number of linepipes is needed for extraction and distribution. Corus is one of the world leading pipe suppliers with a long and successful track record in the energy industry. Corus offers a range of Oil Country Tubular Goods (OCTG), linepipe, pipe-in-pipe insulation, pipe coatings, and process pipe for the Offshore, Onshore, Process Plant and Petrochemical industries. Fig. 1.2 shows cold formed offshore linepipe and its installation offshore.

Cold formed pipeline

Installation of offshore pipeline

Fig. 1.2. Cold formed offshore linepipe and an example of its use. (Corus UK)

In Corus, offshore linepipes are cold formed on an 84" Pipe Mill using the UOE process (Wen et al., 1999) with hot rolled steel plates as raw material, as shown in Fig. 1.3. During the manufacturing process, edge preps are first machined at the two long edges of the plate in order to better accommodate the submerged arc welding (SAW) later in the process. The edge-prepped plate is then incrementally fed into a Crimping press to have the long edges crimped. After that, the plate is then formed into a U-shaped skelp in a U-ing press. Following this, the U-skelp is then further deformed in an O-ing press to form an O-shaped pipe with a seam, which is then welded together using a two-pass submerged arc welding (SAW) process. The SAW pipe is then incrementally expanded along the length with a mechanical expander in order to achieve the specified diameter and roundness. The various testing (hydrostatic, ultrasonic and radiographic) are carried out to inspect the quality of pipeline prior to service.

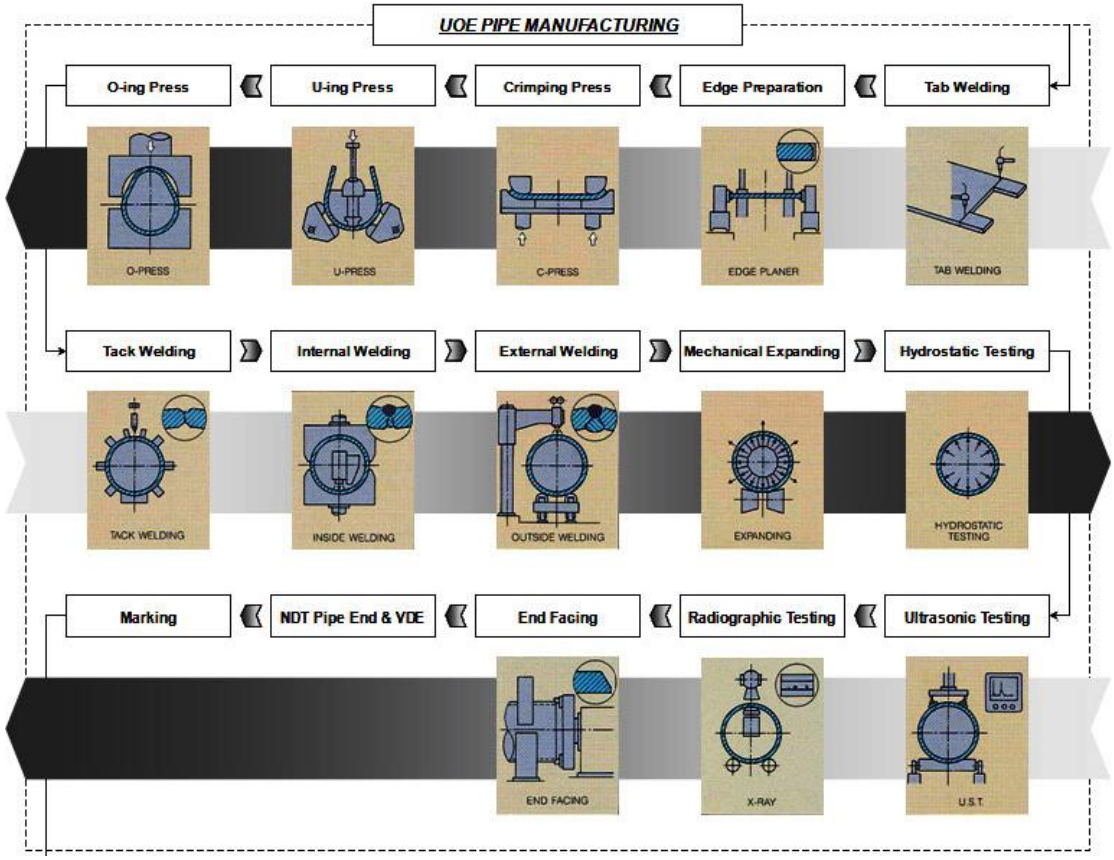

Fig. 1.3. Linepipe manufacturing process using the UOE method (Corus UK).

1.3.2 Problem description

An ideal steel product could be optimised to perform exceptionally at each stage of the production process and during its working life. Cold forming has unique advantages that enable metals to be processed to produce microstructures that enhance mechanical properties, such as strength and fatigue life of components in service. On the other hand, large plastic deformation arising in forming processes may create defects, which reduce ductility and strength and also fatigue and creep lifetime. Formed linepipe needs to ensure the optimal design with collapse and fatigue resistance in high pressure and ultra deep environments as major considerations.

Complex stress-strain paths and multiple deformation processes are encountered in forming engineering components. Micro defects can be created and accumulated during the processes, which cannot be directly investigated using simple uniaxial stress-strain curves. The nucleation and growth of these defects, known as micro-damage, adversely affect the mechanical properties of formed parts. The relationship between micro-damage and mechanical properties has not been quantified and there are no criteria for process design and quality assessment. Over the last 50 years work has been carried out to identify the source of damage during cold forming processes; this is reviewed in Chapter 2.

1.4 Objective and approach to research

The aim of this research program is to understand the mechanisms of damage and repair evolution occurring within the linepipe steel during cold deformation and subsequent heat treatment. The primary objective is to develop unified mechanisms based viscoplastic-damage constitutive equations for modelling microstructure and damage evolution in cold deformation and subsequent annealing.

In order to achieve the objective, the approach to research has been determined. Deformed specimens are studied at a microscopic level for evidence relating to the mechanisms of deformation and eventual macroscopic mechanical properties and material failure. Constitutive modelling techniques are used to define the material behaviour in a mathematical sense. Each key mechanism is represented by a governing equation, which may be time dependent, and related to other influencing mechanisms. Overall, a generic model of material evolution is determined by integration of the

unified constitutive equation set, with the constants being determined by optimisation, with reference to practical results obtained by experiment. To determine the evolution of microstructure and mechanical properties in a forming process the equation set is incorporated into the ABAQUS finite element package for process simulation.

CHAPTER 2

Advances in the understanding of damage and damage healing processes

2.1 Introduction

This chapter starts with a brief introduction to the mechanisms of micro damage. Then various types of micro damage that have been observed are described followed by an evaluation of common damage modelling techniques. Finally, a brief review of micro damage healing features through heat treatment is presented, in order to identify the damage tolerance of the steels.

2.2 Damage phenomena and mechanisms

Metals undergoing plastic deformation will suffer from a degrading microstructure. Discreet voids or cracks tend to nucleate and grow within the material and eventually these defects coalesce to form macro cracks, leading to material failure (Lin et al., 2005). The collective name for these degrading defects is damage (Foster, 2007).

Damage in metals is mainly characterised into three stages: nucleation, growth and coalescence of micro-cracks and cavities (Chaboche, 1987), as shown in Fig. 2.1. They may be described as follows:

Nucleation: Decohesion at high stress points (such as grain boundaries, inclusions, impurities, etc.) causes cracks or voids to nucleate within the material.

Growth: As material surrounding the damage site plastically deforms, the damage feature will enlarge. During this stage the macro flow stress of the material will be reduced due to the reduced load bearing area at the micro scale.

Coalescence: At a critical damage level individual damage features meet or material between damage features becomes significantly overstressed. This causes coalescence by inter-damage cracking. The coalesced cracks quickly grow to form macro scale cracks.

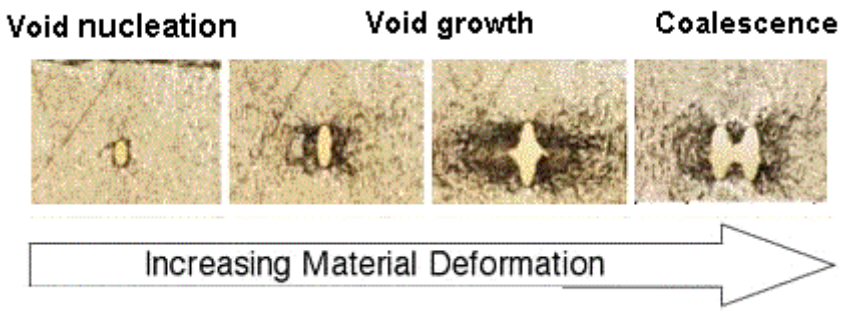

Fig. 2.1. The three stages in damage development (source: http://www.cavs.msstate.edu).

From a macroscopic viewpoint, damage has an important influence on the mechanical behaviour of processed metals, as internal or external cracking results in lower load bearing capacity and eventually complete failure. From a microscopic viewpoint, impurities (distributed defects) in materials act as crack initiation sites, (Lemaitre, 1985). Damage evolution is strongly influenced by the dominant deformation mechanism and processing condition.

2.3 Types of damage

To understand the damage phenomena and mechanisms, which will lead to the development of damage constitutive equations for modelling damage evolution in viscoplastic deformation processes, literature has been reviewed and an analysis given below. Damage is always nucleated at discontinuities in the microstructure within the material and several different damage mechanisms have been observed. Typical damage mechanisms and associated deformation mechanisms occurring at four temperature conditions are considered, based on melting temperature T_m.

2.3.1 Ductile damage ($T < 0.3T_m$)

The cold working of metals is often used to work harden material whilst forming the desired shape. The phenomenon of nucleation and growth of damage induced by large plastic deformation in metals, known as ductile damage, has been extensively studied by Lemaitre (1985). Normally ductile damage takes place within a low temperature range (Thomason, 1990). Control of damage is essential for cold forming because there is often no post-processing to remove cracks or defects that have been created.

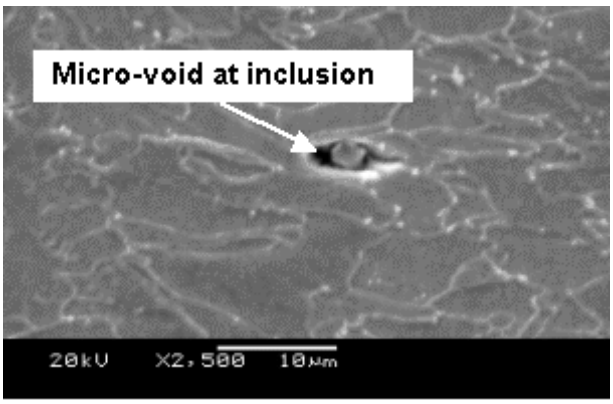

Fig. 2.2. Damage surrounding inclusion in cold deformation.

Ductile damage is associated with point defects within a metal, such as inclusions and pores (Tvergaard, 1982; Lin et al., 2005). From the microscopic point of view, the key role played by microvoids in ductile fracture has been pointed out by McClintock (1968) and Rice and Tracy (1969). At large values of deformation, it has been discovered that void nucleation and growth around inclusions are the dominant damage mechanisms in ductile fracture (Bonora, 1997), as shown in Fig. 2.2. Based on an averaging technique, the characteristics of a volume of material have been considered as an aggregate of voids and rigid plastic material rather than a polycrystalline aggregate (Needleman, 1987). Voids were assumed spherical or cylindrical in order to approximate their real shape. Microvoids start at the ductile matrix/brittle inclusion interface and propagate when the local stress field is strong enough either to debond or break the particle. Subsequently, voids grow until they link by coalescence when the ligament between them has reached a critical length.

2.3.2 Creep damage ($T > 0.3T_m$)

Creep is the continuing elongation of a component under a static stress maintained for a period of time. Deformation by creep is often associated with high temperature, although creep behaviour can occur in cold conditions over very long time periods (Brust and Leis, 1992). The imposed stress is generally low, certainly less than the yield stress of the material and the material deformation rate is relatively low (Zhang and Lee, 1993). The deformation mechanisms are mainly grain boundary sliding and mobile dislocation multiplication (Tvergaard, 1990).

Subjected to creep deformation conditions, an accumulation and growth of micro-voids in metals take place. This is so-called “creep damage” and is time-dependent (Lemaitre, 1984). According to Cocks and Ashby (1982), creep damage loosely includes any type of structural change resulting from adverse creep deformation. Creep damage has been experimentally observed for most metals and alloys (Ashby and Dyson, 1984). Cavity nucleation and growth occur at grain boundaries due to grain boundary diffusion, as shown in Fig. 2.3 for example, dislocation multiplication and creep of the surrounding matrix (Dyson, et al., 1981; Ashby and Dyson, 1984). Coalescence of these cavities, leads to micro-cracks, and finally intergranular creep fracture occurs as the micro-cracks link up. In cases where diffusion is the dominant contribution to the growth of cavities, the rate of growth is often constrained by the rate of dislocation creep of surrounding material (Cocks and Ashby, 1982).

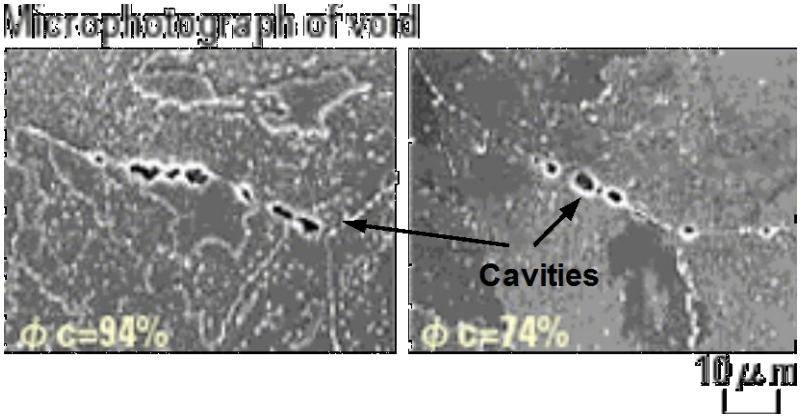

Fig. 2.3. Creep voids formed at grain boundaries of an alloy. (source: www.bhk.co.jp)

2.3.3 Superplastic type damage ($T > 0.5T_m$)

Pearson (1934) published a landmark paper detailing observations of extreme ductility within a Bi-Sn alloy. The superplastic effect occurs under warm to hot deformation

conditions, where a small and uniform equiaxed grain structure is present. Industrial applications include the forming of aluminium components for aerospace and automotive applications, where sheet material can be formed into intricate shapes (Cheong, 2002). Plastic deformation occurs by grain boundary sliding and grain rotation, as a result of which grains remain equiaxed throughout deformation (Ghosh and Hamilton, 1979).

Superplastic damage occurs when there is a mismatch between interacting grains. As a grain passes over a neighbouring grain, some accommodation is required below the grain boundary in order for the grains to remain in contact (Cheong, 2002; Perevezentsev et al., 1992). If the accommodation process fails, stress in the grain boundaries cannot be relieved resulting in the formation of a void. Cheong (2002) has demonstrated that similarities between creep and superplastic deformation make it possible to model superplastic damage using similar concepts to creep damage.

2.3.4 Hot working damage ($T > 0.6T_m$)

Many hot deformation processed are carried out at high temperatures ($T > 0.6T_m$). For most hot metal forming operations, hot work damage is associated with both grain boundaries and inclusions, depending on strain rate. For most hot metal forming operations strain rate is high and voids form at debonded inclusions and grow during subsequent straining (Farrugia, 2006; Liu et al., 2006). But in some regions of deformation strain rate may be low, grain boundaries can become mobile, leading to creep and superplastic type damage (Lin et al., 2005; Lin et al., 2007). Therefore it is possible that two types of damage take place simultaneously during hot deformation.

However, a particular damage mechanism can always be identified as the dominant one at each stage of deformation (Liu, 2005).

2.3.5 Summary

Damage phenomena over all metal forming temperature ranges have been experimentally observed in the work of many researchers. The known damage mechanisms and damage phenomena subject to typical loading conditions are reviewed. The study of this thesis is focused on the deformation condition at room temperature. Ductile damage is a major issue at low temperatures. Therefore, the state of art with regard to cold deformation mechanisms and ductile damage phenomena need to be investigated. The experimental investigation will provide further essential information on formulating and calibrating damage constitutive equations. Ductile damage mechanisms modelling are the basis of formulating unified viscoplastic damage constitutive equations, which are briefly reviewed and discussed in following section.

2.4 Damage modelling

2.4.1 Introduction

The development of damage affects the properties of a material in various ways. A damage model is used to predict one, or ideally all, of the following effects that damage has on a material (Foster, 2007):

Material degradation: by calculating the volume of damage within the material, the extent to which the microstructure deviates from the non-damaged state is assessed. Material softening: Macro reduction in flow stress due to a reduction in load bearing

area caused by micro voids. Failure point: The ability to predict material failure facilitates to creation of safe process route. Damage interaction: The interdependence of different damage mechanisms.

In the majority of damage models developed in past years a damage area variable is used to represent the state of damage. The concept is simple: a single representative damage variable is calculated as the ratio of damage area to total area for a given representative cross-sectional area of the material (Fig. 2.4). Here, a rectangular cross-section of material is considered, with dimensions a and b. D is the damage index, A_D is the damaged area, A_E is the effective or net area and $A_T = A_D + A_E$ is the total area. Thus, a damage value D of 0 indicates no damage, and a value of 1 indicates total material failure.

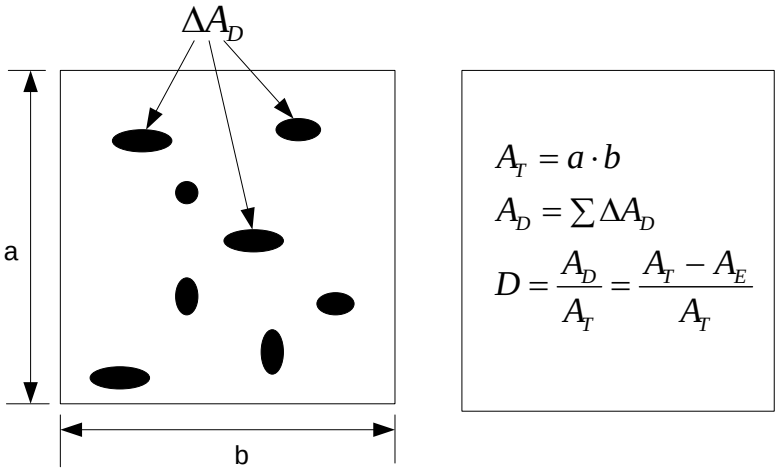

Fig. 2.4. The damage variable by area.

2.4.2 Ductile damage modelling

The mathematical modelling of internal damage cavities created during cold deformation conditions was initially investigated by McClintock (1968), who

developed micro-mechanical analysis for the growth of idealised cylindrical cavities within the material. A year later Rice and Tracey (1969) developed models for void growth through detailed theoretical analysis of the surrounding stress field. Clift et al. (1990) have made a comparison of many ductile fracture criteria for various cold metal forming operations.

Representative Volume Element (RVE) models, the most popular of which is Gurson's (1977) have been developed by analysis of the plastic potential surrounding a spherical or ellipsoidal shape. Gurson (1977) proposed a porosity based model where the yield function for ductile materials is modified by the presence of voids: as the porosity term increases, material softens and loses its capability to carry loads. Gurson model refers to an approximate yield condition, of the form $\Phi(\sigma^{ij}, \sigma_y, f) = 0$, for a porous ductile material, where σ^{ij} is the average macroscopic Cauchy stress tensor, σ_y is an equivalent yield stress, and f is the current void volume fraction. However, Gurson's theories generally under predict the final stages of damage due to the lack of a coalescence criterion. Needleman and Tvergaard (1984) modified the Gurson model in order to take into account an acceleration of the failure process induced by void coalescence. The modification significantly increased the model's ability to predict the damage fraction and damage related material softening close to the failure point.

Needleman and Tvergaard (1984) introduced an extra contribution (f^*) to be added to the Gurson (1977) expression:

$$\Phi = \left(\frac{\sigma_e}{\sigma_y}\right)^2 + 2q_1 f^* \cosh\left(\frac{\sigma_{kk}}{2\sigma_y}\right) - (1 + (q_1 f^*)^2) \qquad \textbf{2.1}$$

where the macroscopic Mises stress is of $\sigma_e = \sqrt{\frac{3}{2} s_{ij} s_{ij}}$, in terms of the stress deviator $s_{ij} = \sigma_{ij} - \frac{1}{3}\sigma_{kk}$, and $\sigma_{kk}/3$ is the macroscopic mean stress. For $f^* = f$ and $q_1 = 1$ the expression (2.1) is that derived by Gurson (1977) based on a rigid-perfectly plastic upper bound solution for spherically symmetric deformations around a single spherical void.

The modification of the yield condition, to account for final material failure, is introduced through the function $f^*(f)$ specified by Needleman and Tvergaard (1984) as:

$$f^* = f \qquad \text{for } f \le f_c$$

or

$$f^* = f_c + K(f - f_c) \qquad \text{for } f > f_c \qquad \textbf{2.2}$$

Where

$$\dot{f} = \dot{f}_{growth} + \dot{f}_{nucl} \qquad \textbf{2.3}$$

for the change of void volume fraction during an increment of deformation. Where $(\cdot)$ denotes partial differentiation with respect to time. In the present investigation an alternative failure model is employed, in which the approximate yield condition

$\Phi = 0$ is modified for $f > f_c$, f_c representing the critical damage level at which coalescence will proliferate. It is noted that the ultimate value, $f^* = f_u^*$ at which the macroscopic stress carrying capacity vanishes, is given by $f_u^* = 1/q_1$, according to equation 2.1. Plots of the yield function in Fig. 2.5 illustrate how the material loses its stress carrying capacity for $f^* / f_u^* \to 1$.

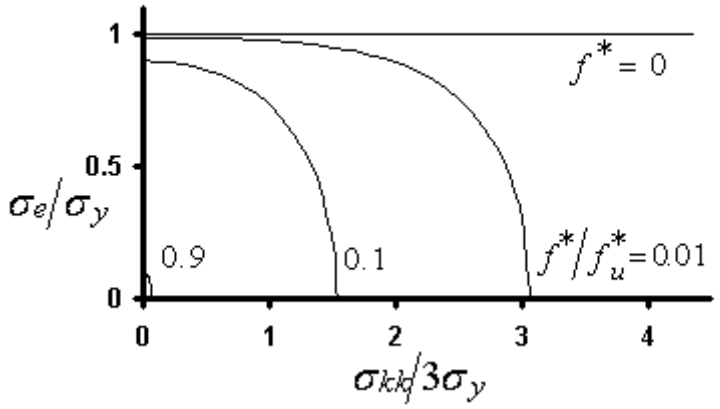

Fig. 2.5. Yield surface dependence on the function f^* in equation 2.1.

The functions for damage nucleation and growth are given by thermodynamically calculated single void models (Tvergaard and Needleman, 2001). The physical yield point of the sound material is assumed to be unaffected by damage, only the macro flow stress is corrected to account for damage. Thus the yield is no longer the macro continuum material yield point, but the yield of undamaged material. This allows the Gurson model to remain separate from other internal variables, which may influence the dynamic yield point (such as material hardening, recovery and recrystallisation, viscoplasticity). The RVE modelling technique is especially useful in situations where continuum theories are insufficient (Li and Steinmann, 2006).

Recent adaptations to the models have included the inclusion of equations to consider the presence of an inclusion within a damaged void (Bordreuil et al., 2003; Maire et al., 2005), extensions to consider void shape and further improve void coalescence (Pardoen and Hutchnson, 2000) and strengthening the two-directional coupling relating damage accumulation and material flow, which is only weakly coupled in the Gurson model (Abu Al-Rub and Voyiadjis, 2003).

Liu et al. (2005) have produced a complex but logical model capable of modelling dislocation build up and associated material hardening, dislocation recovery and recrystallisation, grain growth and ductile damage. The model has phenomenological-based nucleation and growth parts to damage mechanism, but coalescence is not treated as a separate mechanism, rather as a rapid growth of voids. It is this style of modelling that will be adopted in the current work, with the intention of expanding to new materials.

2.5 Damage healing mechanisms

It is known that heat treatment is widely used in the cold forming / forging industry for eliminating work hardening, improving ductility and removing residual stress. If cold formed steel is subsequently heated to a sufficiently high temperature, solid state diffusion can provide a mechanism to re-arrange microstructure into configurations of low energy (Humphreys and Hatherly, 1996). Hence, residual stress within a deformed component can be reduced or eliminated by applying heat treatment after forming. In addition, the level of dislocation density may also be reduced, allowing recovery in mechanical properties.

It is well known that the mechanical properties of steels are closely related to their deformation history and microstructure. In metal forming processes, internal micro-cracks may occur because of inhomogeneous deformation. Although the propagation of cracks is restrained in hot forming because a simultaneous healing process exists (Shapiro and Dieter, 1970), some cracks might remain in the formed materials. The healing process does not exist during cold deformation. Cold forming processes normally increase dislocation density and micro-damage, which can reduce the reliability and durability of products and lead to failure during subsequent forming operations and/or in service (Chaboche, 1987).

Heat treatment may heal internal cracks existing in formed metals. Griffith (1920) proposed that cracking is not a "reversible" operation. However, a very small crack may be healed if the maximum temperature of the heat treatment is sufficient to bring the atoms on either side of the crack to within a range for bonding by thermal agitation (Wei et al., 2006). Kumanin et al. (1995) analysed the damage evolution in metals, and indicated that many types of heat treatment methods can be used to decrease the amount of defects arising after a long-term operation at high temperature. Han et al. (1997) investigated crack healing in 20MnMo steel. And Wei et al. (2004) revealed that a crack could be healed in plain carbon steel at elevated temperature. Han et al. (1997) concluded that the damage healing process was mainly controlled by the diffusion and migration of metal atoms, and consisted of two steps, damage filling and grain growth. Damage healing due to the application of a compressive stress state has been reported at high temperatures (Bogatov, 2003) and crack closure has been accounted for in some FE simulations using damage models (Andrade Pires et al., 2004).

Recrystallisation of alloys eliminates cracks by moving grain boundaries (Liu et al., 2006). Based on the review of damage healing mechanisms described above, two forms of damage healing mechanisms may occur following annealing. Firstly, under certain circumstances, for example a recrystallisation front passing over micro-voids, damage may be eliminated completely. Secondly, if a grain boundary migrates over an area containing small voids due to grain growth, the voids may become locked inside the grains, where stress will be dispersed around the matrix discontinuity. The physically macroscopic and microstructural features associated with recrystallisation and recovery, including grain evolution, can be integrated to provide an overall understanding of damage modification during heat treatment. However, it still remains uncertain how the damage healing mechanism affects the mechanical response. And no existing model can describe the effect of time and amount of damage on damage healing. Thus, further experimental investigation is needed. In this work damage healing mechanisms are coupled within a viscoplastic constitutive equation set to simulate observed characteristics.

2.6 Summary

Damage phenomena are an on-going problem in large plastic deformation. It is insufficient to assume a general model will be adequate to predict the damage mechanisms in a specific material, especially if the model has been developed for dissimilar deformation conditions. Typical damage phenomena have been reviewed with respect to low temperature ranges. Also, a detailed understanding of the specific method of damage nucleation and growth is required, which is unique to the material and deformation conditions being considered. In order to understand these mechanisms,

it is necessary to perform experimental tests that characterise the material and in light of damage, conduct additional tests that reflect the deformation conditions found during cold forming operations.

Complex damage healing phenomena for cold-formed material during heat treatment have been discussed. Damage healing is now considered to show promise in the recovery of the mechanical properties of the damaged materials. Thermal or mechanical treatment provides the driving force to result in the healing of damage, which provides a foundation for developing a set of unified mechanism based constitutive equations to model damage evolution during cold forming and subsequent heat treatment.

CHAPTER 3

Microstructure evolution during heat treatment of cold-formed steel

3.1 Introduction

In this chapter, microstructural evolution and recovery of mechanical properties during heat treatment of cold worked steel, are discussed. Developments in modelling dislocation evolution, recrystallisation and grain size during heat treatment are reviewed. Finally, a set of mechanism based constitutive equation is developed, to model microstructural evolution during heat treatment for linepipe steel.

3.2 Mechanisms of mechanical property recovery by annealing

As mentioned in the previous chapter, heat treatment is widely used in the cold forming / forging industry to eliminate work hardening, increase ductility and remove residual stress. It is well known that the mechanical properties of linepipe steels are closely related to their deformation history and microstructure. The phenomenological approach has been used to create a model, which provides insight into the microscopic mechanisms that act to cause a change in the macroscopic properties of an alloy. In the case of cold forming and subsequent heat treatment, understanding of microstructural evolution and the relation between microstructure and macroscopic response of a material may be used to optimise workability during production and ensure consistency in the microstructure of the finished product.

In order to model the effects of microstructural evolution on mechanical property recovery, the mechanisms and phenomena of change, at different stages during cold

forming and subsequent annealing need to be understood. Mechanical properties such as strength, ductility and toughness, are directly related to the microstructure of a metal. Hence, mechanical property recovery is a function of microstructural evolution during annealing. Typical relationships between grain structures, ductility, yield strength and annealing time for cold deformed steel are shown in Fig.3.1.

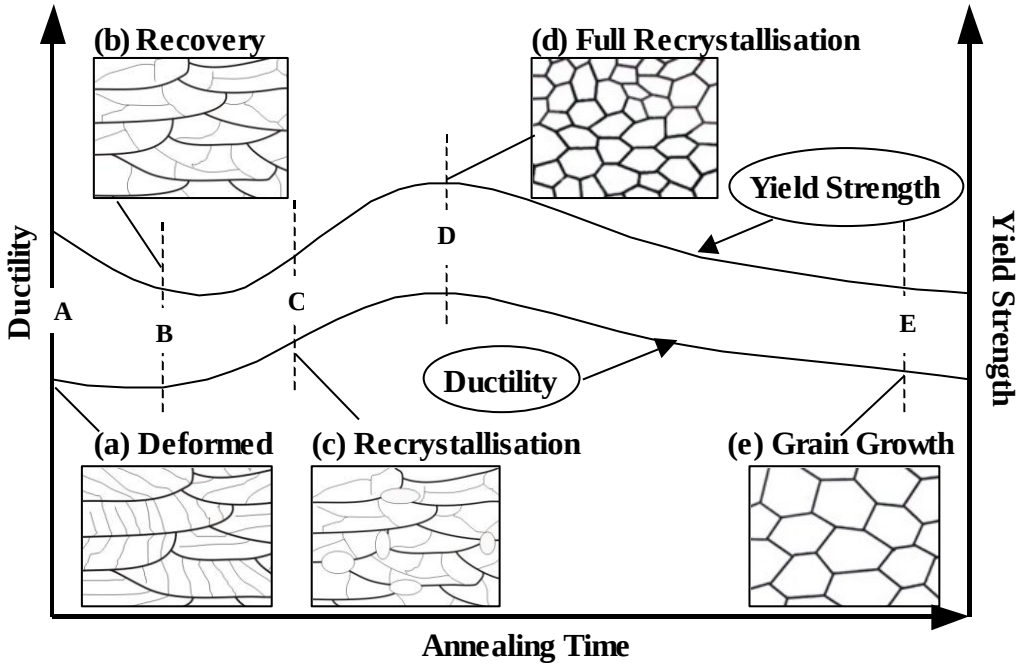

Fig. 3.1. Schematic diagram showing the variations of microstructure and mechanical properties of a pre-deformed material at different stages (A-E) of annealing process (a) Deformed state, (b) Recovery, (c) Partially recrystallisation, (d) Fully recrystallisation and (e) Grain growth (Humphreys and Hatherly, 1996).

Position A in Fig. 3.1 represents the state of cold deformed steel at the beginning of the annealing process. The microstructure at this stage is shown schematically in Fig. 3.1(a), where the grains are elongated and the dislocation density is high. This results in high strength due to work hardening and low ductility due to high dislocation density. The microstructural evolution during recovery is relatively homogeneous and does not

usually affect the boundaries between the deformed grains. The microstructure of the material during the initial stage of the high temperature annealing process (position B), is shown in Fig. 3.1(b). Static recovery takes place by annihilation and rearrangement of dislocations. Also, yield strength decreases due to work hardening annihilation. Ductility does not change significantly because the grain size remains more or less unchanged.

With increasing annealing time, as at position C, in Fig. 3.1, static recrystallisation has occurred, and new dislocation-free grains are formed within the deformed structure. The result is a mixture of old grains and newly formed grains with a low dislocation density. Both yield strength and ductility of the material increase at this stage due to the new fine grains formed by recrystallisation and ductility can be higher than that of the original material, if micro-damage has been fully eliminated. Position D, Fig. 3.1(d), represents a more homogeneous and refined ferrite microstructure, which is produced with increasing annealing time. This shows that at full recrystallisation, ductility and yield strength reach their highest values, due to the fine uniformly arranged new grains. Position E represents the final stage of the annealing process, where further annealing causes static grain growth. At this stage the smaller grains are eliminated as the grain boundaries assume a lower energy configuration. The microstructure is shown schematically in Fig. 3.1(e). Both yield strength and ductility of the material decrease due to the increased average grain size. Detailed modelling of the phenomena described above based on continuum mechanics theories is described in the following sections.

3.3 Review of modelling approaches

The study of dislocation density evolution in cold deformation is becoming increasingly important. A number of investigations on the relationship between macroscopic non-elastic deformation and dislocation evolution have been reported (Bocher et al., 2001; Trivedi et al., 2004; Houtte et al., 2005; Zhang and Jiang, 2005; Mayama et al., 2007). The reversibility of dislocation structures has been studied and it was found that they are not completely reversible when the magnitude of the loading is changed from high to low (Zhang and Jiang, 2005). Mayama et al. (2007) concluded that a model of cyclic viscoplasticity considering subsequent viscoplastic loading must account for both macroscopic deformation behaviour and dislocation structures. Recently, experimental and theoretical investigations have led to the development of constitutive models considering the microstructure of materials (Estrin et al., 1998; Li et al., 2004; Uenishi and Teodosiu, 2004; Bucher et al., 2004; Brinckmann et al., 2006; Beyerlein and Tomé, 2008). Most of these physically based models are founded on the evolution of dislocation structures. Estrin et al. (1998) proposed a dislocation density based constitutive model and extended it to describe deformation of all hardening regions. In this model dislocation densities are divided into a high dislocation density phase (cell wall) and a low dislocation density phase (cell interior). The model has been used to describe dislocation density evolution for large deformations, with only a few material parameters.

Research has also been carried out on microstructural evolution of deformed steel during annealing (Kwiecinski and Wyrzykowski, 1993; Hoc and Forest, 2001; Martínez-de-Guerenu et al. 2004 (a)). Martínez-de-Guerenu et al. (2004 (a)) modelled the recovery at low temperature without recrystallisation taking place during annealing

of a cold rolled low carbon steel; while Kwiecinski and Wyrzykowski (1993) concentrated on the yield strength changes during annealing. A variety of computer models have been proposed in recent years for static recrystallisation, in particular Monte Carlo (MC) simulations (Srolovitz et al., 1988), cellular automata (CA) approaches (Marx et al. 1999; Hesselbarth and Göbel, 1991) and vertex models (Humphreys, 1997). Vertex models treat recrystallisation as a grain growth process, except that the deformed structure is essentially composed of low-angle boundaries. The MC models are essentially thermodynamic models that extrapolate a trajectory towards lower energy situations. The CA models are essentially kinetic approaches to the problem of recrystallisation, where the existence of a driving force is tacitly assumed and the microstructural evolution is traced over time. The mechanisms for microstructural evolution under variable conditions are fairly well understood. However, most of these models focus on one phenomenon, but the microstructural mechanisms associated with cold forming combined with subsequent annealing are different and more complex and a new approach is required. Below an approach is developed to model the effect of microstructural evolution on mechanical property recovery of cold formed and annealed, low carbon ferritic steels.

3.4 Modelling of microstructure evolution in cold forming and annealing

3.4.1 Modelling of dislocation density

During cold deformation, dislocation density ρ within the material changes, due to dislocation accumulation and dynamic recovery. The dislocation structure developed during plastic deformation constitutes a driving force for microstructural evolution, and dislocations mainly congregate on subgrain boundaries. A number of work hardening

models have been proposed (Sandström and Lagneborg, 1975; Kocks and Mecking, 2003; Zhao et al., 2004; Estrin, 1998), and a simple model developed by Kocks (1976) used to assess the influence of strain hardening and the accumulation of dislocations on the internal stress $\hat{\sigma}$ is:

$$\hat{\sigma} = \alpha G b \sqrt{\rho} \qquad \textbf{3.1}$$

Here G is the shear modulus, b is the Burger's vector and α is a material constant. Two concurrent effects determine the variation of dislocation density: storage and recovery. The increment of dislocation density $d\rho$ in the process of plastic deformation can be described by Kocks (1976):

$$\frac{d\rho}{d\varepsilon_p} = \frac{M}{bl} \qquad \textbf{3.2}$$

where $d\varepsilon_p$ is the true plastic strain increment, l is the dislocation mean free path and M defines the texture of the polycrystalline structure, which may be assumed constant (Nes, 1998). To consider the dynamic recovery, a dislocation density based evolution equation is expressed as (Estrin, 1996):

$$\frac{d\rho}{d\varepsilon_p} = K_1 \sqrt{\rho} - K_2 \rho \qquad \textbf{3.3}$$

The coefficients K_1 and K_2 in Equation 3.3 characterise the processes of dislocation storage and concurrent dislocation annihilation by recovery, respectively. Coefficient

K_2 represents a thermally activated process of dynamic recovery by dislocation cross-slip (low temperature) or dislocation climb (high temperature). For processes such as annealing, static recovery is significant. Thus an extra term, *r*, which is particularly used to model the dislocation recovery in the annealing process, is introduced in Equation 3.4 (Estrin, 1996):

$$\dot{\rho} = \left(K_1\sqrt{\rho} - K_2\rho\right)\dot{\varepsilon}_p - r \qquad \textbf{3.4}$$

The static recovery coefficient r is:

$$r = r_0 \exp\left(-\frac{U_0}{K_B T}\right)\sinh\left(\frac{\beta\sqrt{\rho}}{K_B T}\right) \qquad \textbf{3.5}$$

In the above equations the following additional constants and variable are introduced: activation energy U_0, material constant β, temperature T, constant pre-exponential factor r_0, and the Boltzmann constant K_B. Equations 3.4 and 3.5 enable the dislocation density evolution to be well modelled for a microstructure during cold plastic deformation and recovery.

The dominant deformation mechanism in cold forming is due to dislocation slip, and the density of dislocations increases rapidly with plastic strain. Higher plastic strain with higher stored energy results in static recrystallisation during a following annealing process. An equation has been proposed to describe the dislocation density evolution due to plastic deformation and dynamic recovery during annealing, static recovery and

recrystallisation under hot forming conditions, for a steel deformed in the austenitic state (Lin et al., 2005). The normalised dislocation density evolution is expressed as:

$$\dot{\bar{\rho}} = k_1 \cdot (1-\bar{\rho}) \cdot \left|\dot{\varepsilon}_p\right|^{\delta_1} - C_r \cdot \bar{\rho}^{\delta_2} - \frac{C_S \cdot \bar{\rho}}{1-S}\dot{S} \qquad \textbf{3.6}$$

where $k_1, \delta_1, C_r, \delta_2$ and C_S are material constants and $\dot{S}$ represents the evolution of recrystallised volume fraction. The normalized dislocation density varies from 0 to 1 and is defined by $\bar{\rho} = (\rho - \rho_i)/\rho$, where ρ is the current dislocation density and ρ_i is the dislocation density for the virgin material. The current dislocation density is always higher than, or equal to the virgin material dislocation density. The first term in Equation 3.6 represents the evolution of dislocation density due to plastic deformation and dynamic recovery. The second term gives the effect of static recovery and the third term expresses the effect of recrystallisation on the evolution of dislocation density during annealing. Recrystallisation results in new dislocation-free grains, thus reduces the average dislocation density. This equation is employed in this paper to model the dislocation density evolution of ferritic steel during cold forming and annealing.

3.4.2 Modelling of static recrystallisation

During annealing, two separate mechanisms tend to annihilate dislocations: static recovery as discussed above and static recrystallisation. The annealing time-temperature and total deformation dependence for ferrite recrystallisation have been established for cold and hot forming. It is well known that static recrystallisation is a function of the prior strain (Priestner and Ibraheem, 2000). When crystalline materials are deformed at room temperature, the dislocation density is increased, due to the

continued trapping of newly created mobile dislocations by existing ones and their incorporation into the various microstructural features. One of the most obvious features is that the grains change their shape and there is a surprisingly large increase in the total grain boundary area (Humphreys and Hatherly, 1996). The energy associated with this increase in area represents a significant part of the stored energy of cold working and it will be greater for small grain sizes and large strains (Sevillano et al., 1980). The stored energy, which provides the driving force for recrystallisation, increases with strain. Such static recrystallisation leads to the elimination of a large number of dislocations, and creates dislocation free grains. The critical value of dislocations for recrystallisation is expressed as (Sandström and Lagneborg, 1975):

$$\rho_c = \frac{4\sigma_{surf}}{\tau d^*} \qquad \textbf{3.7}$$

where σ_{surf} is the grain boundary energy per unit area, τ is the average energy per unit length of a dislocation and d^* the diameter of the recrystallisation nucleus. The deformation dislocation substructure provides the driving pressure for recrystallisation, F_R, which is expressed as (Martínez-de-Guerenu et al., 2004 (b)):

$$F_R = \frac{1}{2} G b^2 \rho \qquad \textbf{3.8}$$

It can be seen in Equation 3.8 that the increasing dislocation density drives the migration of the recrystallisation front into the deformed area. Both recovery and recrystallisation are controlled by different kinetics and consequently the extent of

overlapping depends on the annealing temperature and holding time. The relationship between the volume fraction of recrystallisation S and the holding time t is normally represented using empirical expressions, such as that given by the Avrami equation (Sakai and Jonas, 1984):

$$S = 1 - \exp\left\{-\left(\frac{p}{d_0}\right)t^q\right\} \qquad \textbf{3.9}$$

where p and q are constants and d_0 is the initial grain size. As recrystallisation is directly related to dislocation density during annealing, when the normalised dislocation density exceeds the critical value $\bar{\rho}_c$, recrystallisation will take place, given sufficient time. Below that, recrystallisation will not occur. The equation for describing the evolution of austenite recrystallisation during hot deformation is written as (Lin and Liu, 2005):

$$\dot{S} = H \cdot \left[x \cdot \bar{\rho} - \bar{\rho}_c \cdot (1 - S)\right] \cdot (1 - S)^{\lambda_1} \qquad \textbf{3.10}$$

where H and λ_1 are material constants. For the work described in this paper, the specific fundamental mechanisms for austenitic steel and ferritic steel are similar. Therefore, it is appropriate to apply the formulation based on austenitic steel to the ferritic steel. The variable x describes the onset of recrystallisation:

$$\dot{x} = X_1 \cdot (1 - x) \cdot \bar{\rho} \qquad \textbf{3.11}$$

where X_1 is a material constant. The recrystallised volume fraction S varies from 0 to 1 and its variation is cyclic, depending on the evolution of dislocation density. These equations can be applied also, to model static recrystallisation of low carbon ferritic steel with appropriate consideration of the specific features of ferrite and austenite.

3.4.3 Grain size evolution

A few investigations have led to the development of empirical relationships that enable the calculation of the ferrite grain size after recrystallisation under various conditions. The equation introduced by Majta and Zurek (2003) has been used to predict the ferrite grain size under inter-critical (austenite-ferrite two-phase region) forming conditions in low carbon steel, and is:

$$d = d_{rex}S + d_0(1-S) \qquad \textbf{3.12}$$

where d_{rex} is the recrystallised ferrite size. When deformation conditions are adequate, such as a temperature below transformation starting temperature, large deformation, and recrystallised ferrite can be observed in the hardened structure. In such a situation the recrystallised ferrite grain size can be calculated using the procedure proposed by Barnett et al. (1994):

$$d_{rex} = Cd_0^a \varepsilon^{-e} Z^{-c} \qquad \textbf{3.13}$$

where ε is the effective strain, Z is the Zener-Hollomon parameter, C, a, e and c are material constants. These equations enable the modelling of ferrite grain size evolution after transformation from austenite during hot deformation.

During annealing, grain refinement and static grain growth work independently. Due to recrystallisation, new grains are nucleated and the total number of grains increases. Consequently, the average grain diameter d decreases. At the same time static grain growth takes place, which results in an increase in the average grain size. Taking only recrystallisation into account, the evolution of the average grain diameter $\dot{d}$ can be written as (Sandström and Lagneborg, 1975):

$$\dot{d} = -d\left(\frac{df_1}{dt}\right)\ln N \qquad \textbf{3.14}$$

where N is the number of new grains after one cycle of recrystallisation, which may be grain size dependent and f_1 the number of recrystallisation cycles, which can be non-integer number. When recrystallisation, which is driven by the stored energy of cold work, is complete, the structure is still not yet stable, and further growth of the recrystallised grains may occur. An equation to describe the post-recrystallisation grain growth is given by (Lin and Liu, 2005):

$$\dot{d} = m\sigma_{surf}d^{-\gamma_0} \qquad \textbf{3.15}$$

where m is the grain boundary mobility and γ_0 a material constant. The equation represents the static grain growth, which is directly related to grain boundary mobility and grain boundary energy density σ_{surf}. Combining Equation 3.14 with 3.15 in consideration of static grain growth and grain refinement due to recrystallisation, as well as taking into account of the equations developed by Lin and Liu (2005), the average ferrite grain size evolution can be expressed as:

$$\dot{d} = G_1 \cdot \left(\frac{d_0}{d}\right)^{\psi_1} - G_2 \cdot \dot{S} \cdot \left(\frac{d}{d_0}\right)^{\psi_2} \qquad \textbf{3.16}$$

where G_1, ψ_1, G_2 and ψ_2 are material constants. The first term of the equation represents the static grain growth following recrystallisation and the second term describes recrystallisation induced ferrite grain refinement. Comparing these two terms, it can be seen that refinement due to recrystallisation plays a more important role during the initial stage of the annealing process, and static grain growth becomes the dominant mechanism after recrystallisation.

3.5 Summary

During cold deformation and annealing operations, most metals experience dynamic changes and static changes and their flow behaviour is influenced by these changes. Complex microstructural evolution during heat treatment has been discussed. Strain hardening due to accumulation of dislocations and softening due to recovery and recrystallisation, dominate material behaviour during cold working and heat treatment,

respectively. The relationships between the internal state variables; dislocation density, grain size and recrystallisation and processing parameters strain, strain rate are detailed and summarised by schematic representations. This provides a foundation for developing a set of unified mechanism based viscoplastic constitutive equations to model cold deformation and subsequent annealing.

CHAPTER 4

Experimental investigation of microstructural evolution (Single Phase)

4.1 Introduction

In this chapter experiments undertaken to determine the relation between tensile strain and damage in a single phase linepipe steel, are described. Firstly, the steel studied is described and metallurgical properties presented. In order to model damage tolerance during cold deformation and subsequent heat treatment, it is necessary to know the microstructure and damage evolutions and their interaction. A uniaxial tensile test programme is designed to reveal the damage occasioned by deformation and repair arising from heat treatment

4.2 Objectives of the experimental programme

During the review in Chapters 2 and 3, it was stated that plasticity-induced damage is the dominant mechanism leading the material failure during cold deformation. And certain heat treatment conditions could reduce the damage level and restore the mechanical properties depending on the microstructure. In order to model the effects of microstructural evolution on mechanical property and damage restoration, the mechanisms and phenomena of change, at different stages during cold forming and subsequent annealing need to be understood. The effects of time at temperature on damage also remain uncertain. As stress state dependence plays a very important role in plasticity-induced damage, it is necessary to further study this effect on damage through an experimental investigation. To investigate the effects of these process factors, a group of interrupted uniaxial tensile tests have been designed and details of

the test conditions are given in the Section 4.6. Microstructural analyses were also carried out before and after deformations to identify damage nucleation, growth and coalescence mechanisms and to represent the microstructure evolution.

4.3 Material as received

The raw material used in the experiments was a plate steel, code named STC-C, used for large diameter pipes and supplied by Corus R, D & T Swinden Technology Centre. It was produced through continuous casting and hot rolling. Its chemical composition is shown in Table 4.1. It is a low carbon ferritic pipe steel, with very fine grains, of size averaging about 10 μm after pre-heat treatment and all the steels were fully annealed to remove strain hardening prior to testing. Hence, both strength and ductility of the received steel were higher than rolled low carbon steels.

Plate code	Cast	C	Si	Mn	P	S	Al	Cr
STC-C	929521	0.034	0.34	1.56	0.005	0.0012	0.037	0.17
Plate code	Mo	Ni	Cu	Nb	Ti	V	N	Pcm
STC-C	0.007	0.012	0.015	0.044	0.013	0.004	0.0042	0.135

Table 4.1. Chemical compositions of STC-C steels.

Fig. 4.1 shows the microstructure of the steel, lightly etched with picric acid to reveal grain boundaries and the ferrite grain structure. The shapes of ferrite grain along rolling direction are longer and more unidirectional compared to those in the transverse direction, as shown in Fig. 4.1. Only a few manganese sulphide inclusions were observed in the steel, due to its low sulphur content. The inclusions appear as dark grey globular forms about 1-3 μm in diameter. They are randomly orientated and often

deviate from spherical. The distribution and shape of inclusions were treated as uniform and symmetric. They were distributed randomly within the matrix material, at ferrite grain boundaries and within grains equally. No existing defects or porous features have been identified in the as-received steel.

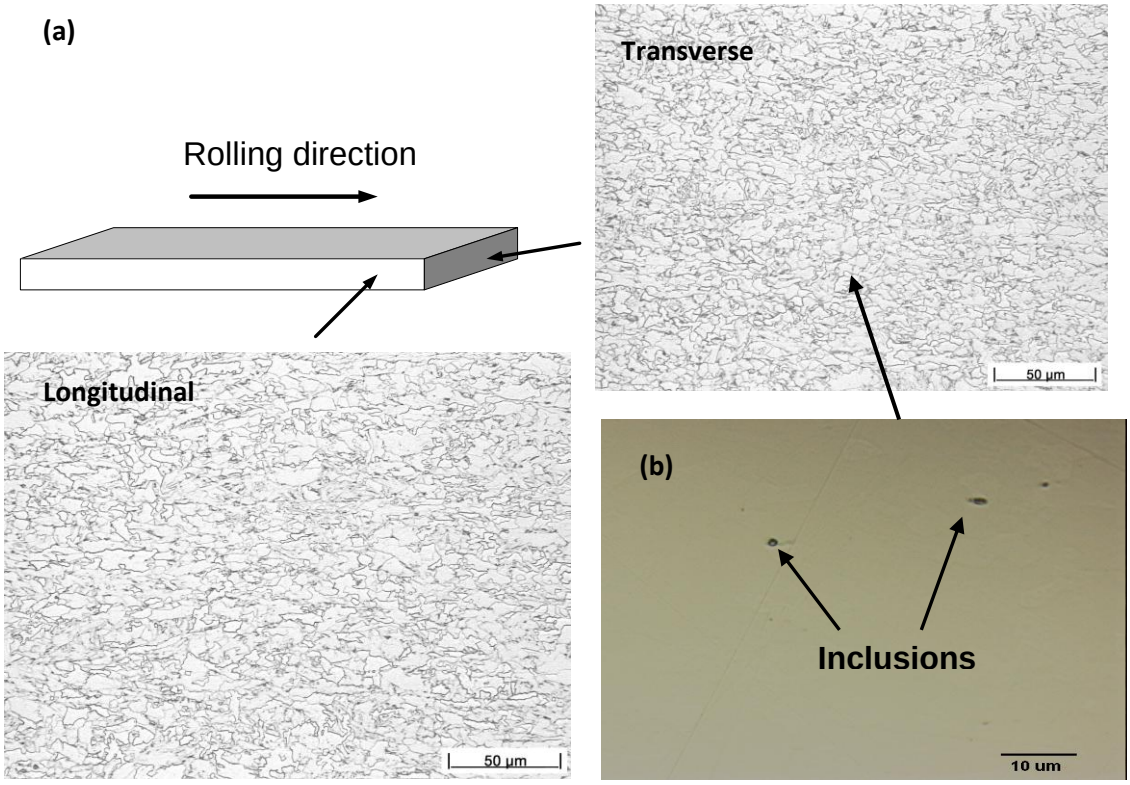

Fig. 4.1. Microstructures of STC-C steel. (a) Etched steel showing grain structure, (b) Unetched steel in transverse direction.

4.4 Experimental equipment

4.4.1 Tensile testing

Zwick 100 universal testing machine, shown in Fig. 4.2, was used for all interrupted uniaxial tensile tests. It can be programmed to simulate the mechanical process variables for a wide range of deformation conditions, by controlling variables, such as stroke, force and strain. Data were collected from measurement transducers distributed

within the machine. A transverse (diameter) extensometer (C-strain gauge transducer), as shown in Fig. 4.3, was used to measure the diameter variation during tensile tests and the experimental data was instantly acquired from this instrument. The knife-edges were positioned at a pre-determined position on the test-piece.

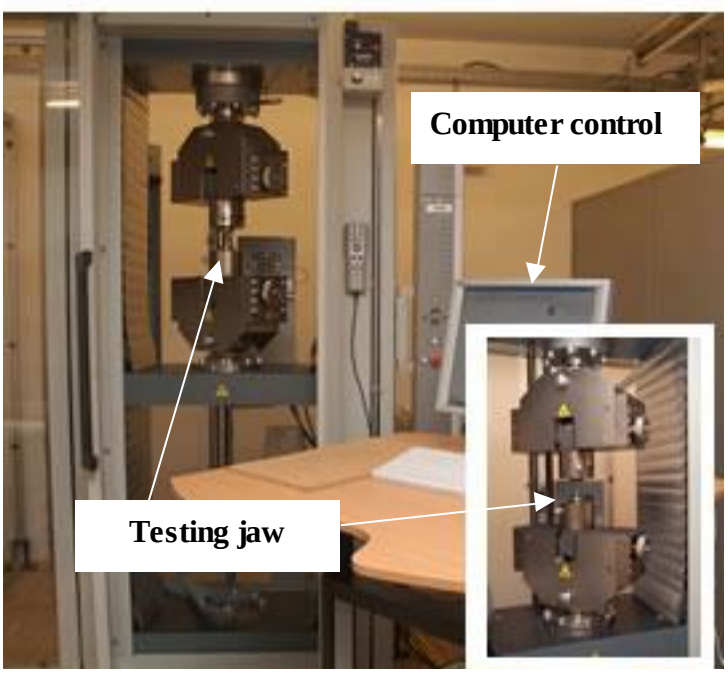

Fig. 4.2. Zwick Z100 universal testing machine.

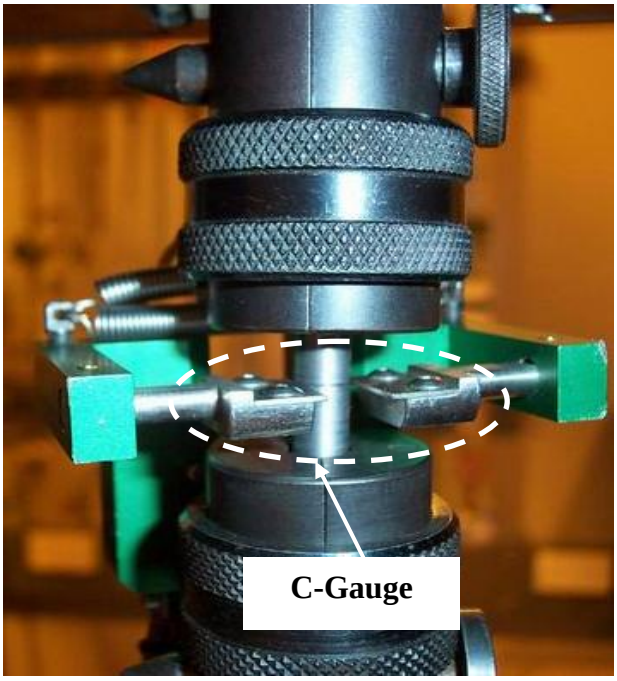

Fig. 4.3. C-strain transverse (diameter) extensometer.

4.4.2 Specimen preparation and metallographic equipment

For microstructural analysis, experimental test pieces were mounted in Bakelite, then ground and polished by hand to remove any deep marks. Final polishing was completed in stages using three sizes of polishing compound; 15, 6 and 3µm. Aluminum oxide finishing polish with 1µm diamond pastes was then used to remove remaining scratches. After polishing, specimens were cleaned using acetone and then etched with saturated picric acid. A scanning electron micrograph (SEM) microscope, JEOL 6060, was used to examine the damage and microstructure of the specimens with up to 10000 times magnification. To determine the composition of material, Energy Dispersive X-ray (EDX) analysis was carried out using a JEOL 6060 SEM equipped with an Oxford Inca EDX analyser. Investigation of microstructures was carried out at all different stages: original material, after first step tensile test, after heat treatment and failure.

Test-pieces were sectioned longitudinally (see Fig. 4.4) to expose the cross-section area of the damaged face.

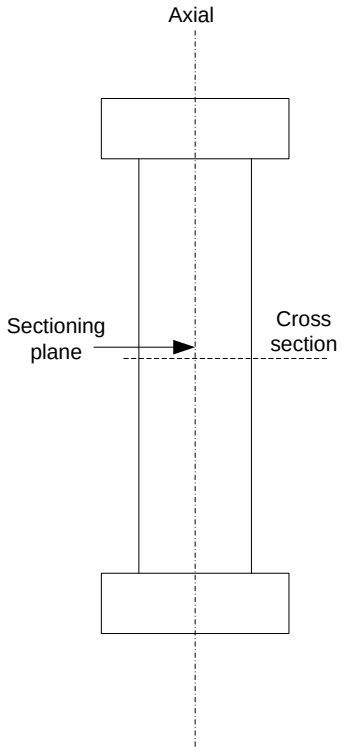

Fig. 4.4. Specimen sectioning plane.

4.5 Experimental set-up

The standard tensile test-pieces were made subject to the recommendations of specimen data by the Lloyd Instruments manual (1986) and the size of grips employed in the tests, as illustrated in Fig. 4.5. The tensile bars were cut from the plate in the transverse direction. However, the jaws of Zwick machine were flat and could grip only sheet test-pieces. Therefore, a pair of adaptors was designed to connect the flat jaws and round grips, which are shown in Fig. 4.6.

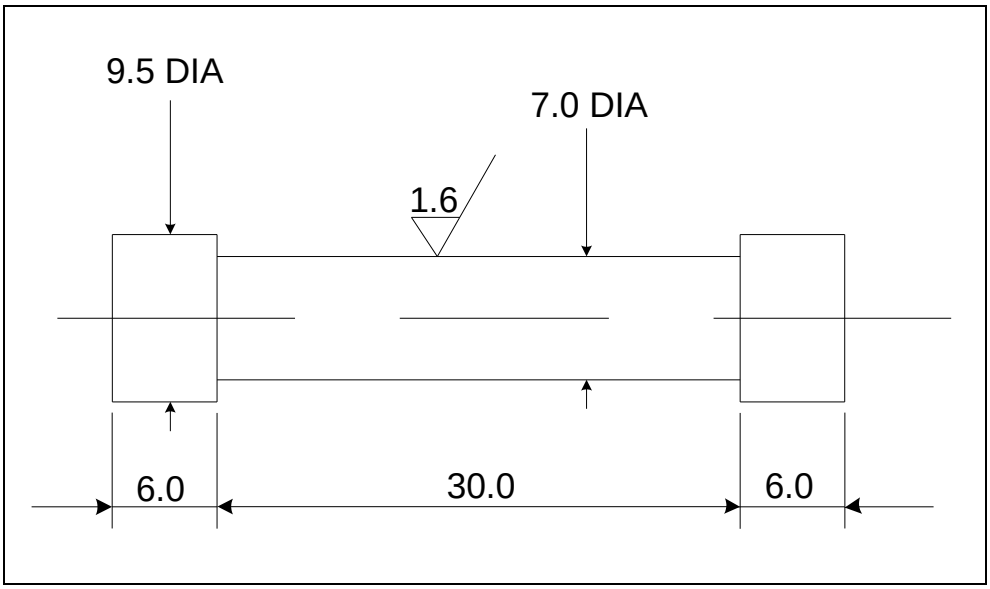

Fig. 4.5. Standard round test-piece for interrupted tensile tests.

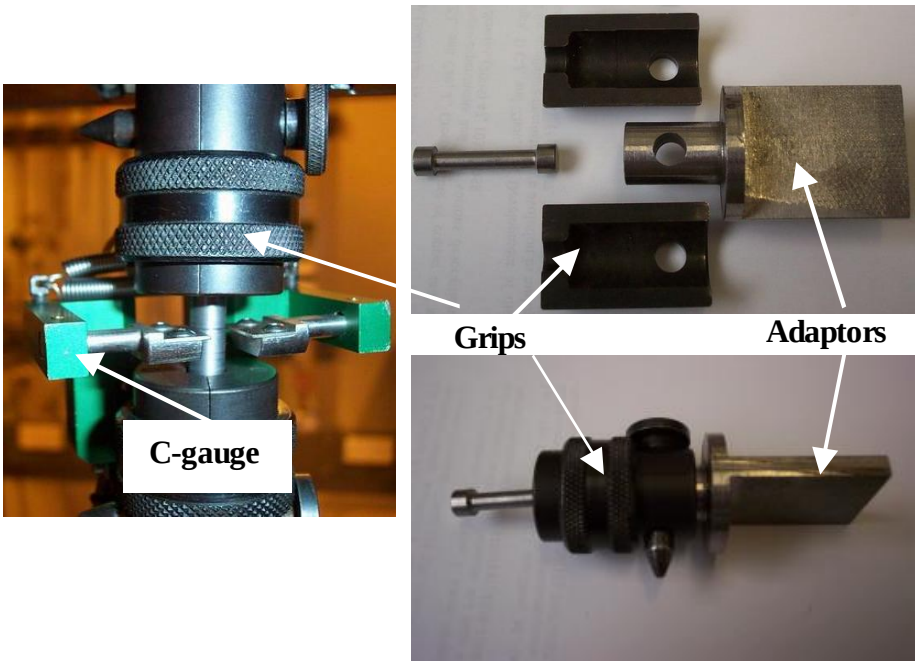

Fig. 4.6. Tensile test set-up.

Pair of grips and adaptors was used at each end of the test-piece. Displacement feedback was by means of an L-gauge mounted between the jaws. To ensure high

accuracy of strain measurement, the location of the C-gauge was periodically adjusted to ensure diametrical strain readings were taken at the visible neck location at all times. The true strain-stress can be calculated for the tensile specimens by:

$$\sigma_T = Force/\left[\pi\left(d_{dia} + \Delta d_{dia}\right)^2/4\right] \quad \textbf{4.1}$$

$$\varepsilon_T = 2 \cdot \ln\left[d_{dia}/\left(d_{dia} + \Delta d_{dia}\right)\right] \quad \textbf{4.2}$$

where Δd_{dia} is the variation of the test-piece diameter during deformation and d_{dia} is the original diameter of the test-piece. The equations were used to work out instantaneous true stress-strain relationships during tensile tests. Experimental data of stress, strain, force, elongation of test-piece and variation of test-piece diameter was acquired using a data logger.

4.6 Test procedure

The overall interrupted processing route is given schematically in Fig. 4.7. There are three main stages involved in the whole interrupted tensile processing route. Stage 1: The 1st step tensile tests were carried out at room temperature (20ºC), at a strain rate of $0.008s^{-1}$. On reaching a pre-specified strain, the test was stopped. Stage 2: The test-pieces were then moved to a furnace preheated to 700ºC for heat treatment. Considering the temperature need to uniformly distribute within whole test-piece prior to count annealing time, additional 2 minutes was given to preheat the test-pieces to 700ºC. Heating time was controlled within the range of 8-60 minutes at the constant temperature and subsequently cooled in air. Stage 3: The test-pieces were strained in tension (2nd step) to failure, at room temperature.

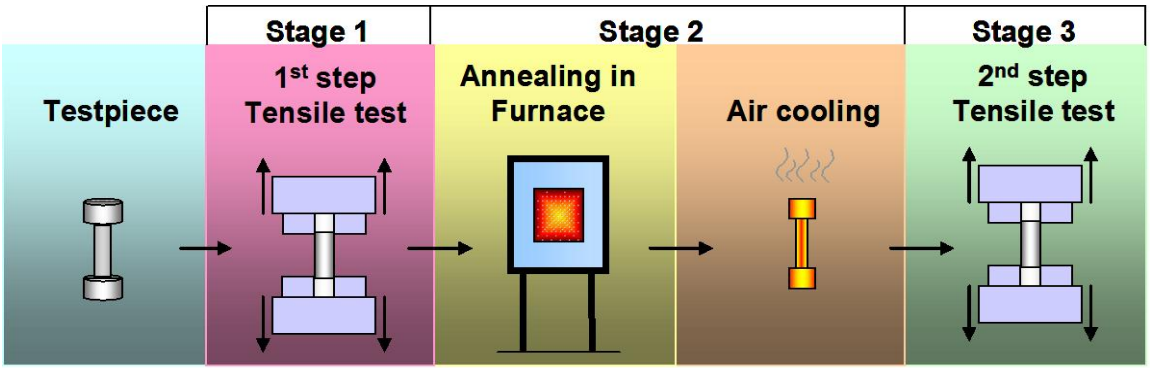

Fig. 4.7. The processing route for interrupted uniaxial tensile tests.

Experiments were divided into three categories:

Set 1: Interrupted tensile tests with various annealing times

A time-temperature plot of deformation and annealing process is given in Fig. 4.8. Test-piece in Stage 1 is deformed to $\varepsilon = 0.2$, annealing time varies from 8 to 60 minutes in stage 2. Also a conventional, continuous tensile test, performed at room temperature without interrupt is carried out. Total 12 tests were carried out in Set 1.

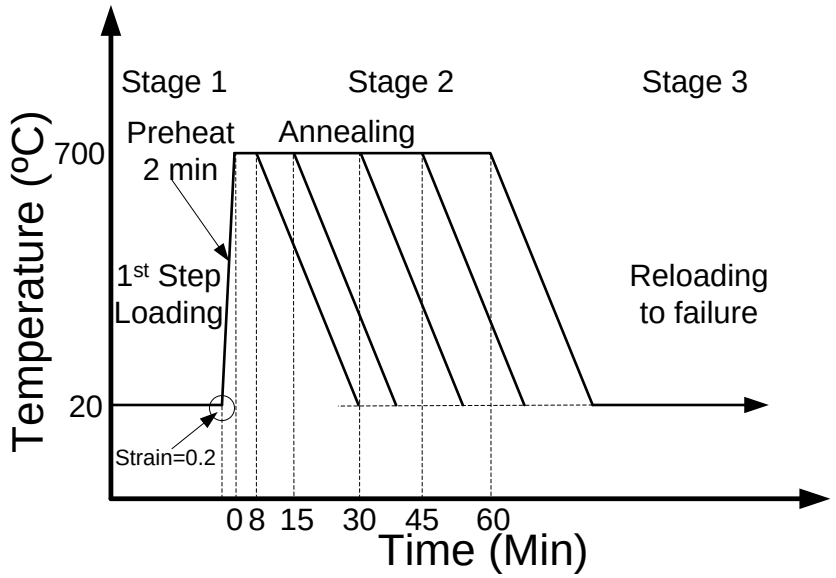

Fig. 4.8. A schematic representation of interrupted tensile tests Set 1.

Set 2: Interrupted tensile tests with various pre-strain

Set 2a: A time-temperature plot of deformation and annealing process is given in Fig. 4.9. First step strain between 0.2~1.3 was applied during Stage 1, with fixed 60 minutes annealing in stage 2.

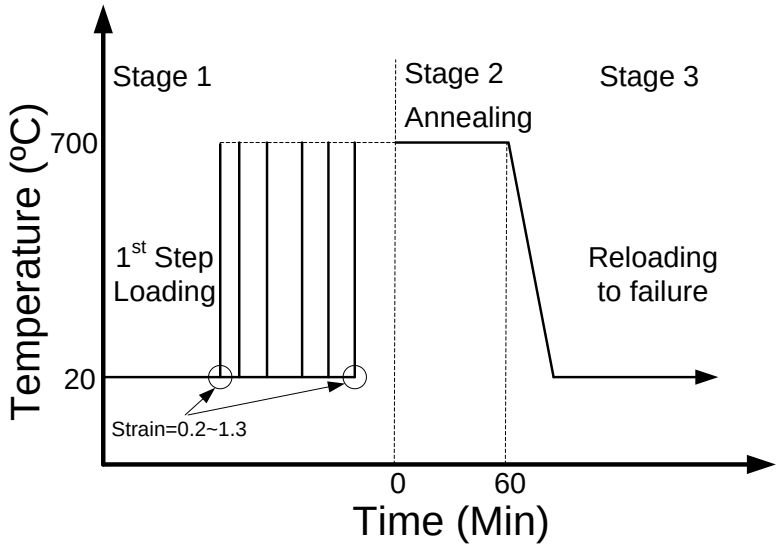

Fig. 4.9. A schematic representation of interrupted tensile tests Set 2.

Set 2b: The same first and second step deformations, as Set 2a were applied, but annealing was omitted. Total 24 tests were carried out in Sets 2a and 2b.

Set 3: Interrupted tensile tests with first stage neck removed

On reaching a pre-specified strain after first step tensile test, necking may take place at cross section area of test-pieces, as shown in Fig. 4.10a. The necking is greater for higher strains. To consider the stress state effect on damage evolution, the gauge lengths of the test-pieces were re-machined to uniaxial cylinders to remove the necking. The overall neck removing process is shown schematically in Fig. 4.10b. The diameter

of remade round tensile test-pieces had a diameter equal to that of the neck after first stage deformation.

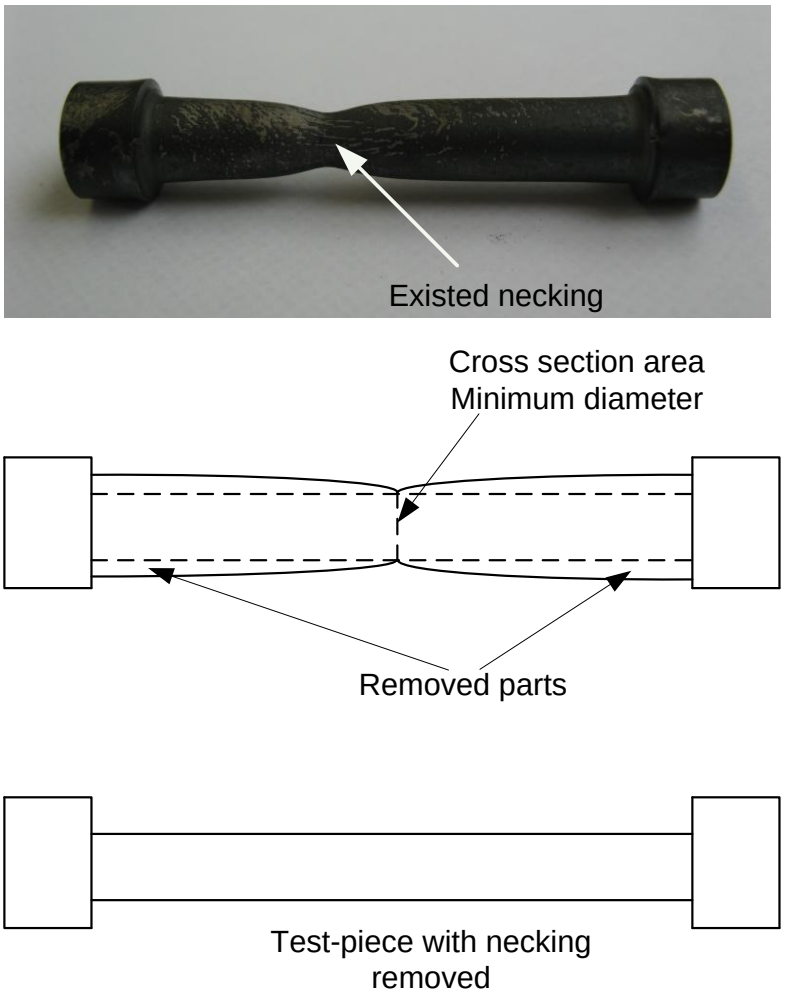

Fig. 4.10. (a) Test-piece with existed necking after first step cold tensile test. (b) a diagram showing the necking removing process.

The corresponding temperature-time profile of interrupted tensile test with neck removed is illustrated in Fig. 4.11. The first stage strain ranged between 0.2~1.3. Total 26 tests were carried out in Set 3.

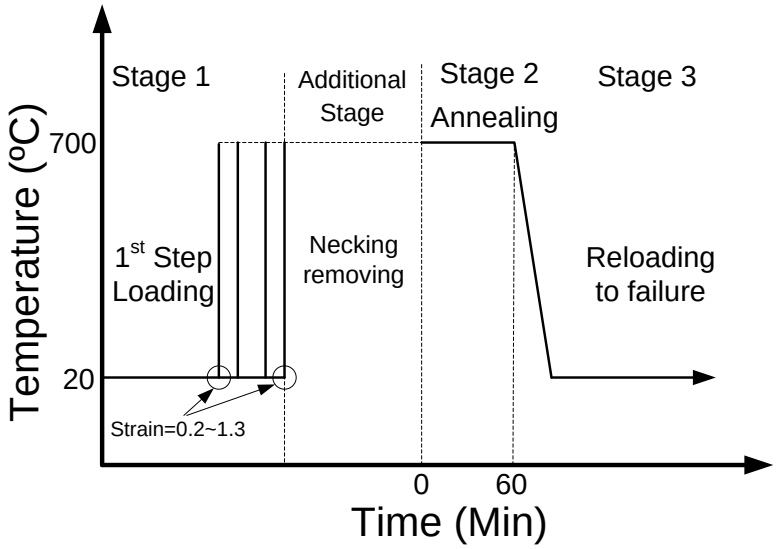

Fig. 4.11. A schematic representation of interrupted tensile tests Set 3.

4.7 Summary

The overall strategy of experimental investigation on microstructure and damage evolution under cold working condition and subsequent heat treatment is proposed. The experimental procedures of all sets of interrupted uniaxial tensile tests were planned to study the effects of microstructure on mechanical properties with variety heat treatment conditions. The test processes are schematically represented. The equipment used in experimental investigation is briefly introduced. Testing results are given in the following chapter 5.

CHAPTER 5

Practical investigation of mechanical properties and microstructural evolution

5.1 Introduction

In this chapter, experimental results are reported and experimental knowledge of stress-strain relationships, damage evolution, microstructural evolution and their relationships for a variety of interrupted conditions are studied. Mechanical response and damage evolution coupled with plastic deformation and microstructural evolution during heat treatment, are rationalised. Microstructural evolution and damage mechanisms are then summarised for use in the development of viscoplastic-damage equations, which are able to predict microstructure evolution, damage and their interaction during cold deformation with subsequent heat treatment.

5.2 Effect of annealing times on mechanical properties

5.2.1 Mechanical response

Flow stress-strain relationships obtained from Set 1 tests are given in Fig. 5.1. Material ductility was very high for all tests, with failure strains between about 1.7 and 2.1. This is expected for a low carbon ferritic linepipe steel, with very fine grains, of size averaging about 10.5 μm after pre-heat treatment. All sets of stress-strain relationships have the similar feature that peak stress was followed by abrupt onset of failure.

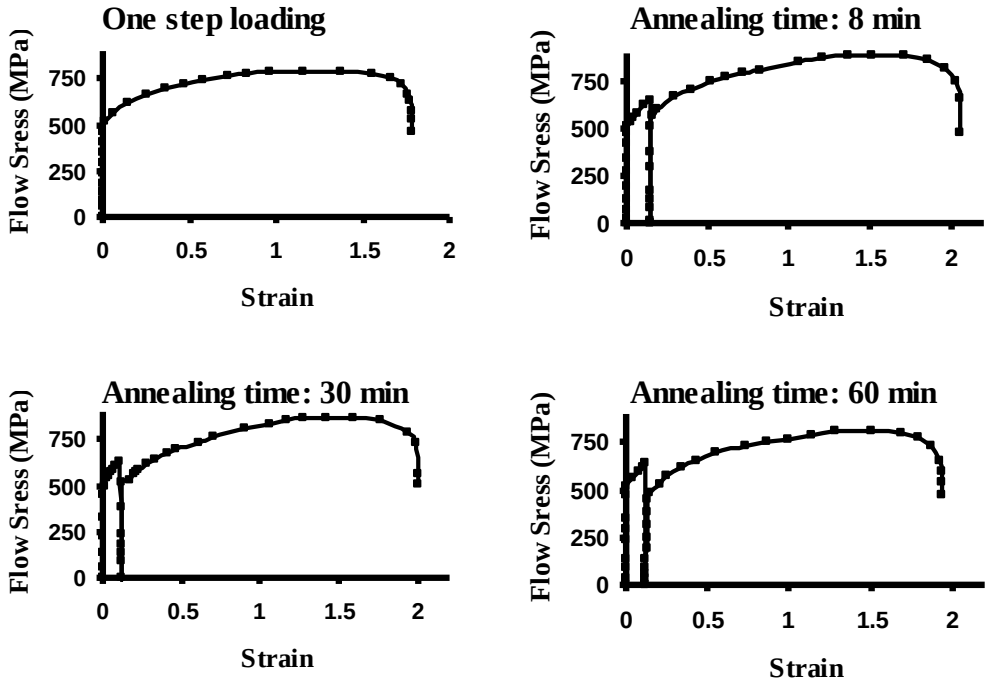

Fig. 5.1. Stress-strain relationships for one step loading and interrupted tensile tests with annealing for 8, 30 and 60 minutes at 700ºC.

In order to grade ductility and peak flow stress of the inter-stage annealed test-pieces a comparison was made with the continuously tested to failure test-piece in Fig. 5.2. It can be seen that the value of peak stress and strain to failure, against annealing time, decrease linearly with annealing time. The highest ductility and maximum peak stress are obtained for 8 min annealing time. In addition, all test-pieces subjected to annealing have higher ductility than the un-annealed one-step test-piece. This is believed to be due to the favourable microstructure (finer grain than raw material) formed through recrystallisation and recovery, by annealing, resulting in enhanced mechanical properties.

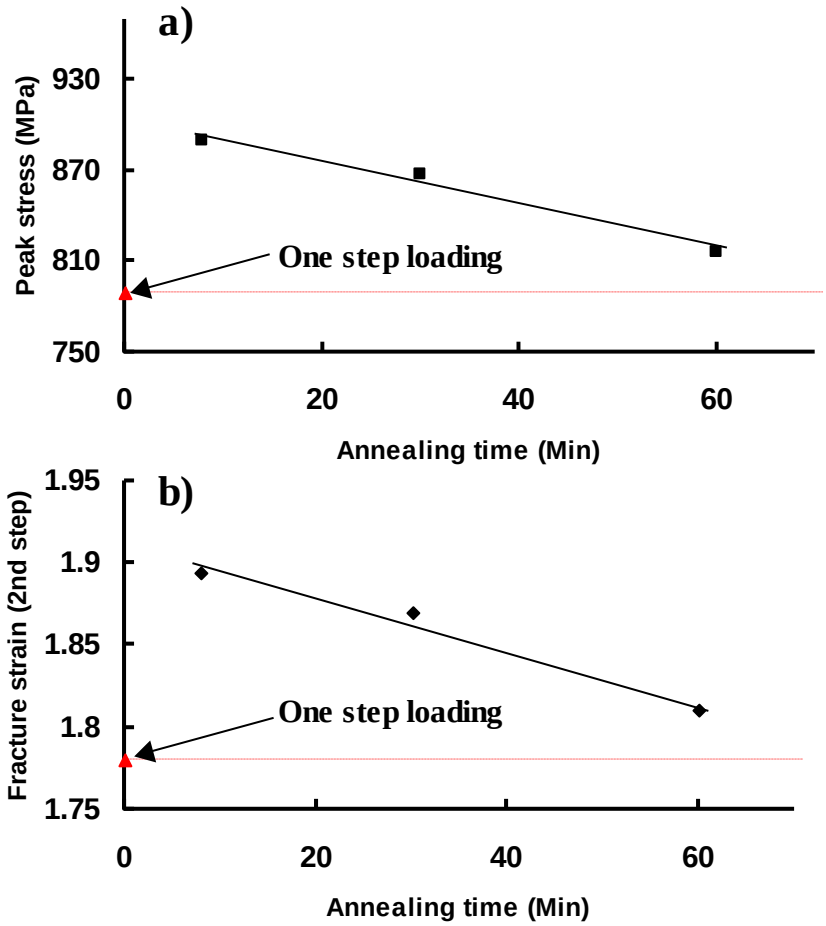

Fig. 5.2. Peak stress and fracture strains of second step loading against annealing time for 8, 30 and 60 minutes at 700°C.

5.2.2 SEM analysis of microstructure evolution

The relation between mechanical properties and microstructure after annealing was examined using SEM. The micro-voids were not significantly developed after first step strain at 0.2 under practical microstructure observation. Therefore, strain was extended to 0.4 after first step deformation in terms to observe the micro-voids evolution during annealing. Stages at which observations were made are shown in Fig. 5.3. Stages 1 and 2 were, the original and deformed metal (0.4 true strain). Stages 3, 4, 5 and 6 were post annealing after 0.4 strain, for different lengths of time.

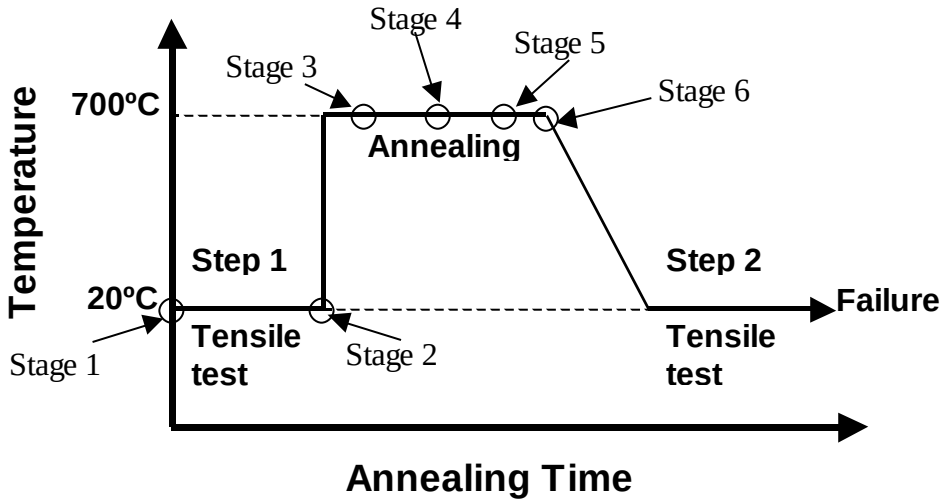

Fig. 5.3 SEM observed positions for microstructure analysis.

Fig. 5.4(a) shows the original microstructure of the steel prior to deformation, where regular grains can be observed. The microstructure of the cold deformed steel is shown in Fig. 5.4(b), where grains are elongated in the deformation direction. Micro-voids, about ~2 μm long, can also be observed. These have nucleated and grown by plastic deformation of the surrounding material.

Fig. 5.4(c) shows that, after 8 min annealing at 700°C, static recovery becomes the dominant mechanism for dislocation annihilation and rearrangement. A number of new fine grains, indicating recrystallisation nucleation, can be observed in the microstructure. Nucleation of recrystallisation takes place at grain boundaries, where dislocation density is high. As shown in Fig. 5.4(d), recrystallisation is about complete after 15 min annealing and the average grain size is smaller than that of the original material, shown in Fig. 5.4(a). The decrease of the grain size, due to recrystallisation, leads to a higher ductility of the steel.

For greater annealing times, grains start to grow and average grain size increases. A more homogeneous and refined ferrite microstructure is produced, as can be seen in Figs. 5.4(e) and (f), for 30 and 60 min annealing periods, respectively. The microstructure of the steel formed after 60 min annealing is more uniform, as shown in Fig. 5.4(f). Similar microstructures are observed in the original material (Fig. 5.4(a)) and in the cold deformed material after 60 min annealing (Fig. 5.4(f)). This shows that microstructural characteristics and therefore mechanical properties, if no large voids have nucleated, can be recovered by annealing. This can explain the strain-stress relationships obtained from the interrupted tensile tests above. These results indicate that the mechanical properties of the steel are strongly related to microstructural state.

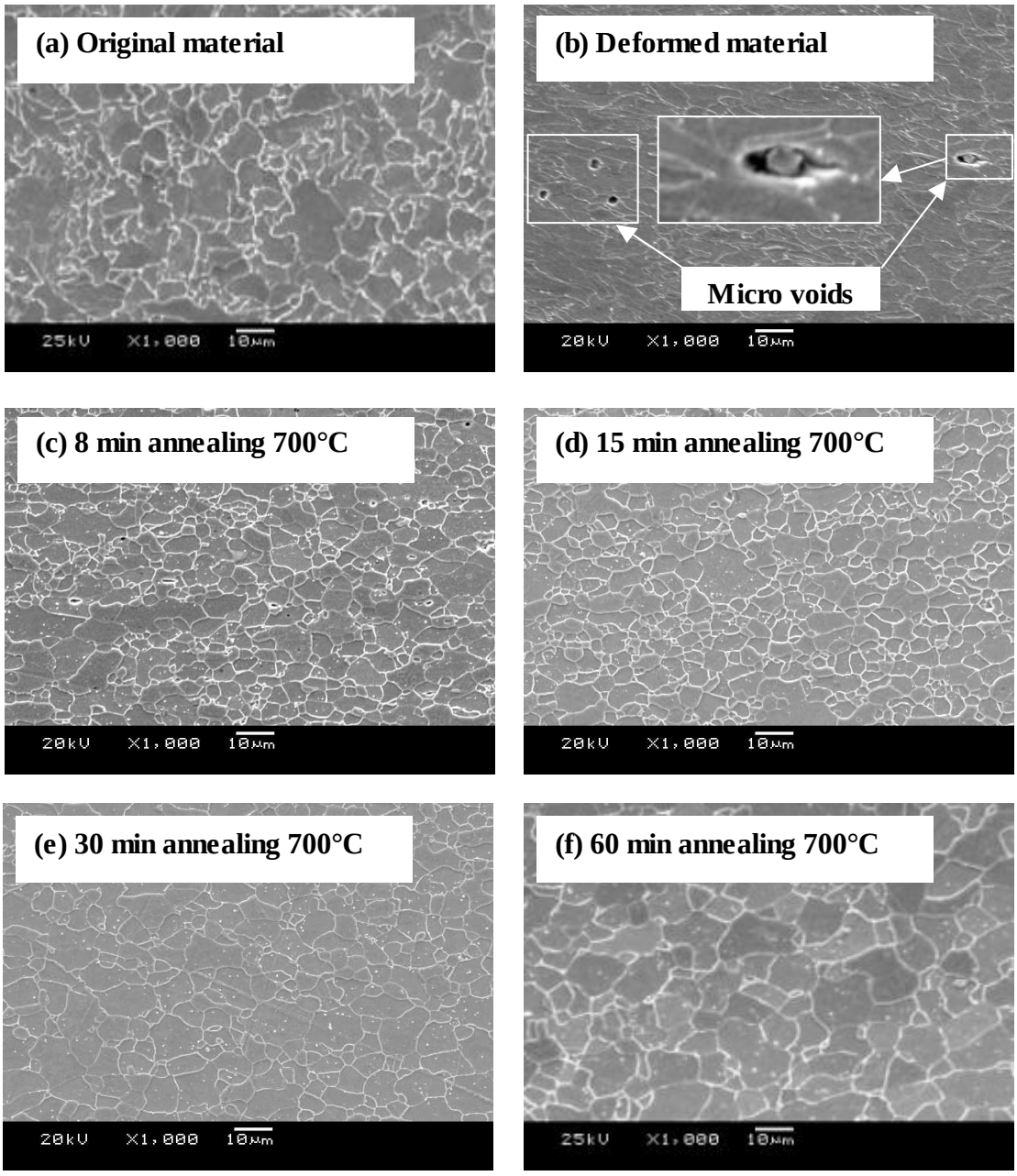

Fig. 5.4. Microstructure evolution for different annealing periods for the low carbon linepipe steel. (a) Original, (b) deformed at true strain of 0.4, with annealing for (c) 8, (d) 15, (e) 30 and (f) 60 minutes.

Fig. 5.5 shows the average grain size after annealing with first step strain at 0.4, determined using visual inspection method (Dougherty and Lotufo, 2003). The complex relationship between annealing time and grain size, shown by the curve is

interpreted as the result of static recrystallisation. Due to the previous plastic deformation, dislocation density continuously increases which leads to static recrystallisation when a test-piece is heated to annealing temperature. Grain refinement begins due to recrystallisation and reaches a lowest value 6.9 μm of average grain size at around 8 minutes annealing time. As static recrystallisation finishes, grain growth takes over and leads to the grain size steadily increasing to 10 μm after 60 minutes annealing at 700°C, as shown in Fig. 5.5. The grain size after 60 minutes annealing is still below the average initial grain size. Grain size is the main factor controlling strength and ductility of ferritic steel and smaller grain size leads to higher strength and ductility during cold deformation. These facts probably are the reason that the highest peak stress and failure strain in second step deformation test-pieces exists in that annealed for 8 and are lower for higher and lower annealing times, as shown in Fig. 5.2. Also, they explain the higher ductility and strength of annealed test-pieces compared with those of the un-annealed one-step test-piece.

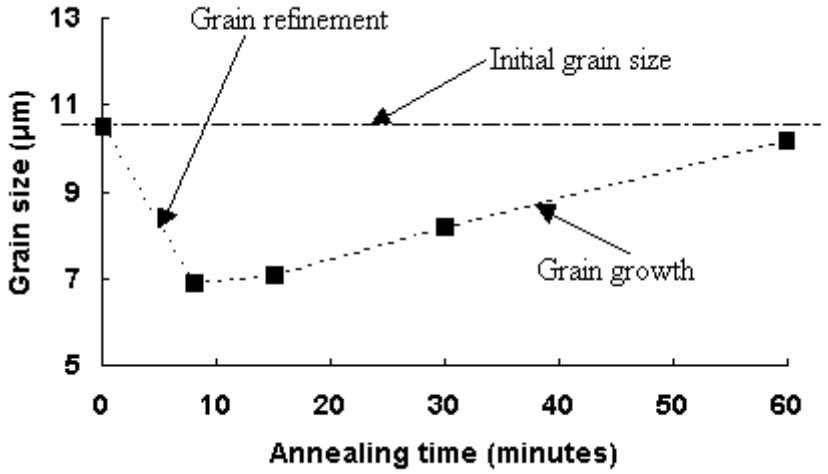

Fig. 5.5. The relation of grain size with annealing time at 700°C.

5.3 Effect of annealing on damage

5.3.1 Damage features due to cold deformation

Based on the pioneering work described in Chapter 2, at room temperature, damage phenomena are considered as being plasticity-induced. The damage develops with increasing deformation and finally might lead to failure. As shown in Fig. 5.6(a), the microstructure has a high level of damage associated with inclusions. The highly magnified area, Fig. 5.6(b), clearly indicates the damage features and related inclusions. To determine the composition of voids and inclusions, Energy Dispersive X-ray (EDX) analysis results are showing in Fig. 5.6(b). Point 1, 2 and 3, in Fig. 5.6(b), which comprise inclusion, void and matrix material respectively, were chosen for chemical composition analysis. As shown in Fig. 5.6, this shows that the light grey inclusion, Point 1, was manganese sulphide (MnS). Aluminium and oxygen peaks appearing at Point 2 are due to contamination from OP-A polishing fluid, drawn into the void and are not part of the steel's chemical composition. These inclusions related damage features are similar to those observed by Baker and Charles (1972), where inclusions had damage tails lengthened in the direction of the major strain.

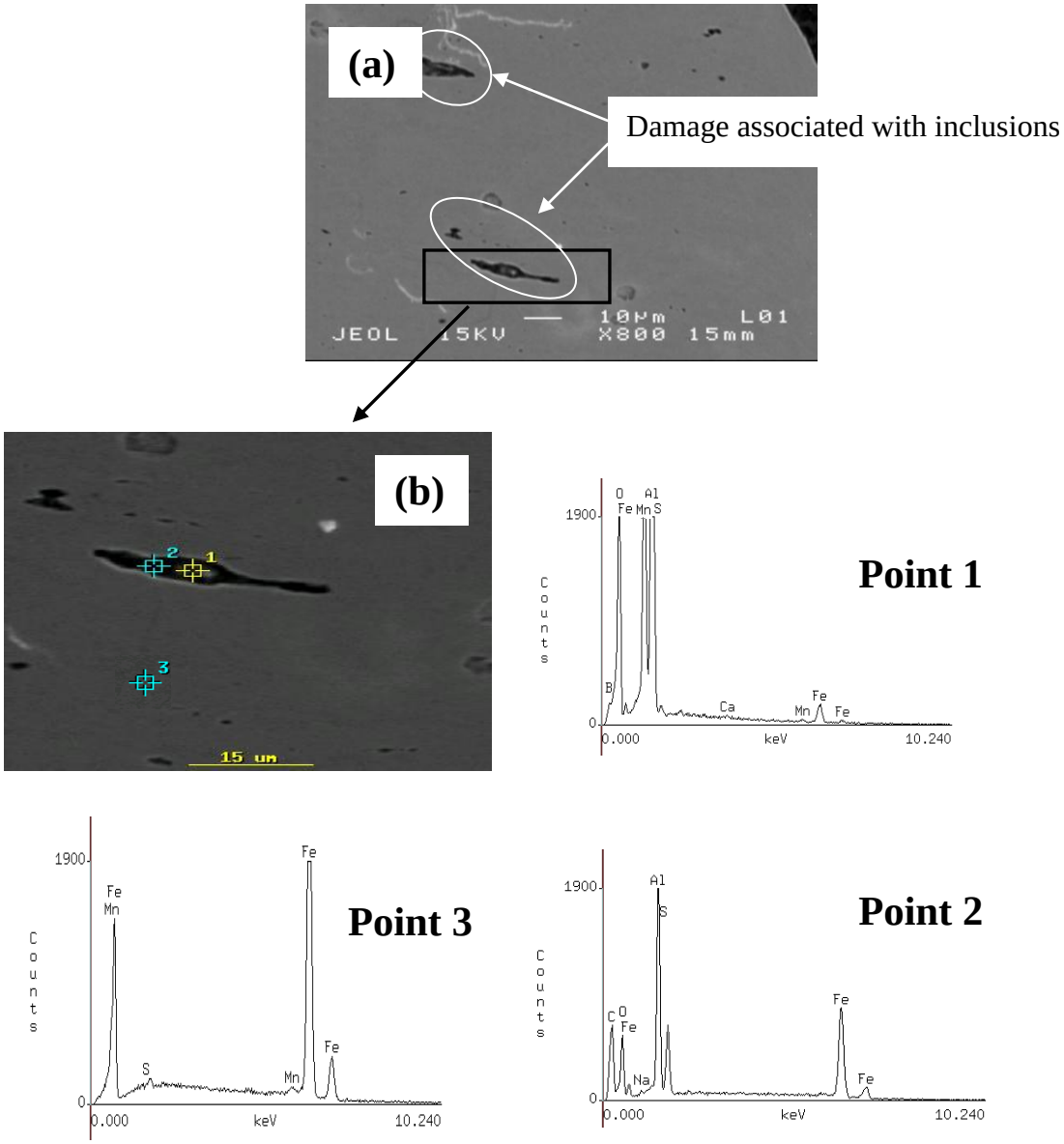

Fig. 5.6. Inclusion related damage at a failure surface and chemical composition analysis.

The interaction of inclusions is apparent. Fig. 5.7 shows the microstructure approximately 1mm below the failure surface, where the general damage level is lower than that on the failure surface. Two inclusions located in close proximity have an increased damage level, as if the level of strain has been heightened in this region. As shown in Fig. 5.7, failure might occur by coalescence of neighbouring voids formed at inclusions, potentially leading to macro cracking. With reference to modelling, these

features show that damage area alone cannot be used to predict a meaningful estimate of remaining ductility. Instead a method of predicting the onset of damage coalescence may be more appropriate.

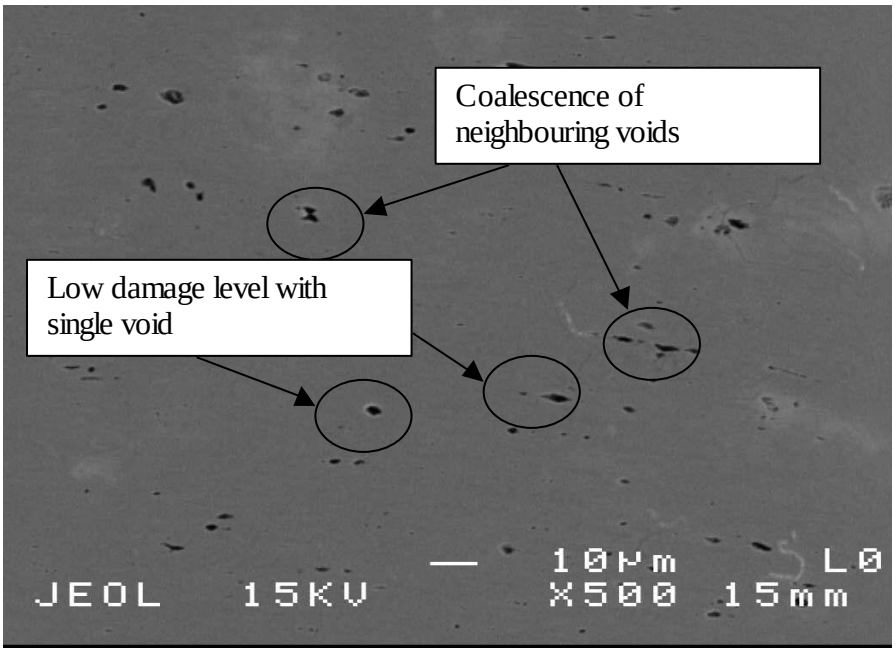

Fig. 5.7. Damage features, approx. 1mm below the fracture surface.

5.3.2 Mechanical response

Microstructural observations provide experimental evidence of the plasticity-induced damage and its evolution. Micro-voids can nucleate at inclusion/matrix interfaces at any stage of cold deformation, in which strain may be about 0.2~1.7. Subsequent annealing, recovery and recrystallisation can annihilate dislocations, relieve local stress concentrations and strain incompatibilities, temporarily impeding further growth of voids. The set of interrupted tests was designed for a study of this phenomenon based on the macroscopic response of flow stress and ductility.

Tensile stress-strain curves to failure, for Set 2a test-pieces, are shown in Fig. 5.8. Stress-strain curves in 'Step 1' are coincident, at the same strain levels. However, it is obvious that gross ductility of each test-piece in Step 2 is different. Gross ductility decreased with higher first step strain. The largest difference in ductility is between the test-piece with a 'Step 1' strain of 1.05 and the other test-pieces. The former is less ductile because it sustained more damage in 'Step 1', which was not significantly repaired by annealing.

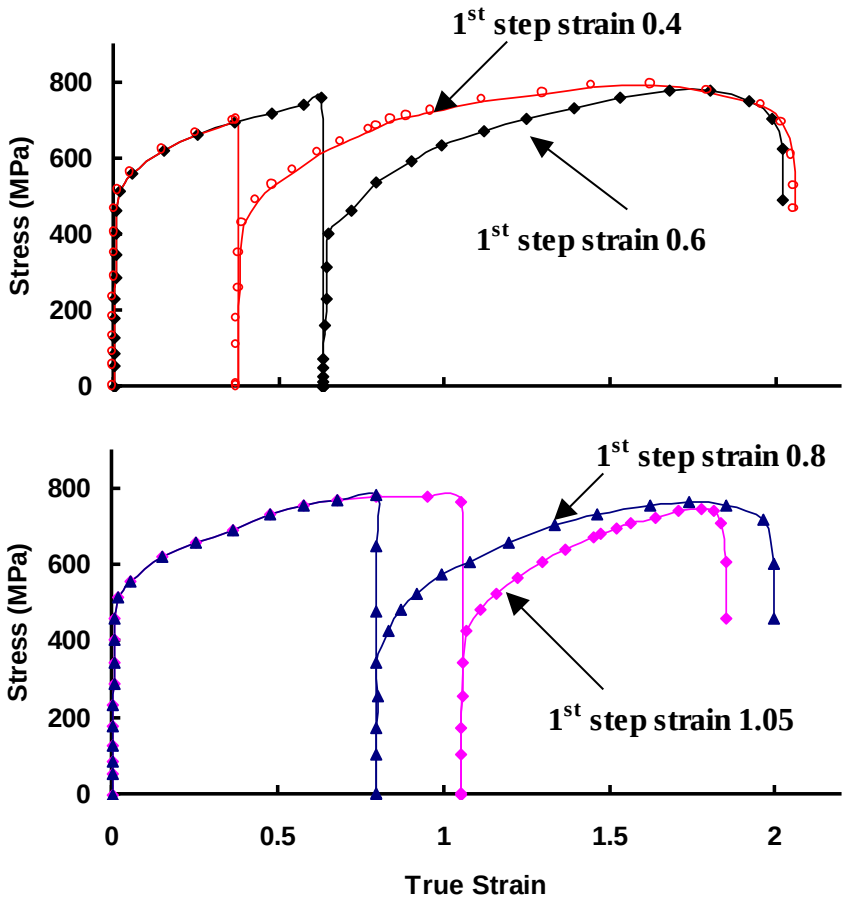

Fig. 5.8. The effect of first step strain on stress-strain relationships for first step strain of 0.4, 0.6, 0.8 and 1.05, with annealing 60 minutes at 700ºC.

To investigate the effect of annealing on damage and mechanical properties, ductility and peak flow stress for tests Set 2a are compared to the values obtained in tests Set 2b, are shown in Fig. 5.9 and Fig. 5.10.

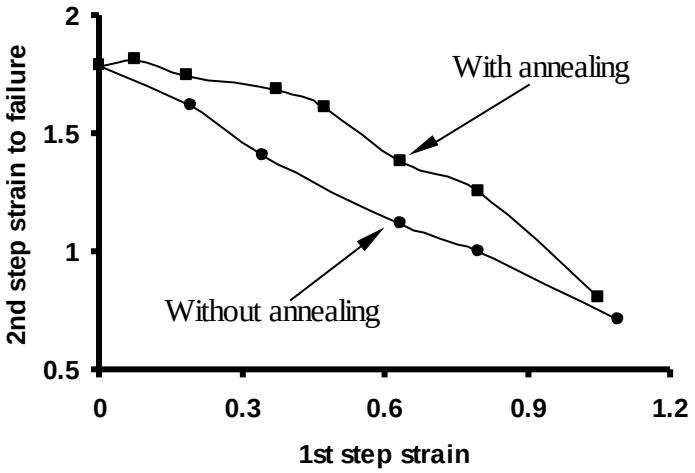

Fig. 5.9. Effects of first step deformations on second step ductility with and without annealing.

As can be seen in Fig. 5.9, annealing before the second step deformation improves second step strain to failure, except for the cases of zero and highest imposed first step strain values. It appears that the damage incurred in the first step is partially reduced by recovery and recrystallisation during annealing. The value of the second step strain to failure of the unannealed steel reduces approximately linearly with increasing value of first step strain. Compared with the value of second step strain to failure of the unannealed steel, the value of second step strain to failure of the annealed steel, for values of first step strain between zero and about one, are higher. This indicates that damage incurred by first step deformation was repaired, either fully or in part, by annealing, except at the highest imposed level of first step strain. A maximum difference between second step ductility of annealed and unannealed steel occurs for a value of first step strain of about 0.6. Therefore, the material demonstrates an

improvement in ductility with annealing. As the first step deformation continuously rises, the improvement of ductility with annealing starts to decrease as shown in Fig. 5.9. It increases for first step strains up to about 0.6. Considering the results presented in Fig. 5.9 it may be concluded that damage repair by annealing is effective only for values of first step strain below about 1 in this set of interrupted tests. The healing effect of recrystallisation and recovery due to annealing on lightly damaged material is significant and on heavily damage materials is low.

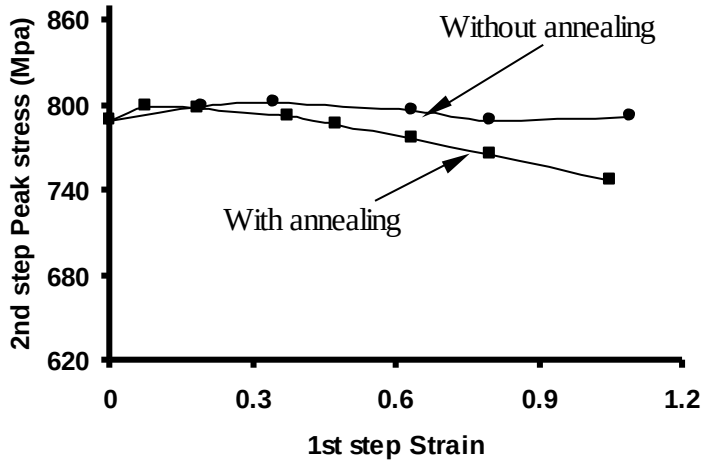

Fig. 5.10. Effects of first step deformations on second step peak stress with and without annealing.

Analysis of the effects of the strain in the first step on the second step peak stress is shown in Fig. 5.10, for annealed and unannealed test-pieces. The value of second step peak stress was not changed significantly, by changing values of first step strain, for unannealed test-pieces, as no microstructural change was introduced during the interruption in deformation. For an increase in first step strain values from zero to about 0.3, a slight increase in the value of second step peak stress occurs, but for higher, increasing values of first step strain, the value of second step peak stress reduces

steadily. Peak stress is likely controlled by grain size prior to second step tests and grain size will depend on static recovery, recrystallisation and perhaps grain growth, brought about by annealing. Dislocation density will increase during first step deformation and the lower the value of dislocation density the greater is the time needed to start and complete recrystallisation, for a given annealing temperature. Therefore, the increase of peak stress at low first step strain is a result of the incomplete restoration of microstructure, as to be effective, annealing requires a long time, due to low values of dislocation density. Thus the higher second step peak stress is due to the fine, distorted grains remaining in the test-pieces. The value of second step peak stress reduces with increasing values of first step strain higher than about 0.3. The reason is that dislocation density increases with increasing first step strain and this enhances the effect of annealing, leading to more complete recrystallisation and grain growth. Grain size has a dominant effect on peak stress, hence, the longer time for grain growth, (shorter time required for recrystallisation for high dislocation density), the larger grain size obtained during annealing, which decrease the second step peak stress.

5.3.3 Damage healing phenomena

It has been observed that the evolution of plasticity-induced damage within the specimen, and the mechanical response to annealing suggests that the heat treatment introduces a healing function. Therefore a further investigation was carried out to compare the effects of annealing on damage and damage healing using SEM. Examples of microstructures of test-pieces first step strained to a value of 1.0, presented in Fig. 5.11, show a high level of damage associated with inclusions, both before and after 60 minutes annealing at 700ºC.

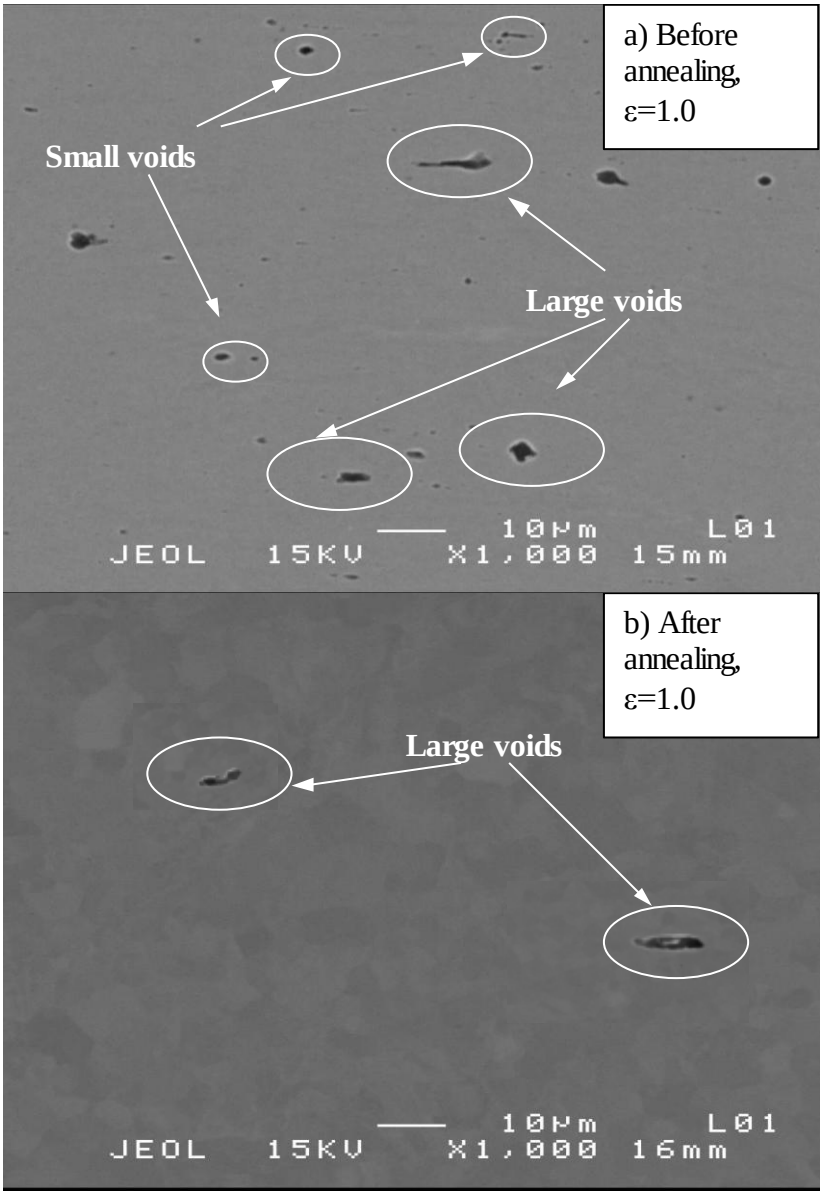

Fig. 5.11. Effect of annealing on damage evolution.

As seen in Fig. 5.11(a), for the unannealed specimen, large voids at the inclusion/matrix interfaces are elongated, with lengths of up to 10 µm. Also some small voids are present that probably have just been nucleated. After 60 minutes annealing at 700ºC, the damage remaining in the metal is significantly changed, as can be seen in Fig. 5.11(b). Only large voids (around 10 µm in size) remain. The small cavities (up to 10 µm in size) have disappeared. Under certain circumstances, for example a

recrystallisation front passing over the damage features will eliminate the locally high dislocation density. The density of dislocation is critical to the onset of damage. It is hypothesised that micro voids are nucleated at dislocation pile-ups occurring at interface of inclusions and matrix material. This could significantly alter the onset of damage coalescence, or slow down damage growth. Therefore, annealing could heal existing damage with enough time and sufficient temperature, but if damage exceeds a certain limit, the effects of damage healing are limited.

5.4 Effect of stress state on damage

Test-piece necking takes place with high first step deformation. This will affect damage evolution in the second step test due to the stress state effect. To identify the interaction of stress state with the evolution of damage mechanisms it is necessary to create and evaluate suitable experimental data.

5.4.1 Necking definition

Necking, in engineering or materials science, is a mode of tensile deformation where relatively large amounts of strain localise disproportionately in a small region of the material (Bridgeman, 1952). The resulting prominent decrease in local cross-sectional area is called a "neck". Because local strains in the neck are large, necking is often closely associated with yielding.

Necking results from an instability during tensile deformation and Considére (1885) published the basic criterion for necking in 1885. Three concepts provide the framework for understanding neck formation.

- Before deformation, all real materials have heterogenieties such as flaws or local variations in dimensions or composition that cause local fluctuations in stresses and strains. To determine the location of the incipient neck, these fluctuations need only be infinitesimal in magnitude.
- During tensile deformation the material decreases in cross-sectional area. (Poisson effect)
- During tensile deformation the material strain hardens. The amount of hardening varies with extent of deformation.

The latter two items determine the stability while the first item determines the neck's location.

5.4.2 Necking quantification

As deformation precedes the geometric instability causes strain to continue concentrating in the neck until the material either ruptures or the necked material hardens enough. Necking needs to be quantified geometrically to establish the effect of stress state on damage evolution. Fig. 5.12 shows an example of the quantitative relation between geometry and decreased cross-sectional area for a test-piece that forms a stable neck.

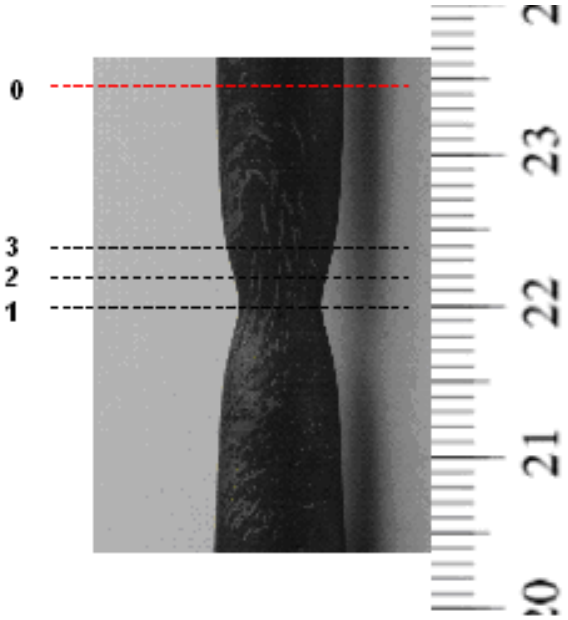

Fig. 5.12. Profile of necked test-piece.

As shown in Fig.5.12, diameters at three positions 0, 1, 2 and 3 were measured. Position 1 is the center of necked tes-piece where the minimum cross section area occured. Positions 2 and 3 are 2mm and 4mm away from position 1. Position 0 is 15mm away from center of necking which was considered to be reference position without necking. Necking can be quantified using three parameters N_1, N_2 and N_3, which are described in equation 5.1.

$$N_1 = \frac{d_{dia}{}^{1}}{d_{ref}}$$
$$N_2 = \frac{d_{dia}{}^{2}}{d_{ref}}$$
$$N_3 = \frac{d_{dia}{}^{3}}{d_{ref}} \qquad \textbf{5.1}$$

where $d_{dia}{}^{1}, d_{dia}{}^{2}, d_{dia}{}^{3}$ and d_{ref} are diameters of positions 1, 2, 3 and 0, respectively.

5.4.3 Necking validations

Fig. 5.13 shows the shapes of deformed test-pieces after first step tensile loading. Fig. 5.13(a) shows the original test-piece and Fig. 5.13(b) shows the test-piece with first step strain 0.2. Although the test-piece was stretched, the shape of test-piece still remains near cylindrical. Fig. 5.13(c) and d shows test-pieces with strain around 0.4 and 0.6, respectively. Small necking is visible in both centres of test-pieces. In Fig. 5.13(e), a failed test-piece is shown. It can be seen that flow localisation terminates the uniform deformation in the neck. Subsequently, failure occurs due to damage propagation inside the localised flow. The necking profile of test-piece has been interpreted in terms of true strain in axial direction.

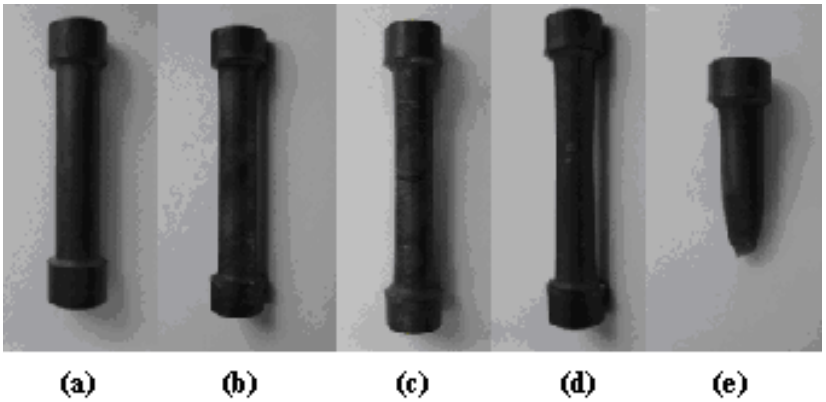

Fig. 5.13. (a) Original test-piece and deformed test-pieces with strain (b) 0.2, (c) 0.4, (d) 0.6 and (e) 1.78.

Necking has been quantified by equation 5.1, and results are shown in Fig. 5.14. It is obvious that differences between N_1, N_2 and N_3 with low first step strain are quite small. Significant differences arise for higher strain values. Necking results in stress

triaxiality that increased the effect of stress state on damage accumulation in second step deformation (Bridgman, 1946).

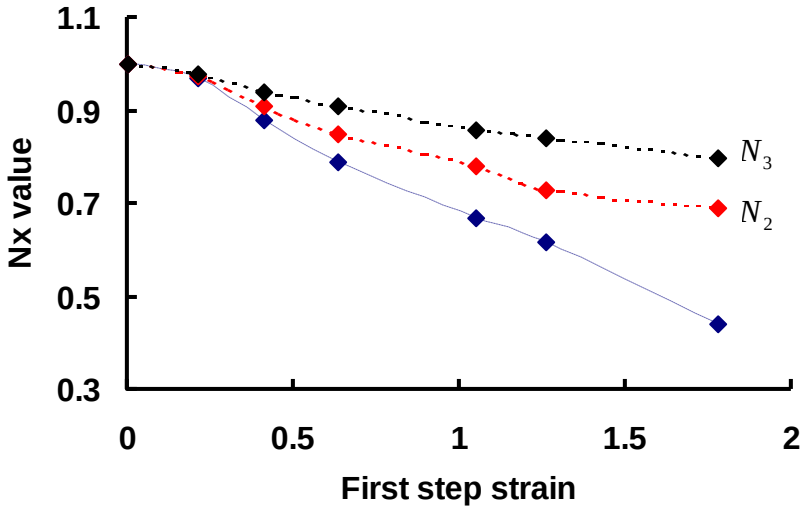

Fig. 5.14 Necking evolution against first step strain.

5.4.4 Stress-strain relationships

It has been shown that there is significant necking in test-pieces, creating large stress triaxiality, with high first step strain. The increasing effect of the stress state could affect the evolution of damage. To find the implication of this from a mechanical viewpoint, the mechanical responses of necked and un-necked test-pieces are compared.

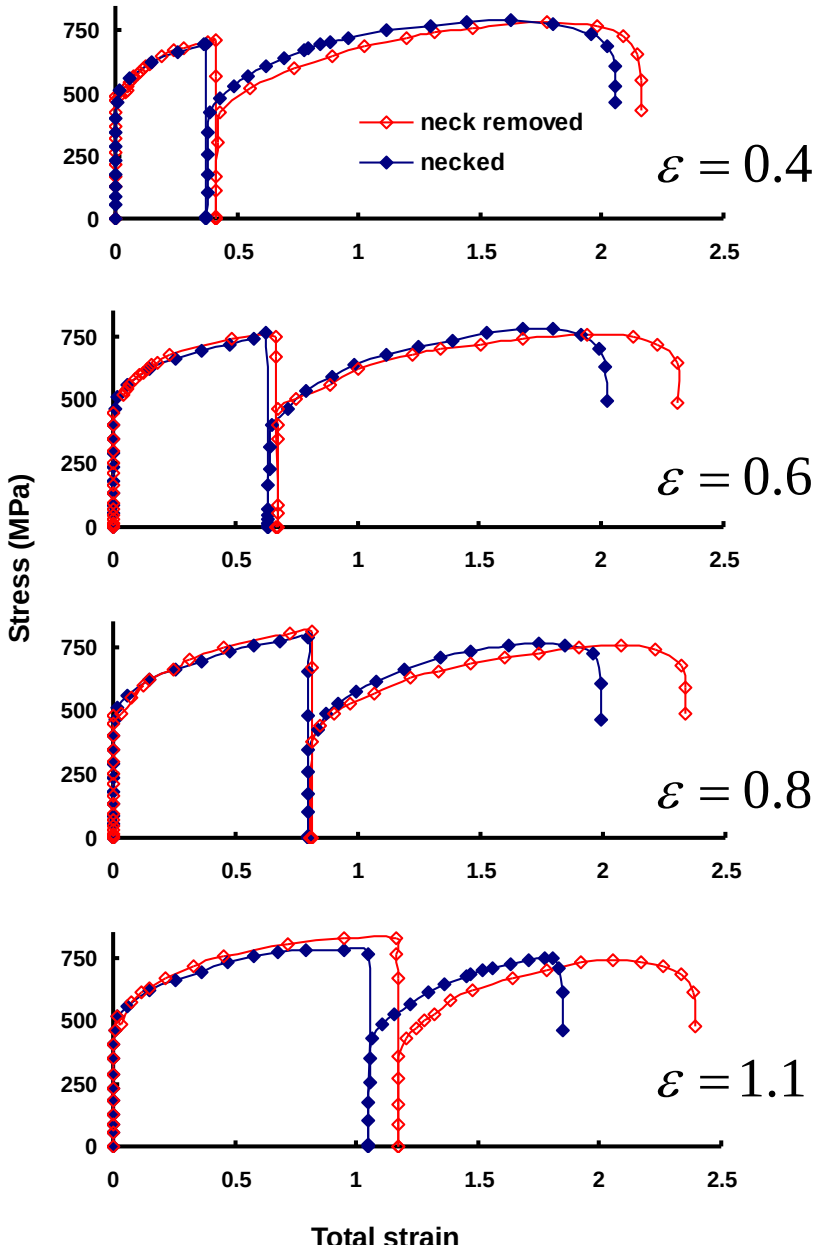

Fig. 5.15 Flow stress results with necked (blue) and un-necked (red) test-pieces prior to second step deformation.

Four pairs of stress-strain relationships plots obtained from test-pieces, necked and un-necked, prior to second step deformation, are shown in Fig. 5.15. Similar ductility, for each type of test-piece, was obtained for a first step strain at around 0.4, as necking was not significant (Fig. 5.14). Then the differences of second step ductility between necked

and un-necked test-pieces increased with higher first step deformation and second step ductility improved significantly when necking was removed, although peak flow stress remained similar in all cases. With first step strain around 1.1, the second step un-necked test-piece ductility improved nearly 40% compared to that for the one with necking. This may due to the fact that necking created high stress triaxiality and the stress state was affecting the damage evolution, which affects the strain to failure. And the damage accumulation was slowed down by neck removing due to decreased stress triaxiality.

In order to quantify these features, second step fracture strains have been plotted in Fig. 5.16 against necking created in first step deformation. It is obvious that ductility in step 2 of an un-necked test-piece is greater, mainly due to lower stress triaxiality. Meanwhile, the improvement with first step high-necked test-pieces is normally better than those with low necking. That indicated the increasing effect of the stress state accelerates the evolution of damage and lead the material failure faster.

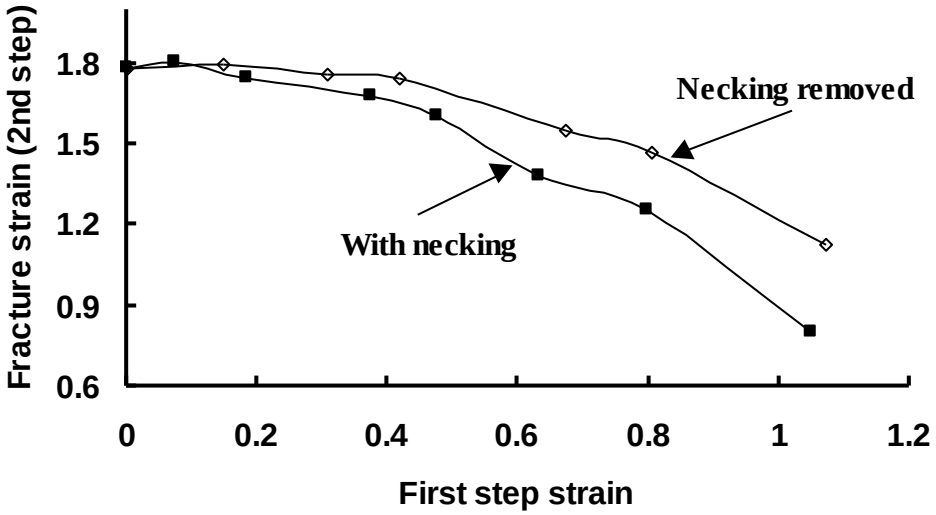

Fig. 5.16 Effects of first step deformations on second step fracture strains with and without necking.

5.5 Summary

Experimental stress-strain relationships have been obtained over a range of interrupted tensile tests. The results of step deformation mechanical tests and microstructure examination show that it is possible to recover or even improve the mechanical properties of cold formed UOE linepipe steel using an appropriate annealing process. For certain annealing times, the mechanical properties of the processed material can be better than that of the original material. This is not only due to the reduction in dislocation density and micro-damage, but also the refinement of grain size due to recrystallisation.

The existence of inclusions in the steels leads to a phenomenon of plasticity-induced damage in cold tensile tests. The results of interrupted tensile tests show that the healing effect of recrystallisation and recovery in lightly damaged steel is significant and on heavily damaged steel is limited. The heavily damaged material may benefit

from this healing due to recrystallisation and grain growth if the physical size of damage exceeds a certain limit. However, the upper limit of damage, which can be healed, remains un-quantified. Localised straining due to existed necking accelerates damage evolution. An optimum combination of value first step strain and annealing time determines the best cold formability in the second step. A reduction in grain size improves cold ductility and strength. Grain growth during annealing reduces flow stress and ductility in subsequent deformation. The material may gain an improvement if the test-piece has a proper deformation and interrupted time.

CHAPTER 6

Unified viscoplastic damage constitutive equations

6.1 Introduction

In this chapter, modelling approaches are reviewed and characterisation of material behaviour is discussed. Tailored viscoplastic damage constitutive equations are created, which account for the material behaviour observed in Chapter 5. This enables the evolution of the material microstructure to be mapped during heat treatment and the mechanical properties of cold-formed linepipe steel to be predicted after heat treatment. This set of constitutive equations is determined for a linepipe steel using an Evolutionary Programming (EP) optimisation technique. Finally, the influence of stress state on material properties is discussed.

6.2 Approaches to modelling

As a result of scientific preference and industrial needs in modelling material deformation, a number of modelling approaches have been used in past decades, which are summarised in the following sections.

6.2.1 Empirical methods

A traditional approach to describe material behaviour is to use extensive experimentation, and to capture the behaviour by empirical equations or graphs. For example, recrystallisation behaviour has been described by a power law functions of the process parameters in hot deformation (Sellars, 1990; McLaren and Sellars, 1992). The heat treatment response of steels is extensively reported by means of continuous

cooling transformation (CCT) diagrams, mapping phase transformations as a function of cooling rate, for instance (Atkins, 1978). Frequently knowledge of microstructure is not important if only mechanical properties are of importance. The problem with these methods lies in their limited predictive power and their dependence on extensive experimentation (Grong and Shercliff, 2002).

6.2.2 Advanced statistical methods

Based on extensive empirical data in some areas of metals processing, the application of advanced statistical methods, such as artificial neural networks have been developed to model the material behaviour. Vermeulen et al. (1996) predicted Jominy hardness profiles of steels using an artificial neural network, and the application of neural network approaches was used to predict microstructural evolution during hot forging (Brooks and Sabin, 2001). Compared with traditional empirical approaches, advanced statistical methods are more versatile, since large numbers of input variables can be handled. The success of the approach still depends on the availability of extensive, high quality data, but the method offers great potential to the linking of processing parameters, composition and properties. It is of great value for identifying underlying trends in complex multi-parameter data sets, reducing the volume of experimentation needed, or for testing hypotheses reached from a physically based approach. However, some physical metallurgists regard these new approaches with deep suspicion, since they offer no physical insight (Grong and Shercliff, 2002).

6.2.3 Physically based state variable methods

Theoretical modelling is intended to describe mathematically the physical phenomena resulting from thermo-mechanical processing, since changes in physical phenomena are the essential outcomes of heat treatment. This applies both to the evolution of microstructure with time or strain, and the dependence of mechanical properties on microstructure (Ashby, 1992). A physically based approach attempts to describe both thermo-mechanical history and resulting physical phenomena of metals, in terms of a small number of internal state variables. The internal state variable approach offers a good compromise between the many conflicting requirements for broad application to industrial process modelling (Grong and Shercliff, 2002). This method is capable of capturing some of the inherent complexity in a process, and achieving acceptable accuracy, for expenditure of acceptable computational effort. A physically based approach instils greater confidence than an empirical method for predicting the behaviour under conditions which are outside the range of conditions that have been explored experimentally, and provides potential for enhancing scientific understanding. For industrial applications, models must be simple enough to be implemented as fast subroutines in a numerical finite element or finite difference code (Grong and Shercliff, 2002).

6.2.4 Integral formulation of a model

Constitutive models aim to capture the interrelationship of critical process variables, which act to alter the mechanical or material response. The phenomenological approach has been used to create a model that provides insight into the microscopic mechanisms that act to cause changes in the material's macroscopic response. It is believed that this modelling method gives the insight necessary to validate results and facilitates the

extrapolation to new loading states (Cocks, 2001). By using this technique the resulting models are simple and clear in their formulation and can be easily understood by users. They are based on material constants that can be determined inexpensively from data sets generated on a range of widely available test machines. Another advantage of these modelling techniques are that new phenomena can be modelled before detailed work, on tooling and equipment, is carried out, which can reduce lead time and cost to implementation.

In this thesis, the work of Lin et al. (2007) is adopted to account for the material behaviour observed in Chapter 5, creating a tailored, physically based equation set. In the case of cold working and subsequent annealing, understanding of microstructural evolution and interaction between microstructure and macroscopic response of the steel, in different operational stages, is vital. The state variables with respect to deformation (or strain), considered during cold forming processes, are dislocation density and damage accumulation. In modelling annealing operations, the microstructural evolution can be described mathematically in terms of incremental variation of a number of state variables with respect to annealing time. The increments may then be integrated, step by step, through the whole operation, using an appropriate numerical procedure. Such a computation can be used to predict the microstructural evolution during both cold deformation and annealing.

6.3 Viscoplastic constitutive model

Constitutive equations for plasticity have been developed for many metals (Dunne et al., 1997 and Farrugia et al., 1999). The equations enable a wide range of phenomena to

be modelled, such as strain hardening, stress relaxation and microstructural evolution. In this section a dislocation density driven incremental-plasticity model is formulated in terms of the flow rule, work hardening and normalised dislocation density. This work forms part of the development of a set of unified viscoplastic constitutive equations to model the evolution of recrystallisation, dislocation density, strain hardening and grain size, to rationalise their inter-relationships and effects on plastic flow of material.

6.3.1 Flow rule

The deformation of a yielding body with an imposed stress will consist of a recoverable part (elastic strain) and permanent part (plastic strain). Summation gives the total strain induced:

$$\varepsilon_T = \varepsilon_e + \varepsilon_p \qquad \textbf{6.1}$$

where ε_T, ε_e and ε_p are total strain, elastic strain and plastic strain, respectively. From Hooke's law, assuming linear elasticity, stress can be related to elastic strain in the usual way:

$$\sigma = E\varepsilon_e \qquad \textbf{6.2}$$

where E is Young's modulus.

The flow rule describes the relationship between the flow stress and the plastic flow rate, incorporating factors such as the initial yield and material hardening due to the

interaction of dislocations. In the model developed in this work, plastic strain is the general term given to both rate-independent and rate-dependent inelastic material strain.

The classical strain hardening law $\sigma = K\varepsilon_p^n$ (in which K (strength factor) and n (strain hardening exponent) are material constants) is an empirical approximation and has no physical base. It has several shortcomings that must be reviewed. Material yield is not considered, yet in practice a defined yield stress, or stress band, exists. Secondly the flow rule is incapable of predicting material softening, which often arises and can clearly be seen in the tensile results presented in Chapter 5. To overcome these weaknesses, the strain hardening parameter ε_p^n is substituted for an additive form derived from a mechanical viewpoint.

With reference to Fig. 6.1, the material has a yield point k. The stress potential able to create viscoplastic material flow can be expressed as $(\sigma - k)$ where the bracketed term is used to indicate that only positive results are valid. After straining has commenced, dislocation trapping has hardened (increased the flow stress) the material by an amount R. The stress potential for viscoplastic flow σ_v, will be reduced to $(\sigma - k - R)$. Thus the flow rule can be formulated to relate directly to isotropic hardening and the initial yield:

$$\dot{\varepsilon}_p = \left\langle \frac{(\sigma - k - R)}{K} \right\rangle^n \qquad \textbf{6.3}$$

This form has been used to create additive viscoplastic models (Lemaitre and Chaboche, 1990), superplasticity constitutive models (Cheong, 2002) and a uniaxial, isotropic simplification of the form initially proposed by Rice (1970).

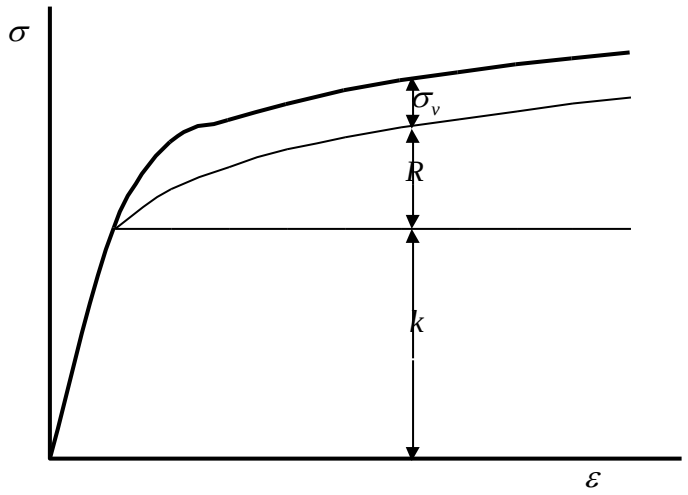

Fig. 6.1. Schematic of the decomposed stress components.

6.3.2 Isotropic work hardening law

Lin and Liu (2003) have modelled isotropic material hardening as having a linear relationship with normalised dislocation density in previous work:

$$\dot{R} = B \cdot \dot{\bar{\rho}} \qquad \textbf{6.4}$$

This is based on a first approximation to hardening, whereby the increase in yield can be directly (and linearly) attributed to the dislocation density. In practice, refinement is needed to predict the asymptotic hardening observed with increasing strain.

As discussed earlier, formation and movement of dislocations occur due to plastic straining. Work hardening occurs because some fraction of previously mobile dislocations remains locked in the material lattice and reacts with other dislocations, forming new obstacles to dislocation slip (Kocks, 1976). The strain required to cause dislocation slip is heavily influenced by the length over which a dislocation can move, the dislocation slip length l. As the density of dislocations increases the slip length reduces and a higher stress level is required to induce plastic deformation (Nes, 1998). Relating this to hardness, the hardening factor R is directly related to the reciprocal of the average slip length. In turn, the mean slip length is governed by the inverse square of the dislocation density $\rho^{-1/2}$ (Nes, 1998). In the work presented here, a normalised dislocation density $\bar{\rho}$ is used as a practical expression of the material's dislocation state (further details are given in Chapter 3). Considering this, the isotropic hardening effect rate, defined as the increase in the static yield surface above the initial yield point can be described as:

$$\dot{R} = \frac{1}{2} \cdot B \cdot \bar{\rho}^{-1/2} \cdot \dot{\bar{\rho}} \qquad \textbf{6.5}$$

It should be noted that although termed a hardening law, the model does allow for material softening resulting from a reduction in the dislocation density.

6.3.3 Formulation of unified constitutive equations

For the convenience of modelling the mechanisms and phenomena described above, and for steel deformed at room temperature, combined with microstructural evolution

during annealing (developed in Chapter 3), a set of unified constitutive equations have been formulated to predict mechanical properties after cold deformation and recovery after heat treatment. These are given below.

$$\dot{\varepsilon}_p = \left[\frac{(\sigma - k - R)}{K}\right]^n \cdot \left(\frac{d}{d_0}\right)^{\gamma} \quad \textbf{6.6}$$

$$\dot{R} = \frac{1}{2} \cdot B \cdot \bar{\rho}^{-1/2} \cdot \dot{\bar{\rho}} \quad \textbf{6.7}$$

$$\dot{\bar{\rho}} = k_1 \cdot (1 - \bar{\rho}) \cdot \left|\dot{\varepsilon}_p\right|^{\delta_1} - C_r \cdot \bar{\rho}^{\delta_2} - \frac{C_S \cdot \bar{\rho}}{1 - S} \dot{S} \quad \textbf{6.8}$$

$$\dot{S} = H \cdot \left[x \cdot \bar{\rho} - \bar{\rho}_c \cdot (1 - S)\right] \cdot (1 - S)^{\lambda_1} \quad \textbf{6.9}$$

$$\dot{x} = X_1 \cdot (1 - x) \cdot \bar{\rho} \quad \textbf{6.10}$$

$$\dot{d} = G_1 \cdot \left(\frac{d_0}{d}\right)^{\psi_1} - G_2 \cdot \dot{S} \cdot \left(\frac{d}{d_0}\right)^{\psi_2} \quad \textbf{6.11}$$

$$\sigma = E \cdot (\varepsilon_T - \varepsilon_p) \quad \textbf{6.12}$$

6.4 Viscoplastic-damage constitutive model

This section is concerned mainly with the development of mechanism-based damage equations to model damage evolution in cold deformation and its effect on material behaviour. The viscoplastic constitutive model is expanded to incorporate the damage nucleation, growth and coalescence mechanisms observed in Chapter 5.

6.4.1 Mechanistic framework

In cold forming operations, the mechanical behaviour of metals varies considerably with dynamic microstructural changes. The occurrence of material failure indicates an operation limit, for particular loading conditions. In general, steels mainly experience two physical phenomena under cold deformation conditions, strain hardening and damage softening. From a microstructural point of view, time dependent deformation is governed by a properly corresponding of hardening, due to accumulation of dislocations. For simple experimental analysis of macro softening effects due to damage, it is possible to compare uniaxial tensile and uniaxial compression tests. If it is assumed that the compressive specimen is damage free, then the difference between tensile and compressive flow stress plots will be equal to the damage softening effect. This is illustrated in Fig. 6.2

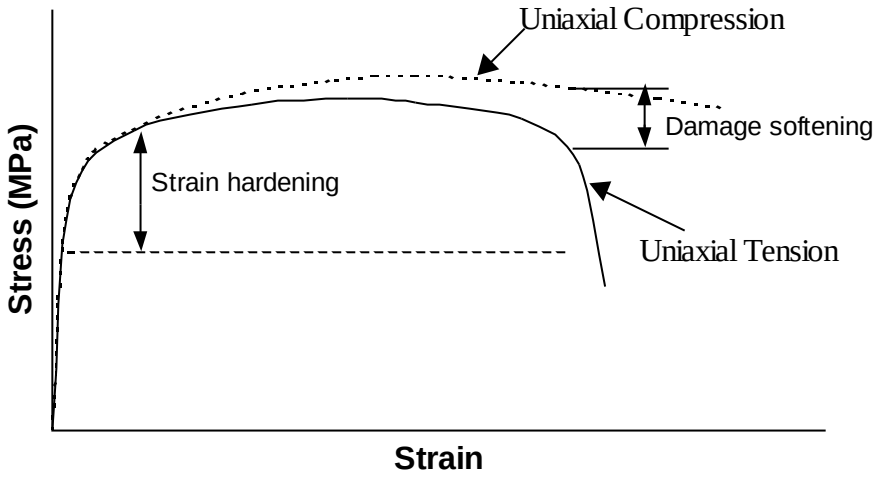

Fig. 6.2 Variation in flow stress (ideal).

6.4.2 Assumptions

To avoid unnecessary over complication, the principal of Ockham's Razor was used in formulating the damage theory, whereby the simplest possible assumption is applied at

each deformation stage. Splitting damage evolution into three linked phenomena produced continuum-modelling laws: inclusion-related damage nucleation, growth and coalescing existing damage. Gurson (1997) has proposed a general expression by decomposing damage evolution in terms of these three phenomena, which has successfully been adopted to describe damage (Dunne and Katramados, 1998). Experimental results in Chapter 5 suggest that damage leading to failure is initiated by nucleation, comprising oval voids formed around debonded inclusions. Failure occurs soon after damage growth leading to coalescence, whereby cracks form between existing voids. Damage growth and coalescence are continuum mechanisms and are similar. Tvergaard and Needleman (2001) treated damage coalescence as an augmented form of damage growth. Therefore, damage growth and coalescence can be modelled as the same phenomenon in this thesis. Based on the idea, the following expression is proposed:

$$\dot{D}_T = \dot{D}_N + \dot{D}_G \qquad \textbf{6.13}$$

where $\dot{D}_T$ represent the rate of total damage. $\dot{D}_N$ and $\dot{D}_G$ denote the rates of nucleation and growth of inclusion-related damage, respectively.

It is assumed that the material is isotropic, obeys von-Mises criterion and damage evolution is also isotropic. The inclusions are uniformly distributed in the matrix material and the volume fraction is constant at macroscopic level.

6.4.3 Plasticity-induced damage

In the work presented here, inclusion-related damage acts to reduce the material strength, as the area fraction of hardened material is reduced by the enlarging voids (Liu, 2004). The density of dislocation is critical to the onset of damage. It is hypothesized that micro voids are nucleated at dislocation pile-ups occurring at interfaces of inclusions and matrix material. The dislocation structure developed during plastic deformation constitutes a driving force for microstructural evolution. When the path of a slip plane is blocked by the boundaries between inclusions and matrix, dislocations will pile up behind the barrier and cause a large localised concentration of stress (Lardner, 1974). Micro damage is created when the stress concentration become sufficient to break cohesive bonds between atoms. Le Roy et al. (1981) and Needleman (1987) formulated damage nucleation rate $\dot{D}_N$, which describes decohesion at inclusion/matrix interfaces:

$$\dot{D}_N = a_1 \cdot (1 - D_N) \cdot \dot{\bar{\rho}} \qquad \textbf{6.14}$$

where a_1 is a material constant. Damage nucleation rate is strongly related to the dislocation evolution rate. Experimental results in Chapter 5 suggest that damage could be healed during heat treatment. If recovery processes reduce the dislocation density, the likelihood of damage will be reduced (Foster, 2007). Therefore, Equation 6.14, for nucleation allows damage to be reduced due to decrease in dislocation density, in this case during annealing.

Damage growth and coalescence are highly influenced by plastic strain development during cold deformation. At higher levels of inclusion damage, it has been shown that

strain localisation occurs and this will speed up the rate at which dislocations build at existing damage sites. Straining will result in an earlier coalescence due to strain localisation caused by enlarging damage voids interacting. Finer grain size will slow down the damage growth rate due to straining (Dunne and Katramados, 1998). Based on the work by Lin et al. (2001), damage growth rate $\dot{D}_G$ is, associated with plastic deformation and grain size, along with the amount of total damage:

$$\dot{D}_G = a_2 \cdot \frac{D_T}{(1-D_T)^{n_1}} \cdot \left(\frac{d}{d_0}\right)^{n_3} \cdot \left|\dot{\varepsilon}_p\right|^{n_2} \qquad \textbf{6.15}$$

where n_1, n_2, n_3 and a_2 are material constants.

6.4.4 Modification of the flow rule

In order to accurately predict material failure, the model was expanded to incorporate damage mechanisms. The flow rule was modified to account for the internal reduction in cross section area caused by damage in the same way as is commonly used in creep laws (Dyson, 1988). The damage D_T reduces the area of load bearing material over which a macro stress σ is distributed. At a micro scale, the material is subjected to an augmented stress over the undamaged area $1-D_T$ creating an effective stress for plastic deformation of, $\sigma/(1-D_T)$. The flow rule is modified thus:

$$\dot{\varepsilon}_p = \left[\left(\frac{\sigma}{(1-D_T)} - R - k\right)\Big/ K\right]^n \cdot \left(\frac{d}{d_0}\right)^{\gamma} \qquad \textbf{6.16}$$

6.4.5 Viscoplastic damage constitutive equation set

The constitutive equation set can now be expanded to include damage:

$$\dot{\varepsilon}_p = \left[\left(\frac{\sigma}{(1-D_T)} - R - k\right)\Big/ K\right]^n \cdot \left(\frac{d}{d_0}\right)^{\gamma}$$

$$\dot{R} = \frac{1}{2}\cdot B \cdot \bar{\rho}^{-1/2} \cdot \dot{\bar{\rho}}$$

$$\dot{\bar{\rho}} = k_1 \cdot (1-\bar{\rho}) \cdot \left|\dot{\varepsilon}_p\right|^{\delta_1} - C_r \cdot \bar{\rho}^{\delta_2} - \frac{C_S \cdot \bar{\rho}}{1-S}\dot{S}$$

$$\dot{S} = H \cdot \left[x \cdot \bar{\rho} - \bar{\rho}_c \cdot (1-S)\right] \cdot (1-S)^{\lambda_1}$$

$$\dot{x} = X_1 \cdot (1-x) \cdot \bar{\rho}$$

$$\dot{d} = G_1 \cdot \left(\frac{d_0}{d}\right)^{\psi_1} - G_2 \cdot \dot{S} \cdot \left(\frac{d}{d_0}\right)^{\psi_2}$$

$$\dot{D}_N = a_1 \cdot (1-D_N) \cdot \dot{\bar{\rho}}$$

$$\dot{D}_G = a_2 \cdot \frac{D_T}{(1-D_T)^{n_1}} \cdot \left(\frac{d}{d_0}\right)^{n_3} \cdot \left|\dot{\varepsilon}_p\right|^{n_2}$$

$$\dot{D}_T = \dot{D}_N + \dot{D}_G$$

$$\sigma = E \cdot (\varepsilon_T - \varepsilon_p) \qquad \textbf{6.17}$$

6.5 Determination of material constants

The equation set contains a total of 23 material constants $k, K, n, \gamma, B, k_1, \delta_1, \delta_2$, $C_r, C_S, H, \bar{\rho}_c, \lambda_1, X_1$, $G_2, G_1, \psi_1, \psi_2, a_1$, a_2, n_1, n_2 and n_3, the values of which have been determined from experimental material data. Using an advanced Evolutionary

Programming (EP) based optimisation method (Li et al., 2002), to produce an accurate fit of the model and experimental results.

6.5.1 Semi-empirical approach

Using the tension flow stress data presented in Chapter 5, upper and lower bounds for the material constants were determined. The term semi-empirical has been chosen for this strategy, as for some bounds, analytical techniques may be used to gain a first approximation (Lemaitre and Chaboche, 1990). Therefore, it is important to estimate lower and upper bounds for the constants based either on their individual physical meanings, or rules within the equation set and/or experience. For example, the values of constants, K and n affect the flow stress levels and viscoplastic behaviour of the material, respectively, at the initial stage of deformation. To minimise the viscoplastic effect of the metal deforming at 20ºC, a high n value is chosen ($n = 30$) in Equation 6.16. A high value of K, which normally ranges from 10 to 1000, results in a higher flow stress value, depending on temperature and material. A high n-value reduces the strain rate effect on material flow. The constant B in Equation 6.7 characterises the effect of dislocation density on the hardening of the material, its value should be within a range 10 to 1000 for most of materials. The value of k_1 affects the slope of hardening in stress-strain curves. Another example is the determination of boundary values for constants, a_1 and a_2, in damage Equations 6.14 and 6.15. The first one (in Equation 6.14) is used to control damage nucleation rate, which influences the softening of the material due to damage. a_2 in Equation 6.15 is used to model damage growth, thus the failure of the material. Their boundary values are estimated initially and modified

according to the experience gained during the determination of the equations. The final lower and upper bound values for the constants are listed in Table 6.1. They were determined using an EP-based optimisation method, as described in the next section.

Constant	Lower Bound	Upper Bound	Determined Value
K (MPa)	100	500	140
γ (–)	16.0	20.0	19.13
k (MPa)	320	420	362
B (MPa)	500	1000	758
k_1 (–)	1.0	2.0	1.77
δ_1 (–)	1.1	2.2	1.3
a_1 (–)	0.06	1.0	0.2
a_2 (μm^{-1})	9.0	11.0	10.01
n_1 (–)	9.0	20.0	14.2
n_2 (–)	1.0	2.5	1.92
H (s^{-1})	14.0	24.0	20.25
$\overline{\rho}_c$ (–)	0.005	0.05	0.015
λ_1 (–)	6.0	12.0	10.8
X_1 (s^{-1})	70.0	100.0	96.7
G_1 (μm)	0.0001	0.001	0.00075
ψ_1 (–)	2.5	3.5	3.08
G_2 (s^{-1})	8.0	16.0	12.91
ψ_2 (–)	1.0	2.5	1.5
C_r (s^{-1})	2.5	3.5	2.61
δ_2 (–)	2.0	4.0	2.92
C_S (–)	0.9	1.5	1.29
n_3 (–)	0.5	0.9	0.6

Table 6.1. Ranges and determined values of the material constants.

6.5.2 Numerical fitting technique

The evolutionary programming (EP) optimisation technique, used for determining these material constants, was based on minimising the residuals between the computed target

values and experimental data. The details of the optimisation method and the corresponding numerical procedure for this type of the problem are described by Lin and Yang (1999) and Li et al. (2002).

The determination of material constants within unified damage constitutive equations from experimental data can be formulated as a problem of finding the global minimum of a well defined objective function. However, such an objective function is usually complex, non-convex and non-differentiable. It is difficult to be optimised by classical gradient-based methods. Also, it is very difficult to choose starting values of the constants to obtain the global minimum by using traditional gradient descent methods (Lin & Yang (1999); Li et al. (2002)). Therefore, evolutionary programming (EP) was used in this work to solve the optimisation problem. The EP technique has generic features, overcomes the difficulty of choosing starting values for the constants, and provides a better chance to converge to the global minimum. The theories and the determination procedure are detailed by Cao and Lin (2008). The optimisation system, OPT-CE (Cao et al., 2006), as shown in Fig.6.3, contains 3 parts: Part 1 is to enable constitutive equations, boundary values of the constants and the corresponding experimental data to be input into the system. Part 2 is the EP optimiser. The constitutive equations need to be solved numerically via a numerical integration method. Differences between the model predictions and experimental data are assessed using a well-defined objective function. According to experience and recommendations given in the OPT-CE user manual (Cao et al., 2006), the control parameters for the EP-optimization are: population: 100, tournament: 50 and the number of generation: 100. Part 3 outputs the optimised material constants and the fitted results graphically.

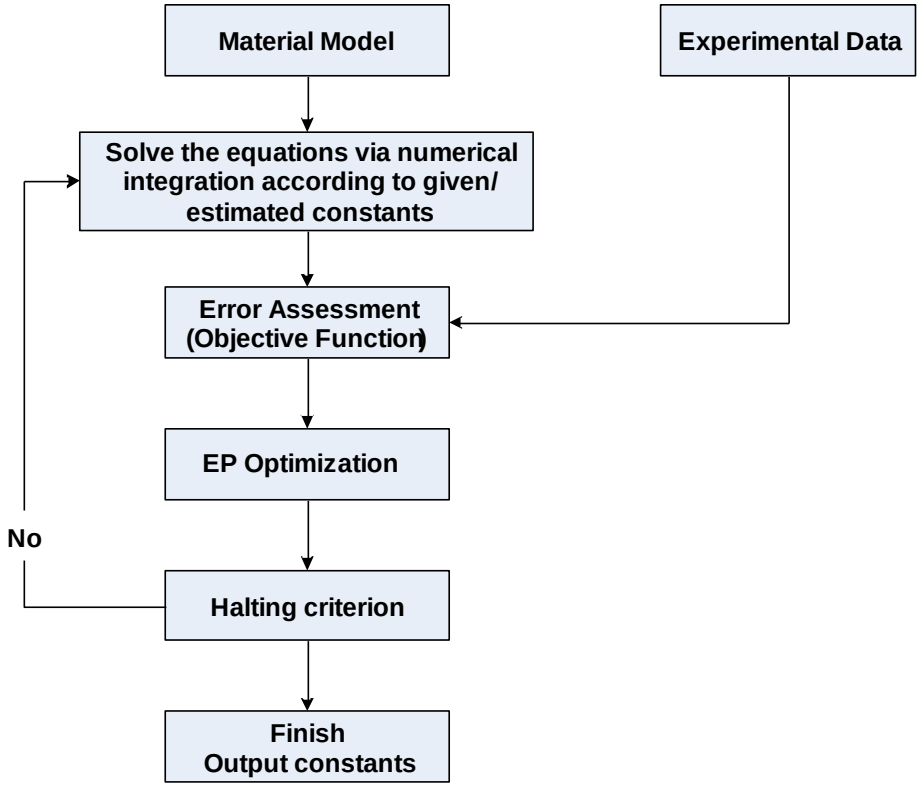

Fig. 6.3 Flow diagram of material constants determination procedures.

6.5.3 Determination of the constants

By using the described procedures the material constants were determined. The unified viscoplastic constitutive equations set, 6.17, were numerically integrated using an implicit integration method. The input was the strain rate and the initial values of state variables for equations. The output was stress and the integrated values of the state variables. In addition, the residuals and the fitting quality to experimental data from optimisation were also output. According to the experimental programme shown in (Fig. 4.7), the computational procedures include 3 key steps in correspondence with the mechanical-thermal-mechanical loading history of the tensile specimens in the experimental programmes as described in the previous section. During the first step,

tensile loading deformation at 20ºC, recrystallisation and grain size evolution would not take place and static recovery of $\bar{\rho}$ would not occur. To model these features, values of constants were set to: $C_r = 0$, $\dot{S} = 0$, $\dot{x} = 0$ and $\dot{d} = 0$, in the first step computation. The second step was to model phenomena arising during annealing. At this stage, due to the fact that there is no further deformation, the settings were; $\dot{\varepsilon}_T = 0$ and $\sigma = 0$. The last step computation was related to the second step tensile loading to failure at room temperature, after annealing. The computational settings used in this step were the same as those described for the first step. The computation was carried out in an iterative and incremental manner and was terminated when plasticity induced damage D_T reached 0.9.

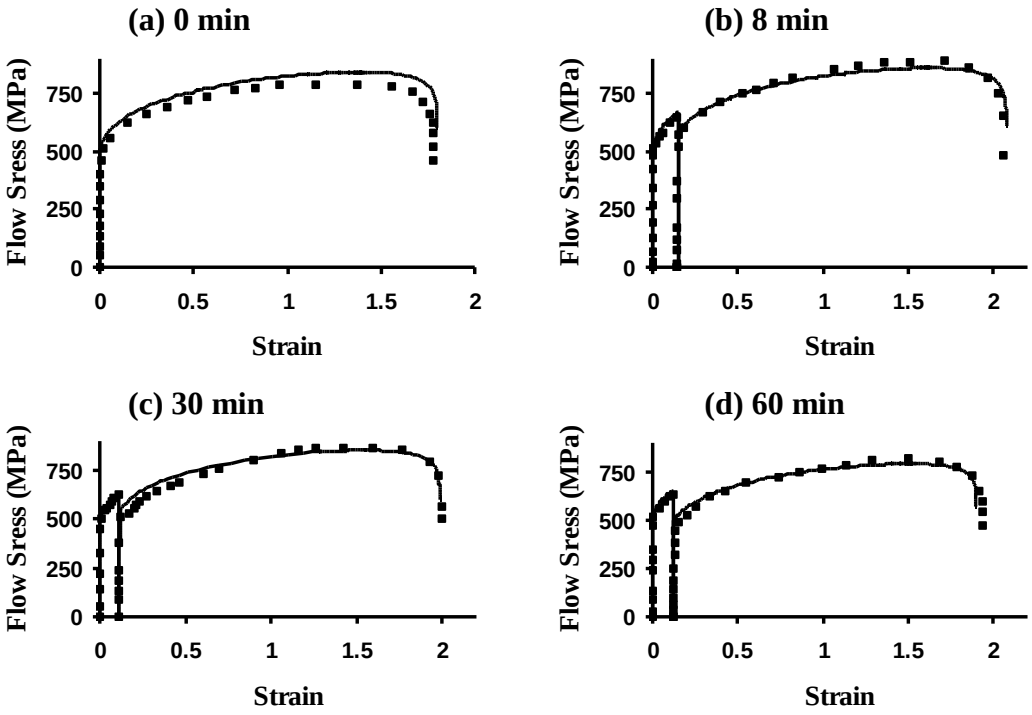

Fig. 6.4. Comparison of experimental (symbols) and computed (solid curves) stress-strain relationships for the interrupted tests with annealing periods of (a) 0, (b) 8, (c) 30 and (d) 60 min.

Fig. 6.4 shows a comparison of experimental (symbols) with computed (solid curves) stress-strain relationships for the interrupted tensile tests. The determined material constants are listed in Table 6.1. The computed data approximate closely to the experimental data. The fitted model is consistent with the test results, showing good accuracy in the computation of the material flow stress as well as strain to failure, for all conditions investigated. The computed strain at failure is within 5% of the experimental value, for all cases. The general trend exhibited by the strain at failure following reloading after annealing, are correctly fitted (Fig. 6.5) with predicted recrystallisation nucleation only marginally before the experimentally determined value. The annealing process can lead to recovery of mechanical properties through microstructural change, as seen in the experimental values of strain to failure.

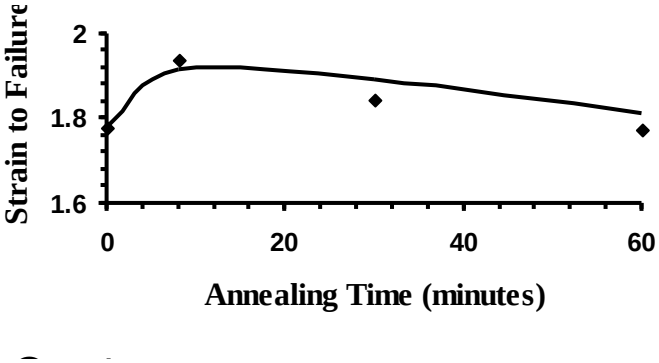

Fig. 6.5. Comparison of experimental (symbols) and predicted (solid curves) strains to failure at the 2nd step stretching against annealing time at 700°C.

6.6 Effects of material constants

The values of material constants (listed in Table 6.1) are valid for the particular steel composition and processing route. For example, ferrite recrystallisation evolution rate

varies from one alloy to another and is defined by the value of constant H. It affects the grain refinement process. However, for the same recrystallisation feature of metals, the process of new grain growth could be different, which affects the average grain size and is defined by the value of constant G_2. Detailed studies, to evaluate the sensitivity of the constants H and G_2, on microstructure evolution and mechanical property recovery during annealing, are described below.

During annealing, static recrystallisation takes place leading to the formation of new grains, thus playing an important role in microstructural evolution. Fig. 6.6 shows the effect of different H values (1.0, 20.25 and 100) on grain size variation, together with mechanical properties (strain to failure and peak stress) variations for different annealing times, for deformed steel, (first step strain at 0.4). The higher H value leads to higher and quicker recrystallisation, as can be seen by the effects on grain size evolution in Fig. 6.6(a). More recrystallisation takes place leading to more new grain formation and smaller average grain size, as modelled by Equation 6.11. Grain growth becomes the dominant mechanism when recrystallisation is complete. The mechanical properties, such as peak stress and strain to failure, are directly related to grain size evolution, as shown in Fig. 6.6(b) and (c). The predicted strains to failure and peak stress are higher for a higher value of H, and also are higher than those for original materials with one step deformation. This indicates that the strength and formability of the deformed material are improved by annealing, and increase with an increasing value of recrystallisation constant H.

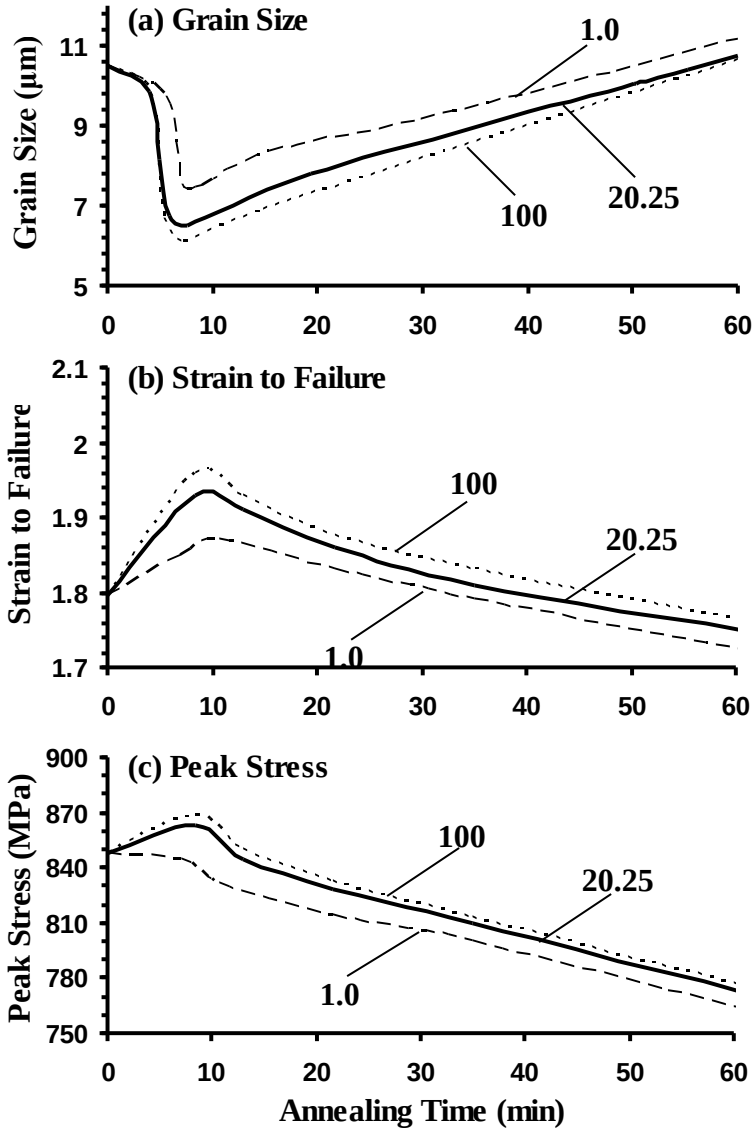

Fig. 6.6. Effects of H values on (a) grain size, (b) strain to failure and (c) peak stress after annealing.

While the annealing continues, for all cases, a competition between the static grain growth and the grain refinement due to recrystallisation tends to a dynamic balance. The parameter G_2 plays an important role to control the grain size evolution in Equation 6.11. The effect of changing values of G_2 from 1.9 to 12.9 to 19.9, are shown in Fig. 6.7. The other values of the constants were the same as given in Table 6.1, with

the first step strain at 0.4. While the G_2 value is small (G_2=1.9), grain size evolution is dominated by static grain growth. Recrystallisation will contribute to grain size refinement at higher values of G_2 (G_2=12.9, 19.9). Therefore, when G_2=1.9, the grain size remains almost constant during recrystallisation. The average grain size is smaller when a greater G_2 value exists, which is shown in Fig. 6.7(a). Fig. 6.7(b) and (c) represent the mechanical property responses for peak stress and strain to failure, which are directly affected by average grain size evolution. Both strength and formability of deformed material can be higher than the values for one step deformed material, as mechanical properties are recovered due to annealing. Also, higher peak stress and ductility are obtained when the G_2 value is larger. This is due to the fact that recrystallisation plays a more important role in refining average grain size when G_2 is large. Overall, it is noted that the predicted results demonstrate the real trends of micro and macro responses. This is due to the effective modelling of parameters within the constitutive equation sets. The whole model directly describes the mechanical property recovery due to microstructural evolution during annealing.

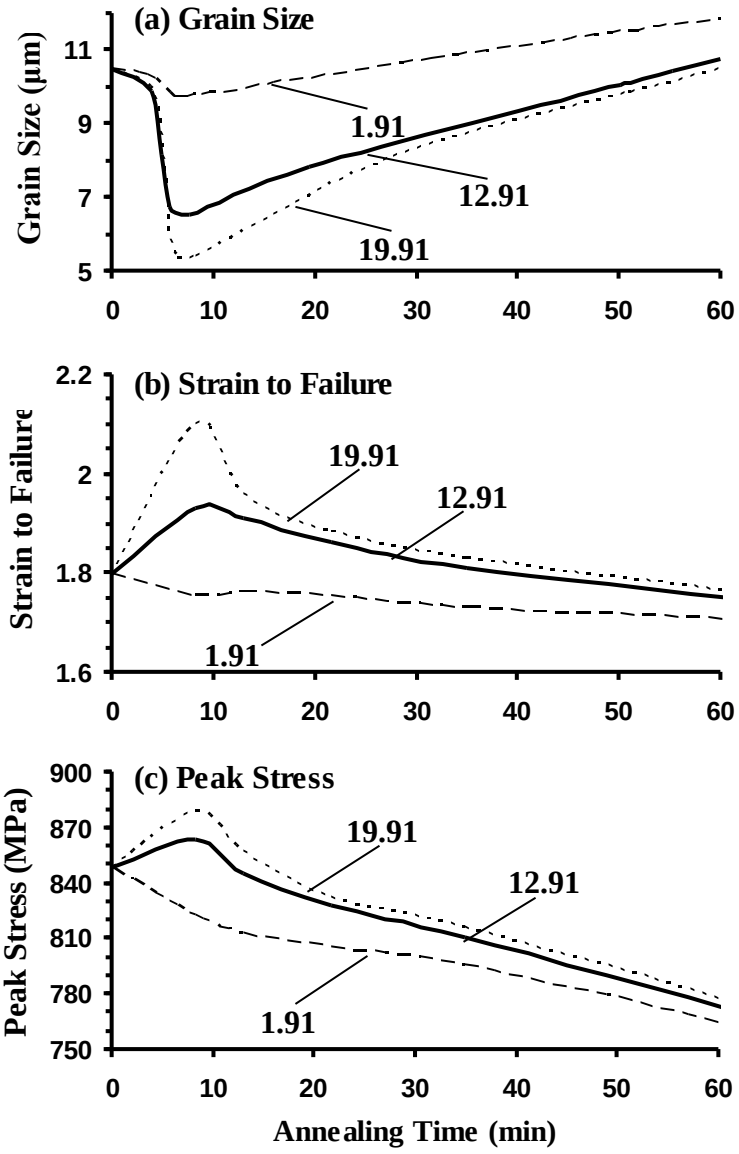

Fig. 6.7. Effects of G_2 values on (a) grain size, (b) strain to failure and (c) peak stress after annealing.

6.7 Predictions and Analysis

With determined material constants, the unified mechanism-based constitutive equations were used to predict microstructure evolution and recovery of mechanical properties by annealing. Also the mechanical response was predicted during cold

deformation after heat treatment. All the experimental and predicted results are for 60 minutes annealing time.

Experimental relationships of stress-strain, symbols in Fig. 6.8, for first step strain of 0.4, are compared with predicted values, the corresponding solid curves, and obtained using the constitutive equations with optimised constants. The predicted results are close to the experimental data. Close agreement exists for both steps of cold deformation. The final drop of the stress-strain curve, due to the material failure, also is well modelled. This indicates that the set of constitutive equations can describe the material behaviour during annealing and predict the mechanical response of annealed test-piece.

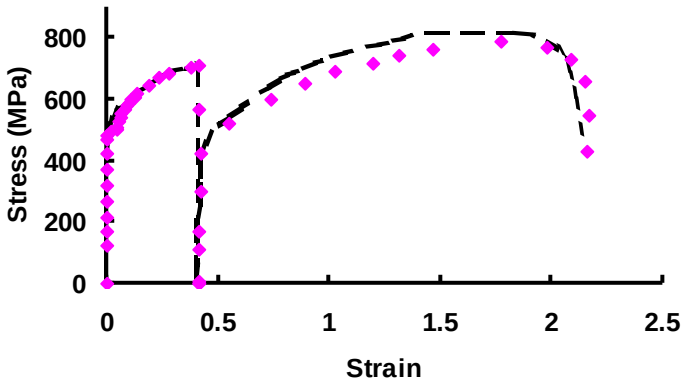

Fig. 6.8. Comparison of predicted (dash curves) and experimental (symbols) stress strain relationships for linepipe steel with first step deformation 0.4.

Fig. 6.9 shows a comparison of experimental with predicted material response for first step strain 0.6. From experimental records shown in Chapter 5, after a first step deformation strain of 0.6, incipient test-piece necking arises. A good fit of material

response is achieved although some discrepancy can be seen for material failure. The general trend of the model's results remains correct.

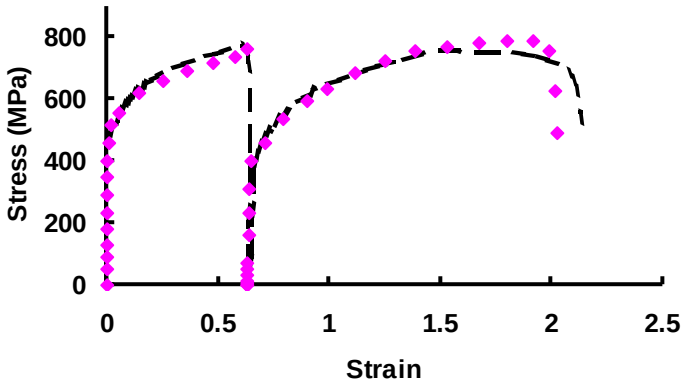

Fig. 6.9. Comparison of predicted (dash curves) and experimental (symbols) stress strain relationships for linepipe steel with first step deformation 0.6.

Fig. 6.10 shows high necking results for first a step strain of 0.8 and 1.1. Here, the fit of material ductility is poor. The equation set has failed to predict damage evolution and material failure satisfactorily in second step deformation. A similar, but lesser discrepancy is also present for the first step strain of 0.8. In this case, the error is due to the highly necked test-pieces formed during the first step and the consequent triaxial stress state not being accounted for in the current equation set.

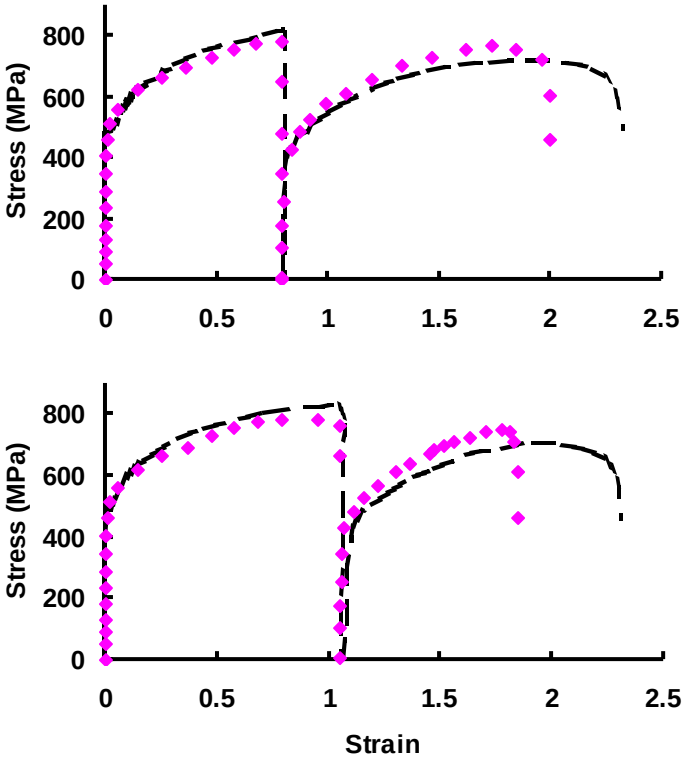

Fig. 6.10. Comparison of predicted (dash curves) and experimental (symbols) stress strain relationships for with first step deformation 0.8 and 1.1.

Damage evolution, especially damage growth and coalescence, are controlled by plastic strain. Localised straining accelerates damage growth and coalescence. As seen in Chapter 5, necking occurred during first step cold tension tests and led to high strain localisation. However, the results of uniaxial tensile tests were used in the current model without considering stress triaxiality and that slows down modelled damage accumulation and extends the ductility of deforming steel, as seen in Fig. 6.10. Therefore, the current unified constitutive equation set is good at predicting the uniaxial tensile characteristics but not for necked test-pieces. The observed results must be used to modify the model, to make it capable of accurately predicting damage and material failure in triaxial stress states. This is discussed to further detail in the next chapter.

6.8 Summary

The tension deformation of linepipe steel at room temperature and subsequent annealing process has been modelled using viscoplastic-dislocation-damage based laws derived here for uniaxial stress conditions. The model has been used to obtain a detailed description of the state (and evolution) of material microstructure. All laws have been derived with significant insight into the driving material mechanisms. For certain annealing times, the mechanical properties of the processed material can be even better than that of the original material. The success of the theoretical prediction provides an effective means for applying subsequent annealing to improve the mechanical properties of pipeline steel.

The current unified constitutive equations were not capable of predicting damage evolution when in highly necked test-pieces. Stress state parameters need to be considered in the current constitutive model to enable it to be used to accurately predict damage arising in stress states of high triaxiality.

CHAPTER 7

Stress-state modelling and integration with FE simulation

7.1 Introduction

In this chapter, a set of pre-necked test-pieces are described and used to study the influence of stress state on damage evolution. Common stress state parameters are reviewed and the most appropriate one selected. Based on the material model developed in Chapter 6, updated equations to predict the stress-state dependence of damage are formulated. A method of integrating the material equations with commercial FE software ABAQUS explicit is described. Following this, simulation results are used to evaluate the predictions.

7.2 Stress state dependents

The state of stress in notched (pre-necked) test-pieces is triaxial and analysis of notched bars was originally undertaken by Bridgman (1952). If necking occurs in an initially cylindrical test-piece the stress state will deviate from pure tension. Bridgman (1946) has presented a set of equations to predict the stress field in a necking test-piece, based on the instantaneous yield surface being constant throughout the necking region (Thomason, 1990). This indicates that for ductile materials, damage will nucleate and grow at the centre of the test-piece, creating the cup-cone feature apparent in some tensile test-pieces. Necked specimen tests on stainless steels show notched samples to have significantly less ductility than plane test-pieces (Tinet et al., 2004). Without further FE or classical stress state analysis, it is hard to quantify the effect of stress state

using the results generated, as the stress triaxiality is complicated and heavily influenced by notch size, notch radius etc and this is not fully appreciated in the study.

As discussed in Chapter 6, interrupted tensile tests provide data on recovery characteristics and the developed unified equations can well simulate the flow response and microstructural evolution under various heat treatments. However, the ductility of material during second step deformation was not simulated well using the current unified constitutive equations, due to the necked shape produced by increased first step deformation. The current model was unable to predict the pre-necked material, which experience variations in ductility and failure mode depending on the stress state. An updated equation set is required to analyse the effect of stress-state on damage evolution and this is described below.

7.3 Selection of appropriate stress state parameters

7.3.1 Review of stress state parameters within damage modelling

The most common stress state parameters within damage modelling are reviewed. The relationships between damage rate $\dot{D}^*$ considering stress state and damage rate $\dot{D}$ with uniaxial tension are generated. In general, damage equations concerned with the enlargement of discreet oval or spherical damage features, such as ductile damage (Rice and Tracy, 1969; Gurson, 1977) and power law creep damage (Cocks and Ashby, 1980) are controlled by the local stress triaxiality. FE analysis of a growing void supports this dependency on hydrostatic stress (σ_H) triaxiality (Needleman and Rice, 1980). Other stress state equations, such as those dictated by maximum principal stress

σ_1 (Lin et al., 2005) have been used in FE simulation and analysis and shown to be less satisfactory.

The effect of stress state on creep damage is often attributed to stress triaxiality, in which an increase in hydrostatic stress leads to a reduction in material ductility. Considered below is the triaxiality relationship proposed by Cocks and Ashby (1980), presented as change in damage rate relative to that in uniaxial tension:

$$\frac{\dot{D}^*}{\dot{D}} = \frac{\sinh\left(2\frac{(n_d - 0.5)}{(n_d + 0.5)}\frac{\sigma_H}{\sigma_e}\right)}{\sinh\left(\frac{2}{3}\frac{(n_d - 0.5)}{(n_d + 0.5)}\right)} \qquad \textbf{7.1}$$

where n_d is the stress exponent for steady state creep. It should be noted that when n_d is large, the equation is insensitive to small changes in its value. The single material constant makes the model extremely useable. The original formulation is derived from an analysis of a simple void within a continuum and so is valid for many damage types and deformation conditions.

Lin et al. (2005) have developed a model showing the influence of the maximum principal stress on creep damage rate. The ratio of σ_1/σ_e is used to correct the uniaxial damage rate for complex stress state.

$$\frac{\dot{D}^*}{\dot{D}} = \left(\frac{(\sigma_1 + |\sigma_1|/2)}{\sigma_e}\right)^{\gamma} \qquad \textbf{7.2}$$

Interestingly the exponent γ given above is a function of the maximum principal stress $\gamma = A\sigma_1$ where A is a material constant. This relationship is used to account for the observed deformation during creep.

Ductile damage, which may occur under complex strain paths, has attracted a considerable amount of work into the anisotropic modelling of damage (Brunig, 2002). In this case, the damage variable is generalised to form a damage area tensor **D**:

$$\mathbf{D} = \begin{bmatrix} D_{xx} & D_{xy} & D_{xz} \\ D_{yx} & D_{yy} & D_{yz} \\ D_{zx} & D_{zy} & D_{zz} \end{bmatrix} \qquad \textbf{7.3}$$

which in some special cases has the same meaning as the original variable (Abu Al-Rub and Voyiadjis, 2003). Thus, the anisotropic development of damage voids in a 3D space can be mapped.

Manjoine (1982), for Type 304 steel, has investigated the effect of stress state on the uniaxial strain at failure. Based on notched bar constant displacement rate testing of a range of material, the empirical relationship is derived:

$$\frac{\dot{D}^*}{\dot{D}} = 2^{\left(3\frac{\sigma_H}{\sigma_e} - 1\right)} \qquad \textbf{7.4}$$

The relationship between damage development and stress state is significant to forming processes. Rice and Tracey (1969) proposed the triaxiality relationship, relative to uniaxial damage rate as:

$$\frac{\dot{D}}{\dot{D}^*} = \exp\left(\frac{1}{2} - \frac{3\sigma_H}{2\sigma_e}\right) \qquad \textbf{7.5}$$

Here the effect on damage of the hydrostatic stress relative to effective stress is considered as highly non-linear. The expression has no material dependent constants and is only valid for triaxiality greater than 1.

Pilling and Ridley (1986) have assessed stress state behaviour of superplastic damage for the case of increasingly compressive stress state. Unlike other formulas, their equation allows damage to accumulate to some degree in compressive environments. The equation has been re-written by Nicolaou and Semiatin (2003) in terms of the stress triaxiality:

$$\frac{\dot{D}^*}{\dot{D}} = \left(\frac{1}{3} + 2\frac{\sigma_H}{\sigma_e}\right) \qquad \textbf{7.6}$$

Constitutive models have been developed specifically for hot deformation. Liu et al. (2005) have produced a complex but logical model capable of describing dislocation build up and associated material hardening and inclusion damage. The model maps the interaction of the various material mechanisms in a phenomenological manner. The

power law relationship proposed by Liu et al. (2005) can be given in normalised form as:

$$\frac{\dot{D}^*}{\dot{D}} = \left(\frac{3\sigma_H}{\sigma_e} \right)^n \qquad \textbf{7.7}$$

where n is the material constant.

7.3.2 Effects of stress triaxiality on damage

Fig. 7.1 shows the relationship between the relative damage rate $\dot{D}^*/\dot{D}$ and stress triaxiality predictable by various models over uniaxial tension. Uniaxial tension has a stress triaxiality of $1/3$.

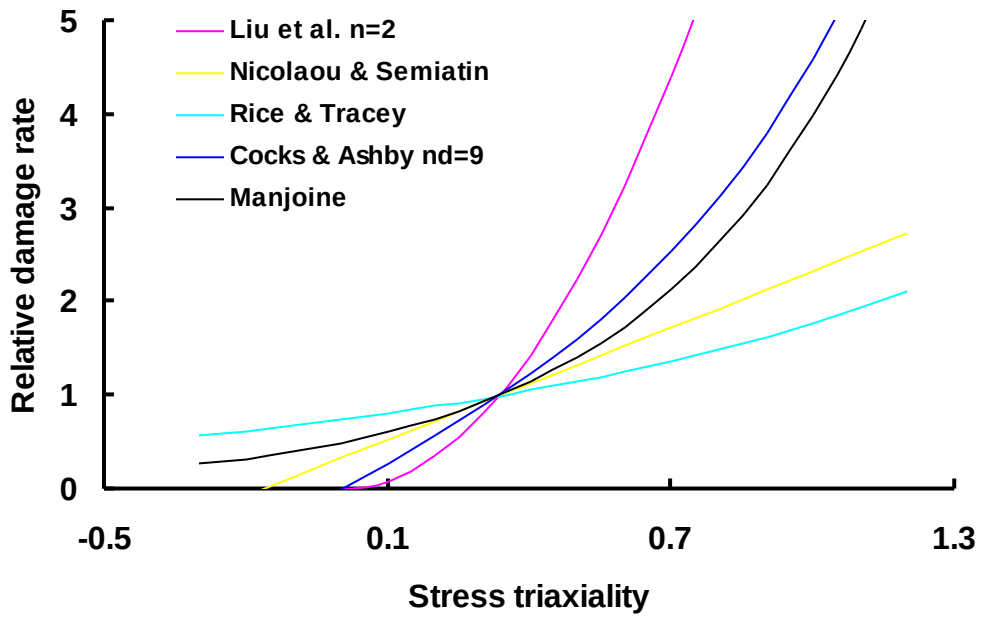

Fig. 7.1. Damage rates compared to uniaxial tension against stress triaxiality for Liu et al. (2005), Rice and Tracey (1969), Manjoine (1982), Cocks and Ashby (1982) and Nicolaou & Semiatin (2003) damage stress state factors.

Equation 7.1 developed by Cocks and Ashby (1982) predicts a near linear rise in damage with increasing stress triaxiality between 0 and uniaxial tension (0.33). When stress triaxiality increases, predicted damage rate is non-linear, that is in agreement with the strain to failure observed from the tensile tests. The use of material constant n_d allows flexibility to fit a material's individual damage characteristics (Foster, 2007).

The empirical relationship 7.4 developed by Manjoine (1982) considered damage under states of negative triaxiality. Damage was observed within negative stress states in hot rolled samples by Baker and Charles (1972). In general, it is accepted that in a negative stress state, no amount of matrix damage will accumulate, it is rationalised that although there is evidence of damage due to inclusion break up in negative triaxiality regions, this has little influence on the state of the matrix material and may not act to weaken the material.

The exponential relationship Equation 7.5 proposed by Rice and Tracey (1969) is for use only in high stress triaxiality regions ($\sigma_H/\sigma_e > 1$). It predicts far less triaxiality dependency than other models at $\sigma_H/\sigma_e < 1$ and significant damage development in negative stress triaxiality states.

The Equation 7.6 proposed by Nicolaou & Semiatin (2003) also considers damage under states of negative triaxiality. Linearity is predicted at higher stress triaxiality levels.

Using the power law relationship (Equation 7.7) proposed by Liu et al. (2005), very little damage is predicted for stress triaxiality less than pure tension ($<1/3$), especially when higher powers of n are used, as stress triaxiality increases damage rate grows rapidly due to the power law.

From the study of different stress state equations described above, Equation 7.1 was chosen to model the stress state dependence of inclusion related damage evolution.

7.3.3 Stress state dependent constitutive modelling

The original constitutive relationship (Equations set 6.17) could now be expanded to include stress state effects

$$\dot{\varepsilon}_p = \left[\left(\frac{\sigma_e}{(1-D_T)} - R - k \right) \Big/ K \right]^n \qquad \textbf{7.8}$$

$$\dot{R} = \frac{1}{2} \cdot B \cdot \bar{\rho}^{-1/2} \cdot \dot{\bar{\rho}} \qquad \textbf{7.9}$$

$$\dot{\bar{\rho}} = k_1 \cdot (1-\bar{\rho}) \cdot \left| \dot{\varepsilon}_p \right|^{\delta_1} \qquad \textbf{7.10}$$

$$\dot{D}_N = a_1 \cdot (1-D_N) \cdot \dot{\bar{\rho}} \qquad \textbf{7.11}$$

$$\dot{D}_G = a_2 \cdot \frac{D_T}{(1-D)^{n_1}} \cdot \left| \dot{\varepsilon}_p \right|^{n_2} \qquad \textbf{7.12}$$

$$\dot{D}_T = (\dot{D}_N + \dot{D}_G) \cdot \frac{\sinh\left(2 \frac{(n_d - 0.5)}{(n_d + 0.5)} \frac{\sigma_H}{\sigma_e} \right)}{\sinh\left(\frac{2}{3} \frac{(n_d - 0.5)}{(n_d + 0.5)} \right)} \qquad \textbf{7.13}$$

$$\sigma = E \cdot \left(\varepsilon_T - \varepsilon_p \right) \qquad \textbf{7.14}$$

For the purpose of stress state analysis for necked test-pieces during second step deformation, the equations describing microstructural evolution during heat treatment (static recovery, static recrystallisation and grain size evolution) were disregarded.

7.4 Explicit FE formulation

Explicit finite element analysis is traditionally used for dynamic simulations in which the kinetics of moving bodies cannot be ignored and thus implicit formulation is inappropriate. The numerical efficiency of a dynamic analysis can, in principal, result in a significant time saving advantage over a comparable implicit formulation. Dynamic formulation also offers simplicity when implementing new material models, as there is no need to formulate the Jacobian matrix. For these reasons the technique has been adopted for quasi-static problems (Prior, 1994; Rojek et al., 2001). During development stages, it offers further advantages in that analysis often continues to produce results after becoming unstable, making it easier to determine the cause of faults. Unfortunately potentially misleading results may be produced. As a result care must be taken to identify the validity of explicit results.

Equilibrium is not computed at each increment. Explicit analysis is based on a system of discrete equations of motion:

$$M \cdot \ddot{r} + D \cdot \dot{r} = f - p \qquad \textbf{7.15}$$

where M and D are the mass and damping matrices respectively, r is the nodal displacement vector and f and p are the external and internal force vectors. The calculation of mass-effects significantly restricts the time increment of FE increments, as the analysis will record pressure waves flowing through the material from dynamic mass displacement. The velocity of these pressure waves is governed by material mass density and the resulting time increment is usually small in comparison to the forming process (Prior, 1994). For forming processes, where the preservation of momentum has an insignificant impact on the result, mass scaling can be used to increase the time increment. The velocity of pressure waves is reduced due to artificially increased material density, and the time increment between FE calculations can be increased (Foster, 2007).

7.5 Generalised material flow rule

7.5.1 Von Mises criterion for different stress conditions

There are two classic yield criteria applied to the deformation of metals, as illustrated for the two-dimensional case in Fig. 7.2. The Tresca criterion assumes that plastic deformation occurs when a critical shear stress is reached. The Von-Mises criterion defines a critical shear-strain energy being reached. Both recognise that plastic deformation is fundamentally a shearing process, with the envelope of Tresca's theory being slightly more conservative (Foster, 2007).

In the case of uniaxial stress or simple tension, $\sigma_1 \neq 0$, $\sigma_2 = \sigma_3 = 0$, the von Mises criterion reduces to $\sigma_1 = \sigma_y$. Therefore, the material starts to yield, when σ_1 reaches the yield strength of the material σ_y, which is a characteristic material property. In

practice, this parameter is indeed determined in a tensile test satisfying the uniaxial stress condition.

In the case of pure shear stress, $\sigma_{12} = \sigma_{21} \neq 0$, while all other $\sigma_{ij} = 0$, von Mises criterion becomes:

$$\sigma_{12} = \frac{\sigma_y}{\sqrt{3}} \qquad \textbf{7.16}$$

This means that, at the onset of yielding, the magnitude of the shear stress in pure shear is $\sqrt{3}$ times lower than the tensile stress in the case of simple tension. The Von-Mises yield criterion for pure shear stress, expressed in principal stresses, is

$$(\sigma_1 - \sigma_2)^2 + (\sigma_2 - \sigma_3)^2 + (\sigma_1 - \sigma_3)^2 = 6{\sigma_{12}}^2 = 2{\sigma_y}^2 \qquad \textbf{7.17}$$

In a multi-dimensional stress space the yield point is normally attributed to a function for the three-dimensional stress state acting on the material. The yield criteria define equivalence between the complex stress state and the uniaxial description.

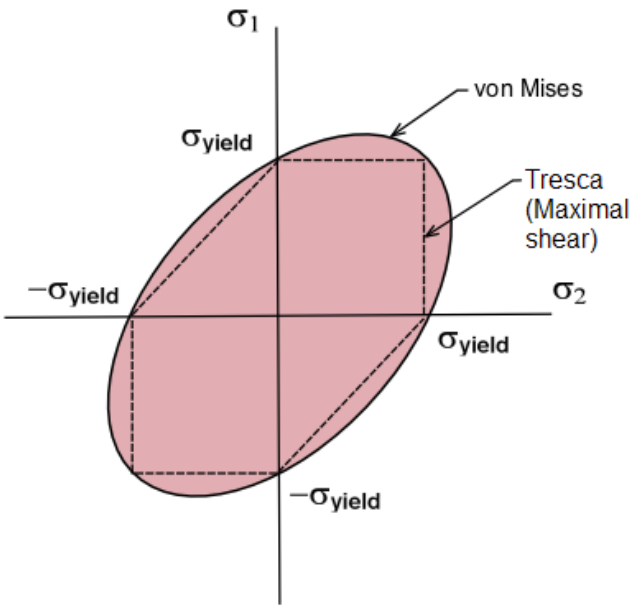

Fig. 7.2. Projection of the von Mises yield criterion (continuous) and Tresca (dashed) into the σ_1, σ_2 plane (pic source: Wikipedia).

7.5.2 Equivalent (effective) stress and strain

It is convenient to define an Equivalent tensile stress σ_e, which is used to predict yielding of materials under multiaxial loading conditions. Its value can be obtained from simple uniaxial tensile tests. Thus, the equivalent stress can be defined:

$$\sigma_e = \sqrt{3J_1} = \sqrt{\frac{2}{3} s_{ij} s_{ij}} \qquad \textbf{7.18}$$

where s_{ij} are the components of the stress deviator tensor σ^{dev} (Lemaitre and Chaboche, 1990). For an isotropic material it is unnecessary and thus inefficient to consider material evolution as a 3D problem. A single dimension parameter can be defined as the effective plastic strain rate $\dot{\varepsilon}_e^p$, with a direction corresponding to the

effective stress vector. For a Von-Mises material, the relationship between effective and the true nine plastic strain component is given by:

$$\dot{\varepsilon}_{ij}^{p} = \frac{3}{2} \cdot \frac{\sigma_{ij}^{dev}}{\sigma_{e}} \dot{\varepsilon}_{e}^{p} \qquad \textbf{7.19}$$

where σ_{ij}^{dev} is the deviatoric stress (Penny and Marriott, 1995).

7.6 FE simulation procedures

The FE simulation undertaken in this work is used to analyse the results from cold tensile tests conducted in the experimental investigation, in which a pre-necked bar is pulled in tension. Taking advantage of the geometric and loading axisymmetry of the tests, only one quarter of the test-piece is modelled and its dimensions are captured form real test-pieces. Two test-pieces were chosen for analysis.

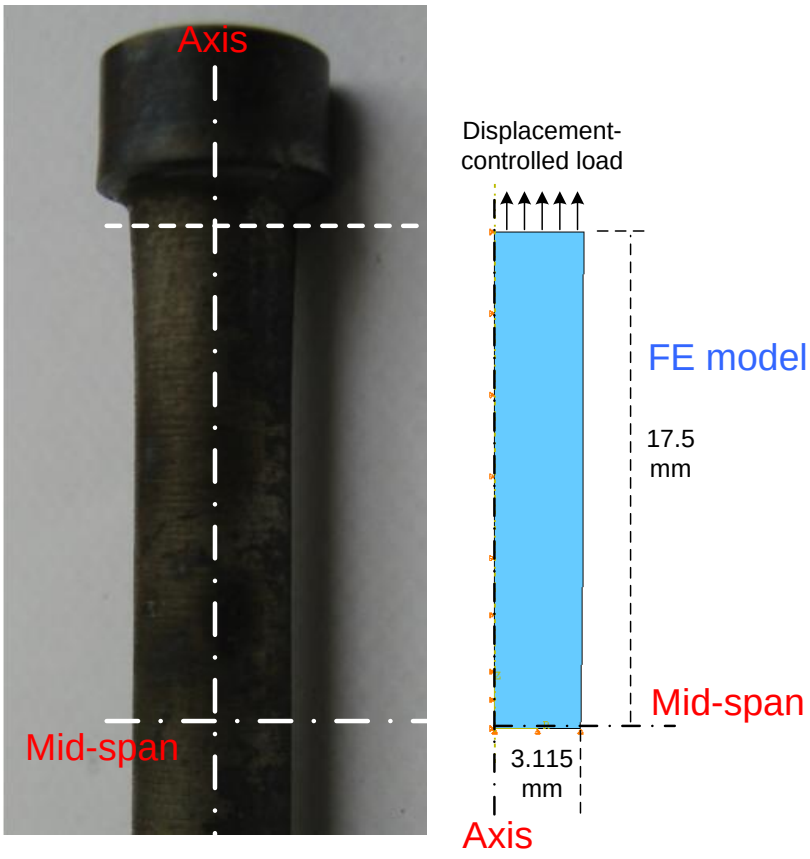

Fig. 7.3. Real test-piece (left) and FE geometrical model (right) with low necking feature (dimension in mm).

Fig. 7.3 shows the geometry of real test-piece and FE simulation model with insignificant necking, after first step deformation strain 0.2. The left-side edge and the bottom of the FE model are the axis and mid-span of test-piece, respectively, and constraints are applied to them as boundary conditions. To the top edge is applied a displacement-controlled load. The load is applied at a continuously changing velocity to ensure that the test-piece is pulled at a constant strain rate, as in the real tests. The mesh was generated automatically for the test-piece. In order to deal with the non-linear nature in material and geometry, a higher mesh density was applied in the region near the mid-span. Four-node quadrilateral axisymmetric elements are used in the

analysis. The same conditions were applied to the test-piece that necked significantly, at first step strain 1.0, as shown in Fig. 7.4.

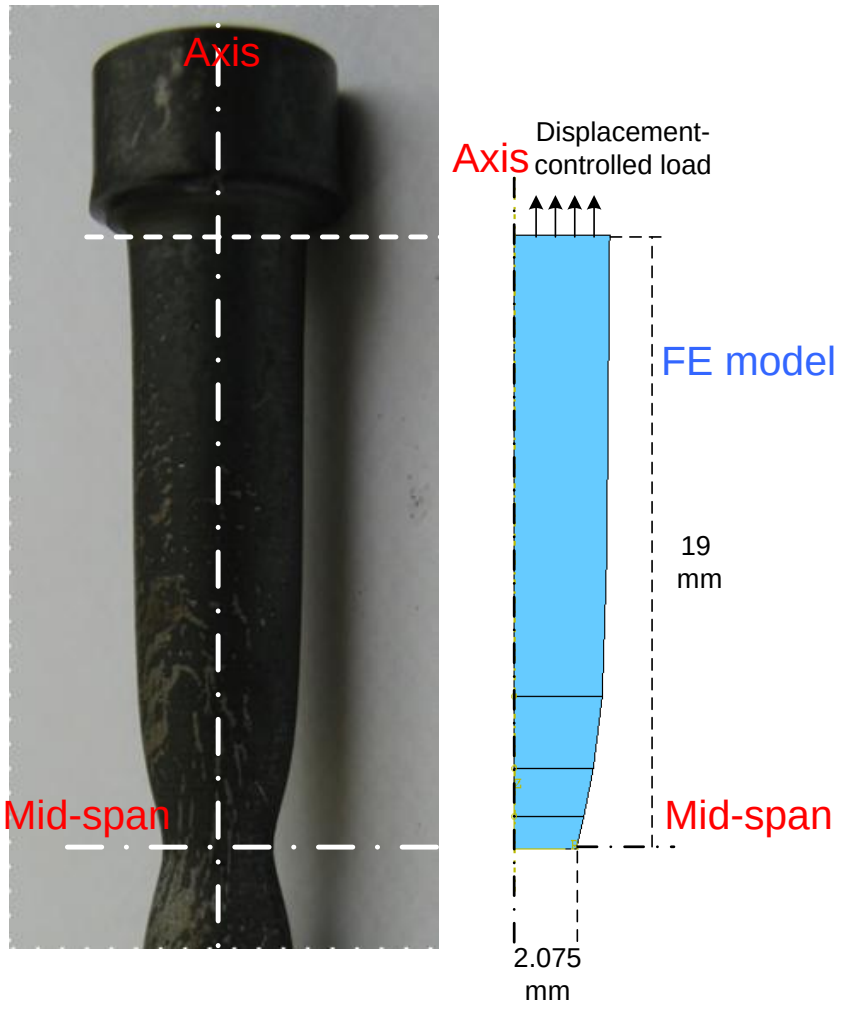

Fig. 7.4. Real test-piece (left) and FE geometrical model (right) with high necking feature (dimension in mm).

The material model was integrated with the finite element software ABAQUS through the user subroutine VUMAT. The evolution of each mechanism in the model is described by each element using an independent set of state variables that are uniquely associated with the element within the subroutine. There are several problems when considering damage, notably in controlling the late stage close to failure, where failing

regions have highly non-linear stress response and state variables. Also, highly damaged elements may create an abrupt step in stress between adjacent elements. Andrade Pires et al. (2004) have presented a detailed methodology for the implementation of damage models into FE. An explicit formulation is given, together with an elastic predictor/return-mapping scheme (Foster, 2007).

The user material subroutine VUMAT is called at each time increment during the analysis. The FE time increment is passed together with the strain increment tensor of each element. The preceding stress tensor and state variables from the previous step are also transferred. The basic routine framework is shown in Fig. 7.5. A loop was constructed within the routine to cycle through the updating of each element.

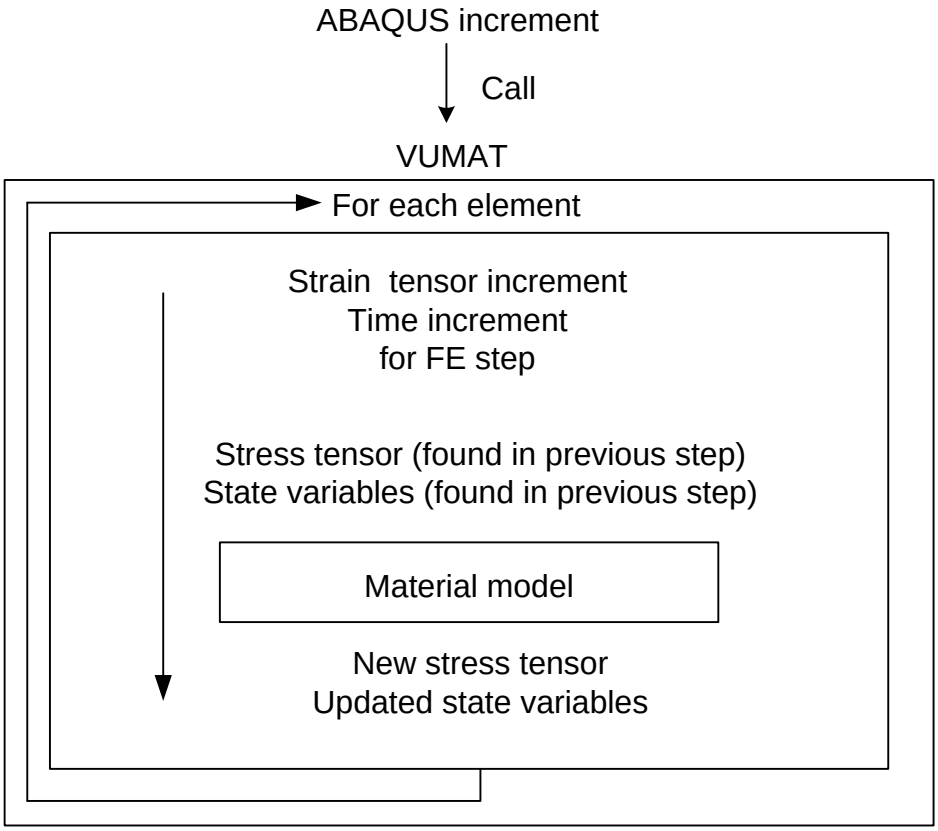

Fig. 7.5. The VUMAT call from ABAQUS showing information passed to & from the routine.

For a non-trivial material, it is first necessary to update the stress tensor to align with the new strain increment. The flow diagram (Foster, 2007), for the process used to do this is shown in Fig. 7.6. No material evolution occurs during this process, only the plastic strain and stress equations need to be iterated. In practice one or two iterations were often sufficient to align the tensor. For computational efficiency tolerance was defined when $\Delta\sigma_e/\sigma_e < 10^{-7}$ (selected arbitrarily) rather than the more correct way of assessing individual stress tensor components. This increases stability of the FE material model (Foster, 2007).

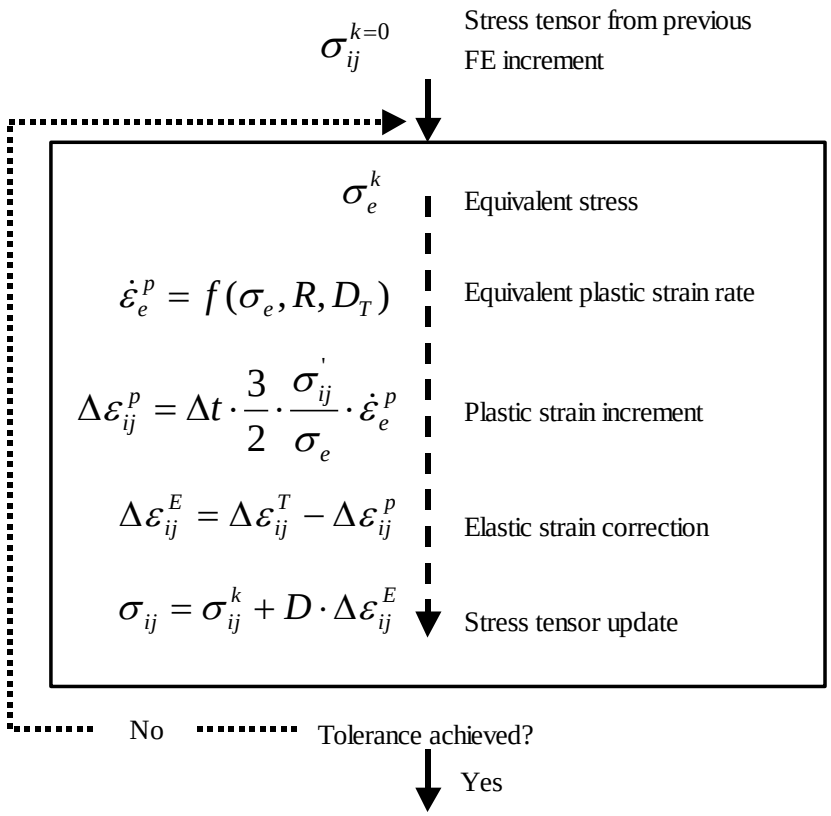

Fig. 7.6. Flow diagram of stress tensor update routine.

The material microstructure evolution rates then were calculated. A forward Euler method was used to integrate the material mechanism state variables, as with the large number of FE increments this proved more efficient than the complex backward Euler integration method. It was not necessary to update the material state variables at each increment due to the small time step between FE increments. Substantial computational updating of only the stress state on every increment saved time. State variables were updated over 3 increments. The calculation of optimum update points proved complicated to implement in an effective and efficient way. Failure of the material is defined as the accumulated total damage reaches 0.9.

7.7 Simulation results

7.7.1 FE validations

In Fig. 7.7(a), a failed real test-piece at first step strain of 0.2 (Fig. 7.3) is shown. The profile of the failed test-piece has been interpreted using the necking quantification method (discussed in Chapter 5). Positions have been chosen to accurately describe the failure profile, which the necking parameter N is calculated by:

$$N_x = \frac{d_{dia}{}^{x}}{d_{ref}} \qquad \textbf{7.20}$$

here $d_{dia}{}^{x}$ is the diameter at the positions of x mm away from the mid-span, and d_{ref} is the diameter of the reference position.

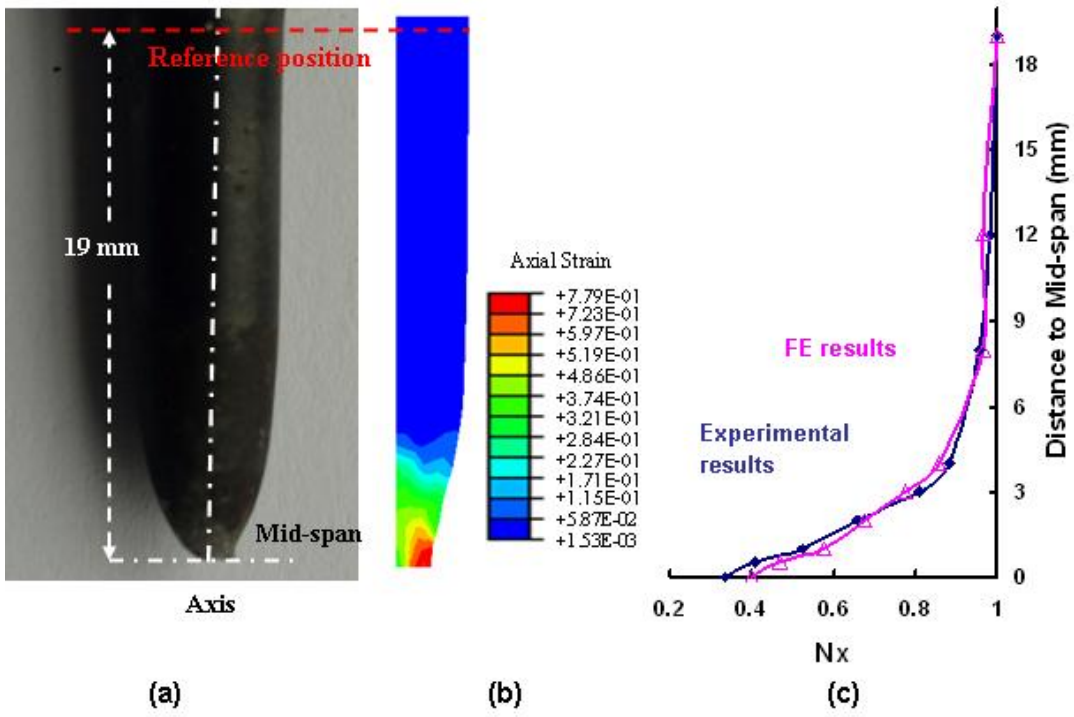

Fig. 7.7. (a) Failed real test-piece, (b) Simulated failed test-piece and (c) comparison of predicted (purple) and experimental (blue) necked profiles.

Making use of the updated constitutive model, using simulation, the failure profile shown in Fig. 7.7(b), was produced. A value of 7.2 was fitted for the damage stress triaxaility constant n_d , as a best fitting result obtained for n_d from 2 to 10. The predicted and experimental necked profiles are compared in Fig. 7.7(c). The real and simulated distribution profiles are similar in shape and value. The necking profile closed to mid-span is well predicted, which suggests the updated stress-state based model is able to simulate the material final failure process at macroscopic level. The experimental and simulated failure profiles for a test-piece with first step strain 1.0 (Fig. 7.4) are shown in Fig. 7.8. A value of 9.0 was chose for n_d , as a best fitting result achieved for n_d ranged from 3 to 15. Experimental necking is greater than simulated values, in regions between 0 to 2 mm from mid-span. The FE simulated and experimentally measured necking profiles above the 2 mm distance are in good agreement.

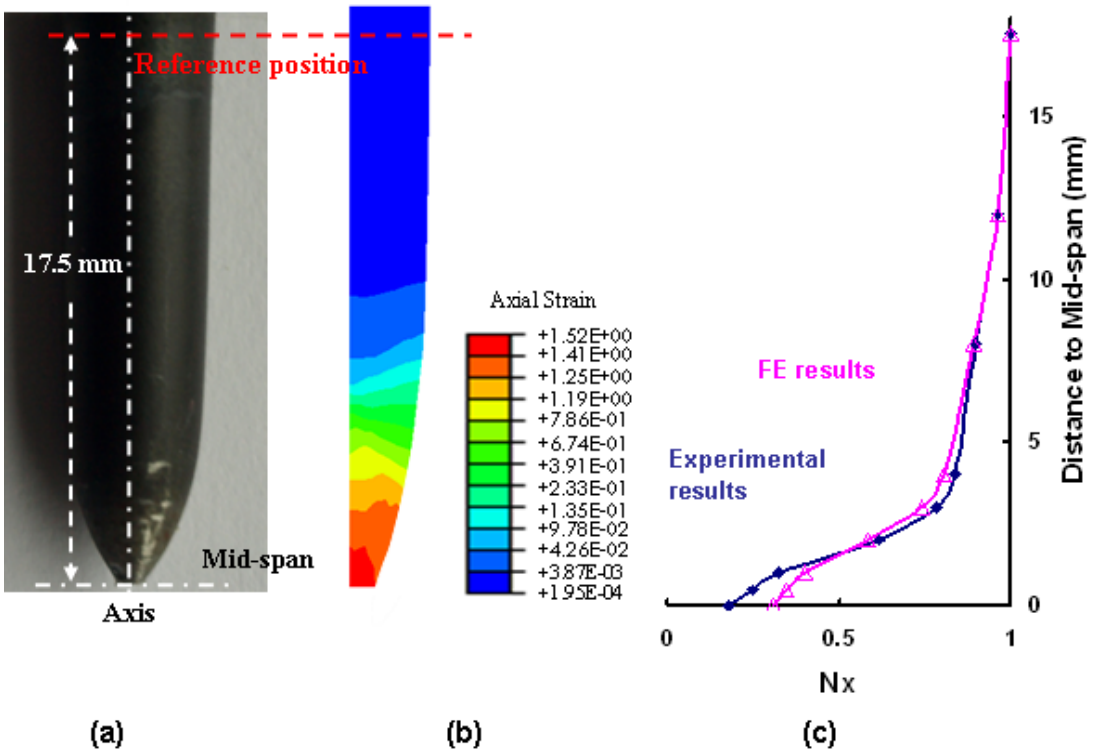

Fig. 7.8. (a) Failed real test-piece, (b) Simulated failed test-piece and (c) comparison of predicted (purple) and experimental (blue) necked profiles.

7.7.2 Damage evolution predictions

Fig. 7.9 shows the distribution and area of damage evolution predicted for highly necked test-piece (1st step strain 0.2). The 2nd step strains are 0.2, 0.5 and failure strain. The initial damage 0.02 was numerically calculated using the constitutive equation set (Chapter 6) for test-piece after first step strain 0.2 and subsequent annealing. The distribution of initial damage is assumed uniform throughout whole test-piece.

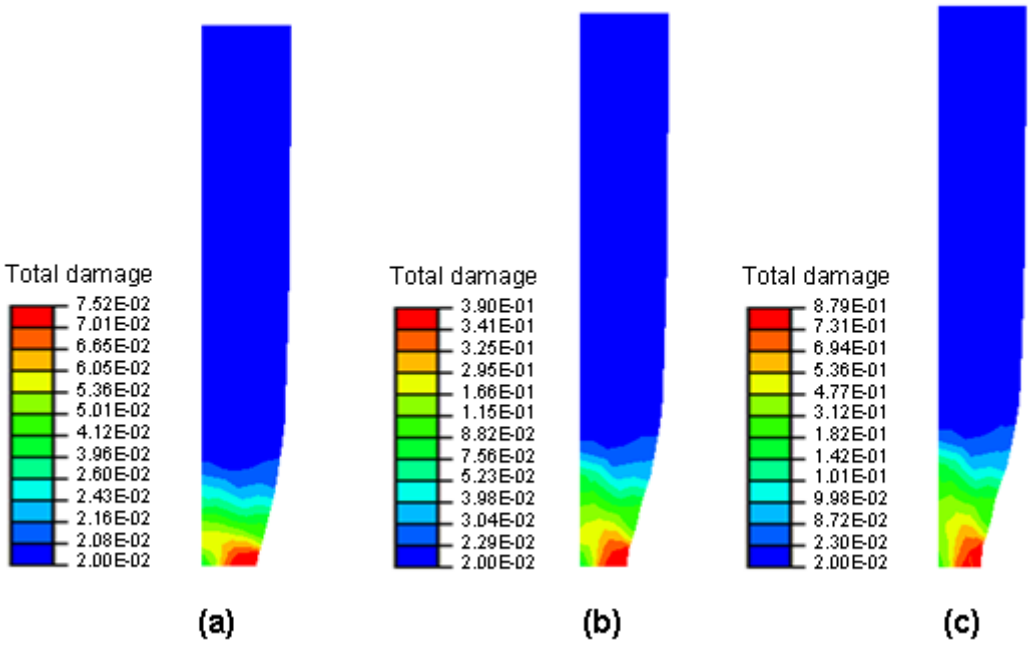

Fig. 7.9. Distribution of total damage evolution at 2nd step strain; (a) 0.2, (b) 0.5 and (c) failure strain 0.8.

As shown in Fig. 7.9(a), damage was distributed broadly across the necked area and the highest level of damage is build up around the centre edge of necked test-piece, where is the highest stress triaxiality, with strain 0.2. An increase in inclusion-related damage is confined to areas having a high tensile triaxiality during the process, shown in Fig. 7.9(b) and (c). This localised damage indicates that the failures of the sharp-necked steel were possibly driven by damage growth from the edge of test-pieces to the test-piece centre.

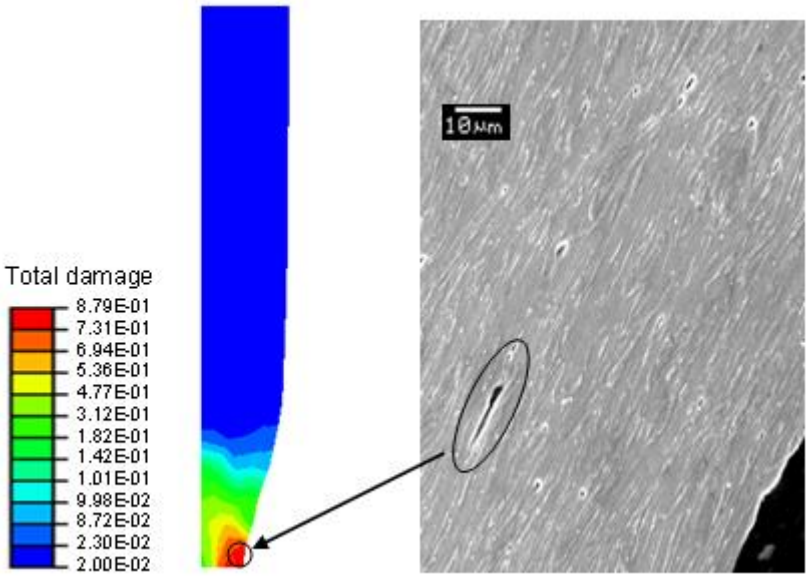

Fig. 7.10. Predicted and microscopically observed damage at failure stage.

An optical micrograph was used to examine damage in the real tensile test-pieces. An example is shown in Fig. 7.10. Large plasticity-induced damage can be observed near the edge of the test-piece that is in good agreement with simulation results. However, the amount of simulated damage is greater than experimentally observed. By looking at the FE model the reason for this becomes clear. In the real material, strain will localise at the point of coalescence once significant coalescence of cracks has arisen (i.e. a coalescence damage value approaching unity). Thus the matrix material in these locations will undergo significantly reduced plastic straining. This is not the case in the FE interpretation, whereby damage can continue to increase till reach the chosen failure value 0.9.

7.8 Summary

Suitable stress state equations have been derived to model the evolution of inclusion-related damage features. The constitutive model developed here is capable of predicting

the onset and extent of damage under various stress states. Damage predictions lie within expected error due to modelling assumptions, material consistency, experiment variations and depth of mechanism modelling. However there are some notable differences between the modelled deformed test-pieces and real test-pieces, in strength at failure.

CHAPTER 8

Damage evolution and mesoscopic FE simulation for dual phase steel

8.1 Introduction

Experimental work undertaken to find the damage characteristics of dual phase (Ferrite-Pearlite) linepipe steel, in simple tension, is described in this chapter. In the first section a short review of previous work on damage evolution in dual phase steels is made and the material studied in this thesis are detailed. Following this, a test programme and microstructural analysis before and after deformation, used to identify damage nucleation, growth and coalescence mechanisms, are described. Based on the microstructural evolution, the process of damage nucleation is modelled and simulated using meso-scale finite elements. Previous work on meso-scale FE models is reviewed. A description of the grain mapping and digitisation process used to generate FE mesostructures is given and the assumptions used to generate the model are discussed. FE results are compared with deformed tensile microstructures, to assess the validity of the model.

8.2 Review: Damage evolution in dual phase steels

Ferrite-Pearlite steels have been studied since the 18^{th} Century and have been widely used in many applications. The advantages of dual phase steels were described by Rashid (1976), who has demonstrated their great strength, compared with commercial single phase steels which have inferior ductility and formability. Classical products made from dual phase steels range from the heavily drawn fully pearlite cords for

bridge suspensions and reinforcements of automotive tyres to the low carbon sheets for various applications. For these applications, dual phase steels are cost effective.

There is an established relationship between second phase particles and mechanisms of ductile fracture, in dual phase steels. The fracture process in ductile metals is characterized microscopically by the nucleation and growth of voids that coalesce to produce the macroscopic fracture surface (Cuddy and Bassim, 1990). Since this process is due to the preceding localization of plastic deformation at microstructural heterogeneities, the importance of inhomogeneous arrangements of dislocations in the fracture process is unequivocal. A number of criteria have been proposed by several investigators (Goods and Brown, 1979; Argon et al., 1975; Fisher and Gurland, 1981; Gurland and Plateau, 1963) to describe the initiation and growth of voids at the particle-matrix interface. Wilsdorf (1983) has pointed out that the presence of particles is not a prerequisite for void nucleation. In metals with a low particle content, for example, void nucleation has been observed at grain boundaries and grain boundary triple points (Greenwood et al., 1954).

A detailed investigation into the micro damage mechanisms of a dual phase steel has been made by Cuddy and Bassim (1990). The work showed, the fracture surface topography in regions containing pearlite to be characterized by microcracks running normal to the pearlite colonies as illustrated in Fig. 8.1(a). At the higher magnifications shown in Figs. 8.1(b) and 8.1(c), shallow microvoids of size less than 0.5 μm, are visible in the interlamellar regions between cementile platelets, which appear as bright, parallel ridges in the micrographs. These results present a picture of the ductile fracture

process in 4340 steel. Microvoids, nucleated at cementite platelets in pearlite owing to the applied tensile stress and localized shear in the adjacent ferrite, propagate through the colonies and encounter softer ferrite grains. Crack propagation through the ferrite grains proceeds by void initiation and coalescence at the dislocation cell walls, leading to ductile fracture of the material.

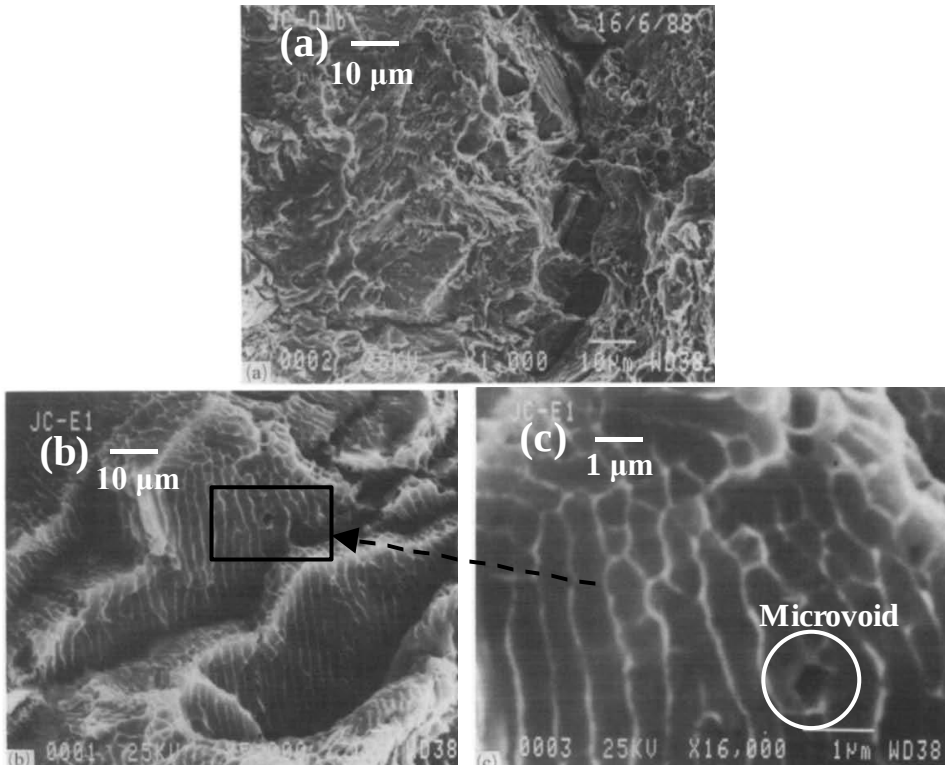

Fig. 8.1. Fracture surface of the pearlite showing (a) evidence of cleavage and microcracks and (b), (c) evidence of microvoids in interlammellar ferrite. (Cuddy and Bassim, 1990)

Previous studies have examined the mechanical behaviour of ferrite and pearlite, including microstructural examination of the steel after deformation. The literature suggests micro void initiation and propagation inside the grains plays a significant role in damage formation. This has also been observed in ductile cast irons (Iacoviello et al., 2007). However, there is less detailed work on the interaction mechanisms between pearlite and ferrite matrix material due to cold forming. To compensate for this, a

detailed investigation was conducted as part of this research, with further focus on damage nucleation features on the grain boundaries between pearlite and ferrite. For the purpose of modelling, the tensile mechanical flow stress response of material was also obtained.

8.3 Uniaxial tension test and microstructure analyses

8.3.1 Steels as received

The experimental material, STC-D, is a commercial dual phase plate steel containing 7% pearlite, used for large diameter linepipes and supplied by Corus R, D & T Swinden Technology Centre. The plate was produced through casting and hot rolling. Its chemical composition is listed in Table 8.1. The carbon content of this dual phase steel is higher than that of the steel STC-C, described in previous chapters and the sulphur content is about three times lower.

Plate code	Cast	C	Si	Mn	P	S	Al	Cr
STC-C	929521	0.034	0.34	1.56	0.005	0.0012	0.037	0.17
STC-D	16505	0.074	0.275	1.50	0.011	0.0004	0.036	0.048
Plate code	Mo	Ni	Cu	Nb	Ti	V	N	Pcm
STC-C	0.007	0.012	0.015	0.044	0.013	0.004	0.0042	0.135
STC-D	0.011	0.031	0.029	0.039	0.011	0.002	0.0039	0.164

Table 8.1. Chemical compositions of STC-C and STC-D steels.

The original microstructure of the steel is shown in Fig. 8.2. The second phase (pearlite) is dark grey and lies between ferrite grains. Fig. 8.2(a) shows the grain distribution in the longitudinal direction, which is the rolling direction. The pearlite is longer and more unidirectional compared to its shape and orientation in transverse direction (Fig. 8.2(b)).

The inclusions of manganese sulphide are not easily seen, due to the low content of sulfur in the steel.

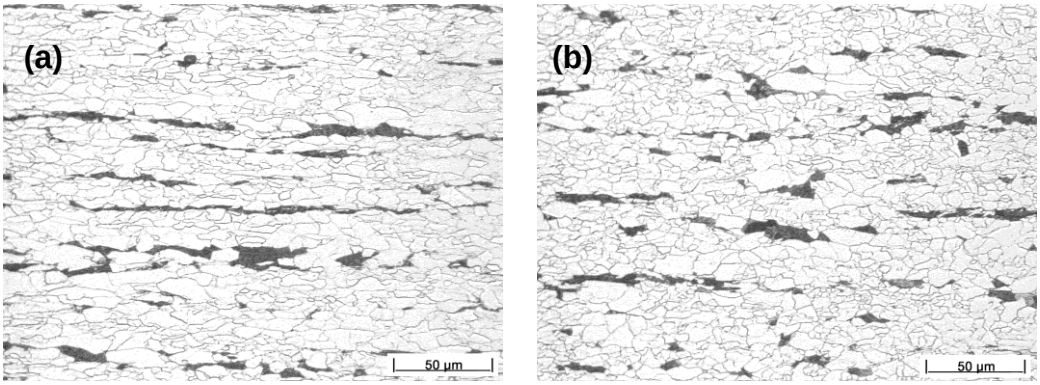

Rolling direction **Transverse direction**

Fig. 8.2. Optical Microstructures for Plates STC-D.

8.3.2 Uniaxial tension tests

A Zwick material test machine was used for the cold tensile tests, as described in previous chapters. Test-pieces were machined from the STC-D steel in the transverse direction. The test-pieces geometry was identical to that used for the interrupted tensile tests described in Chapter 4. The tests were carried out at room temperature (20ºC) at a strain rate of $0.008s^{-1}$. Strain was measured by diameter change using a C-gauge, and all strains referred to in this paper are true strains. To ensure the accuracy of strain measurement, the location of the C-gauge was periodically adjusted to ensure diametrical strain readings were taken at the visible neck location at all times. Total 6 tensile tests were carried out for dual phase steel and all test-pieces were sectioned to observe the damage features, which showed in next section.

8.3.3 Optical & SEM analysis of deformed samples

Typical necking observed at the point of failure is shown in Fig. 8.3(a). This is concurrent with the test-piece fracture surface consisting of the cup and cone features associated with high tensile hydrostatic stresses at the failure centre (Fig. 8.3(b)).

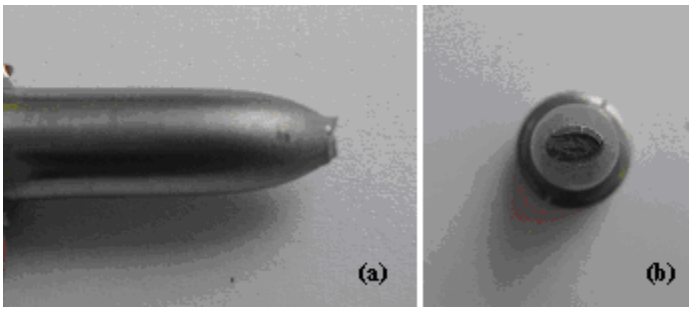

Fig. 8.3. Typical fractured test-piece.

The failure samples were sectioned longitudinally (Fig. 8.4(a)) to expose damaged regions. Samples were hot mounted in conducting Bakelite, ground and polished with diamond paste to 1μm. Aluminum oxide finishing polish was then used to remove remaining scratches. The damage evolution, which controls the ductile cracking, was observed in detail, with focus placed on void nucleation. The etched microstructures, examples of which are given in Fig. 8.4(b) and (c), show different levels of microstructure observed by SEM in the longitudinal direction in the middle of the specimen. The damage features are similar to those observed by Ohata and Toyoda (2004), with void nucleation at grain boundaries and grain boundary triple points.

As show in Fig. 8.4(b), numerous micro-voids measuring approximately 1 μm were found to nucleate in the hard pearlite phase near the Ferrite–Pearlite interface after 0.8 tensile plastic straining. This nucleation behaviour of micro-voids could be due to the highly condensed pile-up of dislocations near the interface of microstructures with

mismatch in strength. Moreover, almost no voids of any size were observed in the undeformed test-pieces, showing that the damage arose virtually entirely due to cold plastic deformation in the tensile tests. The elongated voids were observed along the grain boundaries after 1.3 tensile plastic strain just before 1.56 ductile cracking strains (Fig. 8.4(c)). This shows that growth of larger voids play an important role in damage mechanism during this stage, and is the accepted mechanism of ductile cracking.

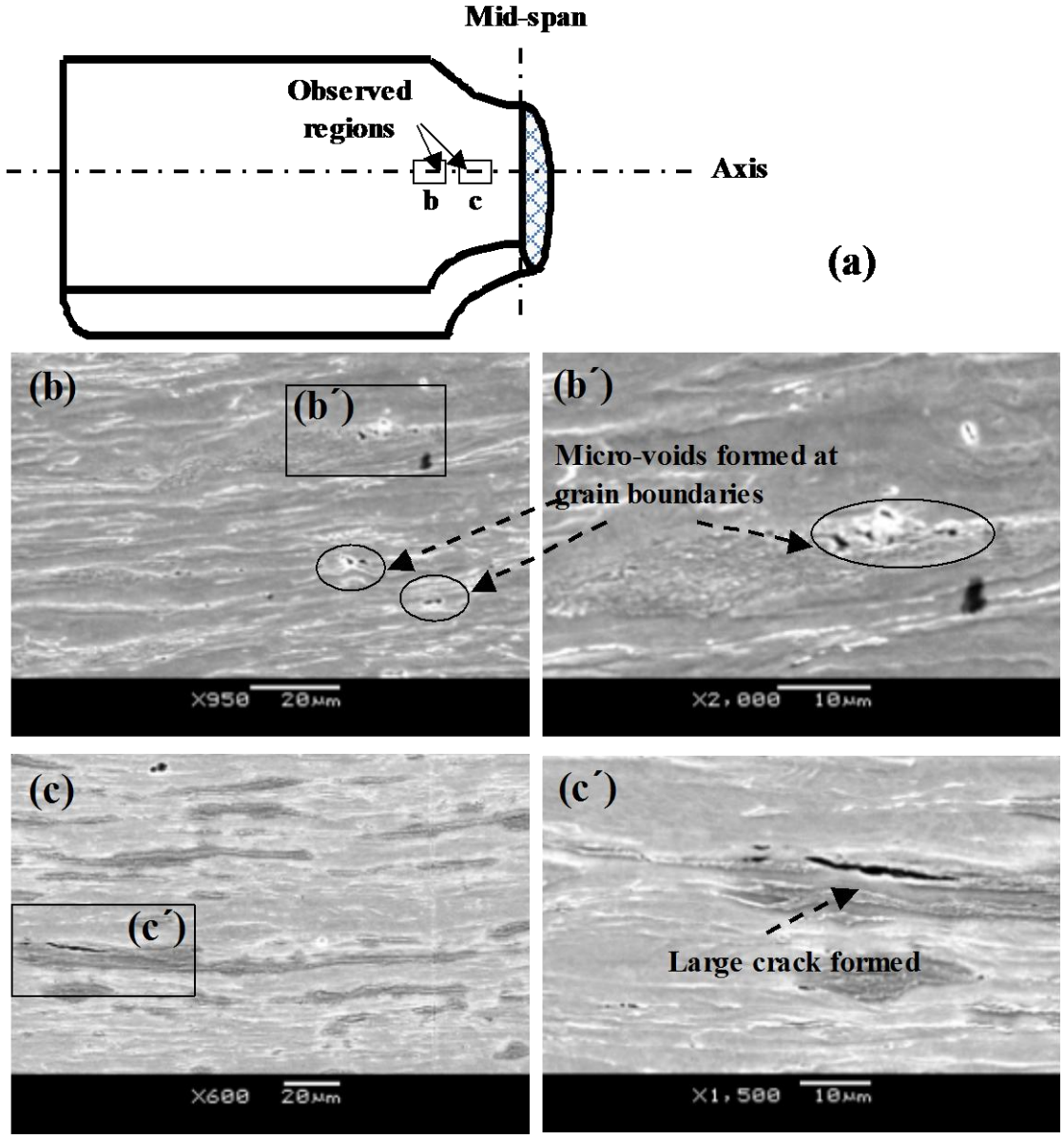

Fig. 8.4. Observation of material damage with respect to ductile cracking in the middle of specimen for Ferrite–Pearlite two-phase steel used.

8.4 Review of mesoscopic FE simulation

As the name suggests, the mesoscopic model approximates material to a form that lies between large-scale continuum and true, fully detailed microstructural modelling. Only selected features of the material microstructure are reproduced in the finite element

model, vastly simplifying the simulation. Mesoscopic models may be used to study matrix mechanical behaviour, stress localisation or a particular mode of failure.

Tomota et al. (1976) proposed a continuum model for predicting tensile behavior of two-ductile-phase alloys. This model can predict stress–strain curves of dual-phase materials from the tensile properties of each constituent phase, and it can be applied to three-phase materials (Rudiono and Tomota, 1997). Huper et al. (1999) examined the hardening behavior of two-phase high strength steels by using Tomota's continuum model. Although this continuum model successfully predicts the stress–strain behavior of the multi-phase material, it does not provide the local stress–strain state inside each phase. As this continuum model is based on Eshelby's inclusion theory (1957) and mean field concept by Mori and Tanaka (1973), stress and strain distributions are averaged inside each phase; while the actual stress–strain distribution in each phase of the material can display a substantial degree of localization. Furthermore, Tomota's model has been mainly applied for materials containing spherical inclusions or second-phase particles, while many high strength structural steels are produced by controlled rolling processes, resulting in a microstructure elongated along the rolling direction, for which large effects of the shape and distribution of the second-phase on the mechanical properties can be expected. In order to determine the local stress–strain state and the effect of the morphology of the second-phase particles, preliminary investigations have been conducted by finite element analysis (Tomota et al., 1982; Shikanai et al., 1992). However, these two-dimensional FE analyses gave only qualitative information on the local stress–strain state, or the macroscopic behaviour of multiphase materials because of the difficulty in constructing an adequate model which captures the real mechanical

behavior of the microstructure, especially the interactions of heterogeneous representative volume elements.

Following its introduction by Tvergaard (1982), the stacked hexagonal- array axisymmetric cell model (SHA model) has been commonly used for FE-analysis of porous materials and two-phase materials with spheroidal inhomogeneities. The distribution of voids or second-phase particles is idealized by an array of hexagonal cylinders, each containing a spherical void or second-phase particle. This model is quite accurate if the volume fraction of voids or second-phase particles is small, or when there is a relatively small difference in deformation resistance between the matrix and particle phases. However, it does not provide an adequate prediction for the macroscopic material behaviour when the interaction between adjacent voids or second-phase particles is not negligible. Recently, Socrate and Boyce (2000) proposed a simplified axisymmetric finite element unit cell model to investigate macroscopic and microscopic stress–strain behaviour of toughened polycarbonate. This axisymmetric unit cell model (V-BCC model) is based on a Voronoi tessellation of the BCC lattice, which better represents the spatial distribution of voids or second-phase particles, and can accommodate a local deformation mode consisting of shear localization of matrix materials between voids. Socrate and Boyce (2000) investigated porous materials, but this new micromechanical model also can be valuable to investigate many cases of dual phase materials.

8.5 Generating the mesoscopic model

Significant research has been carried out and it has been demonstrated that Voronoi tessellation can be used to generate polygon grain structures (Zhu et al., 2001; Okabe et al., 1992; Stoyan et al., 1987). The Voronoi tessellation divides a region into convex polygons, or cells that fills the space without overlap. Grain generation software, VGRAIN, has been developed based on two-dimensional Voronoi polygon modelling technique (Riesch-Oppermann, 1999; Weyer, 2002; Nakamachi et al., 2000). The software, VGRAIN (Cao et al., 2009), is written in Visual C++ and can generate the virtual microstructure of a material based on Voronoi polygon theory and the text file, that contains information of virtual microstructure in the figure, can be loaded into ABAQUS/CAE. The mesoscopic finite element models generated microstructure of the steel, using VGRAIN, automatically. With such a small sample area, it is impossible to assume results are truly representative of the steel. Acknowledging this, the work presented here aims only to provide a visual aid to the local stress distribution and the possible area of damage nucleation.

8.5.1 Material assumptions and mapping

The structure of the dual phase steel was assumed to be a continuum matrix (Ferrite) inter-dispersed with second phase (Pearlite) with different material properties. The second phase was modelled as being fully bonded to the matrix material, with fully bonding force across the grain boundaries at all times. Recognising this, the model has no significant merit for the visual demonstration of damage nucleation. The analyses were performed as plain strain, which significantly reduces the mesh complexity and thus computation time needed from a full three-dimensional analysis.

Plate	Pearlite Grain size	Ferrite Grain size	% Pearlite
STC-D	5.6 micron (13.3 d-½)	9.7 micron	7

Table 8.2. Microstructural parameters for STC-D steel.

Fig. 8.5 shows the VGRAIN mapping method used to create the FE element mesh. Configurations of these meshes were defined in accordance with the actual microstructure of the ferrite-pearlite steels, to describe shape and distribution of the pearlite phase. Firstly, the microstructure of a typical area was selected from images of the Ferrite-Pearlite steel presented in Fig. 8.5(a), which has been used to guide generating the initial microstructure of the simulation. Table 8.2 has details of the average size of both grains and the ratio of the second phase and then these data were input into the VGRAIN mapping software. The generated microstructures of dual phase steels using VGRAIN were output and the one with the phase distribution most similar to that of the real microstructure was chosen (Fig. 8.5(b)). The resulting mesoscopic simplification was finely meshed with standard plain strain two-dimensional elements (Fig. 8.5(c)).

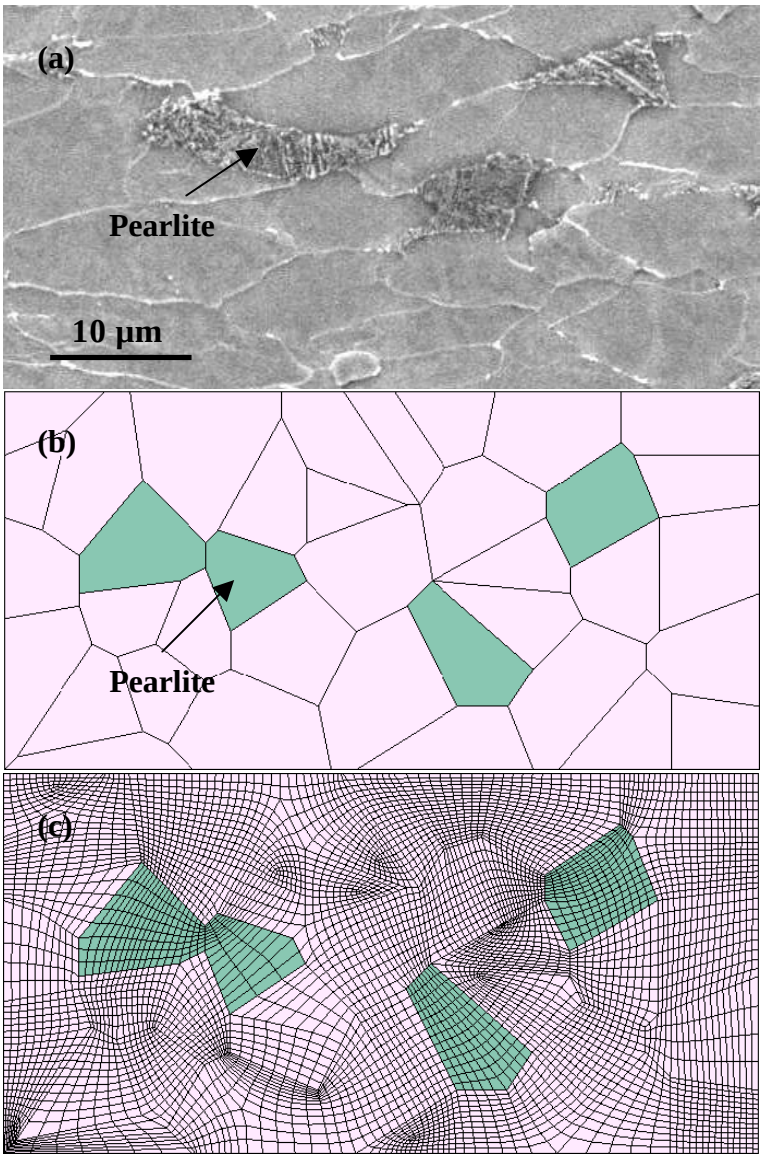

Fig. 8.5. (a) Micrograph area selection, (b) Microstructure mapping using VGRAIN and (c) The FE mesh for the mapped region.

8.5.2 Material definition

The stress strain relationships were defined as material data characterizing the ferrite matrix and pearlite phase. Ishikawa et al. (2000) reported the stress train behaviour of the single-phase, ferrite and pearlite, respectively, during uniaxial tensile tests. The two phases are described by the von Mises yield criterion and the associated flow rule with

isotropic hardening. The hardening behaviour of the single-phase ferrite and pearlite are presented in Fig. 8.6. Damage softening has not been considered from the macro response of the single phase, as the interaction between the two phases is the main concern of damage evolution. The hardening of ferrite and pearlite were assumed constant throughout deformation. At room temperature ferrite phases are far softer than the pearlite phase, as shown in Fig. 8.6.

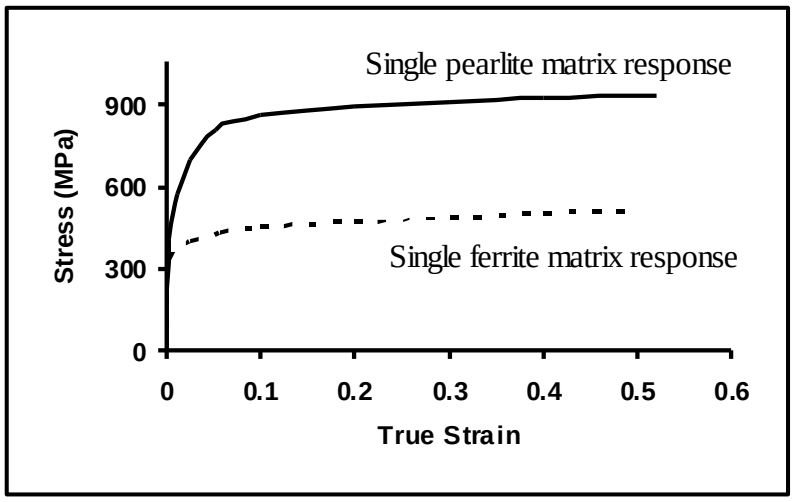

Fig. 8.6. Influence of ferrite and pearlite phase on tensile test results. (Source: Ishikawa et al. 2000).

To summary, in this initial simulation the following assumptions were made:

- The material obeyed the von-Mises yield criteria.
- A uniform test temperature was assumed.
- Surface scale was not modelled.
- Damage evolution was turned off to allow the simulation of material past its tensile failure strain.

8.5.3 Simulation Procedures

To create an accurate representation of the macro tensile stress state, the boundary conditions are applied and shown in Fig. 8.7.

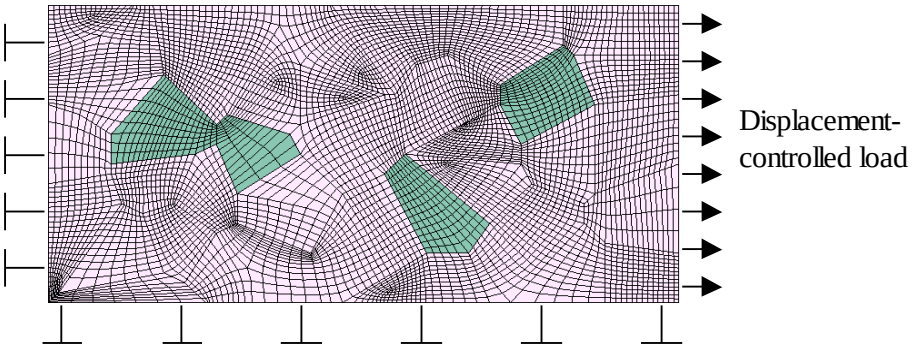

Fig. 8.7. A schematic representation of FE model loading condition.

8.6 Results

From the finite element simulation, stresses and strains at a micro scale within the material can be studied. Fig. 8.8 shows the results of simulated progression of stress, localised on pearlite phases, during tension. The plain strain approximation visually demonstrates the interaction of ferrite and pearlite, the development of stress networks, and eventually identifies a weak area through which void nucleation might take place. The simplification to plain strain leads to an exaggeration of damage, as stress is redistributed within the matrix in two dimensions only. It is apparent that the harder pearlite is subjected to the largest stresses due to the strength mismatch of the two phases.

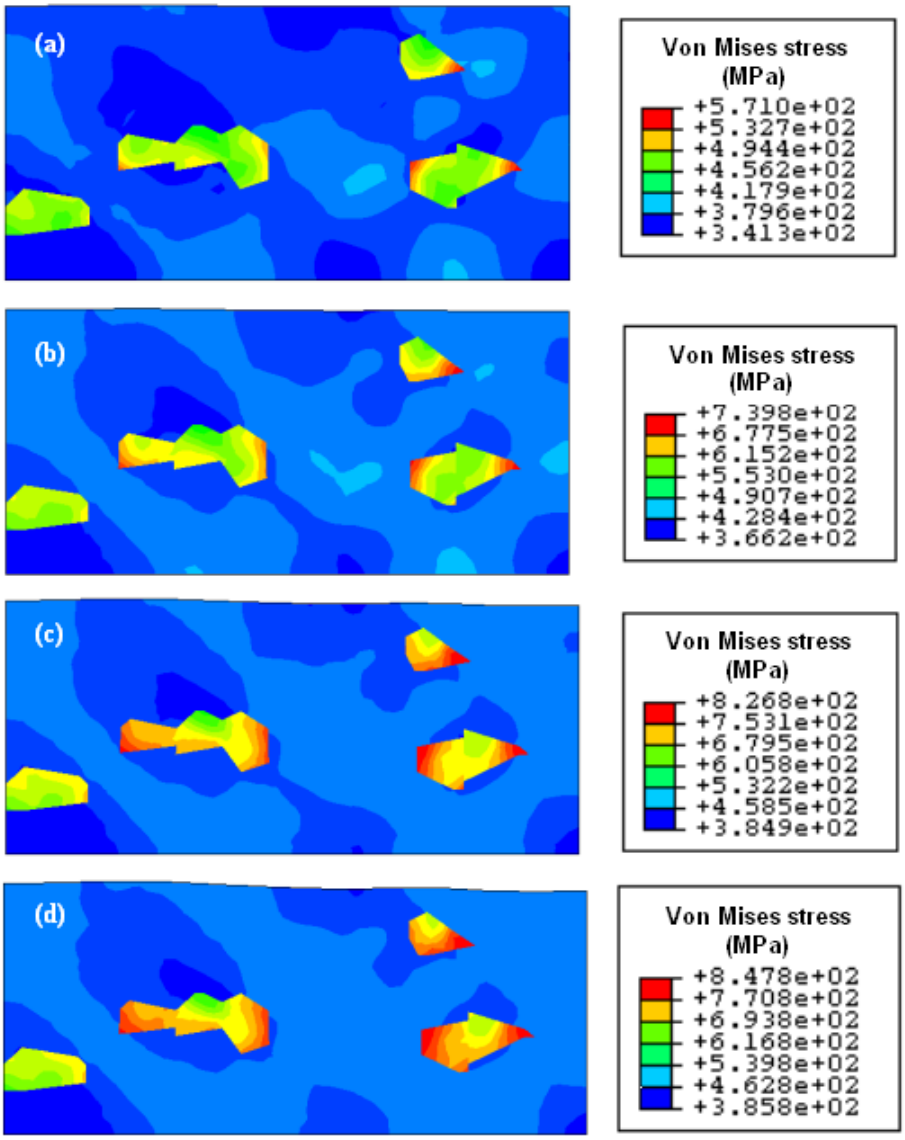

Fig. 8.8. Progression of mesoscopic flow stress at pearlite/ferrite interfaces with strain equal to (a) 0.01, (b) 0.03, (c) 0.06 and (d) 0.1.

The significance of grain boundary related damage interaction is clear from the simulation results. Initial straining of the material (Fig. 8.8(a)) results in the formation of stress concentrations in the pearlite close to the boundary with the ferrite, particularly at sharp points. Full atomic bonding forces are assumed to prevent the separation of the two phases, and the stress will be high at the grain boundaries, due to the inhomogeneous arrangements of mechanical properties for the two phases. Damage

nucleation could take place in these areas easier, due to the stress concentration. As deformation continues, the distribution of stress within the simulated area becomes more inhomogeneous, the stress within the pearlite phase close to the interface with ferrite is higher than elsewhere. Fig. 8.8(b), (c) and (d) show the stresses increase in value along the ferrite/pearlite interface, leading to further possibilities of damage growth and crack coalescence. This will reduce the real area available to support the imposed load on the steel, increasing overall stresses even more until failure of a whole section occurs.

Comparing the simulated results to the experimental microscopic graph of deformed microstructures, as shown in Fig. 8.9, good agreement of the damage initiation area is obtained. Recent work by Dai et al. (2002) also shows microcrack initiation sites identified at the ferrite-pearlite interfaces. Micro damage may nucleate once the stress value reaches a certain level, as is shown in the circled areas of simulated result in Fig. 8.9.

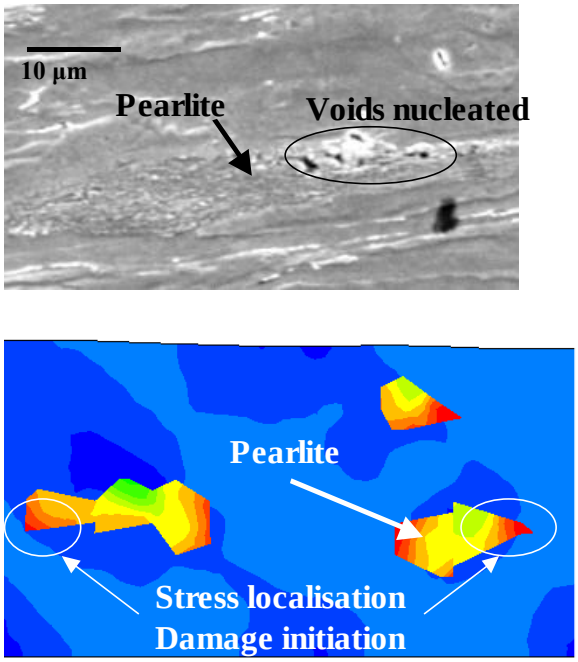

Fig. 8.9. Microscopically observed and predicted damage nucleation area.

8.7 Summary

The concept of a damage mechanism for ductile cracking was derived from the experimental observation that ductile cracking is controlled mostly by the nucleation of micro-voids near the ferrite-pearlite interface in the steel. The used mesoscopic model was capable of being used to simulate the basic damage initiation features during tension tests.

CHAPTER 9

Conclusions and suggestions for future research

As experimental and theoretical study on deformation behaviour and its associated damage evolution during cold forming and annealing is presented in this thesis. The key findings are summarised into four categories and future research is suggested.

9.1 Conclusions

9.1.1 Active mechanisms

From the results of uniaxial tensile tests together with microstructure examinations, the phenomenon of plasticity-induced damage during cold deformation has been revealed. Growth and coalescence of damage features are initially associated with inclusions for single phase linepipe steel during cold deformation. When the material is deformed under tensile hydrostatic conditions damage features grow as oval voids around inclusions. For plastic deformation, in which inclusion damage has arisen and a tensile principal stress is present, coalescence cracks will form linking inclusion related damage features, leading to failure.

From the results of interrupted tensile tests, it has been observed that for lightly deformed metal, annealing leads to healing, due to diffusion bonding and recrystallisation and enables a significant improvement in mechanical properties to be achieved. The improvement achievable in heavily damaged material is slight as diffusion bonding across large voids is not possible.

During cold deformation and annealing operations, most metals experience both dynamic changes and static changes in microstructure and their flow behaviour is influenced by these changes. Strain hardening due to accumulation of dislocations and softening due to recovery and recrystallisation, dominate material behaviour during cold working and heat treatment, respectively.

9.1.2 Constitutive modelling

Experimental stress-strain relationships for a range of interrupted conditions have been obtained and were used in the determination and validation of the viscoplastic-damage constitutive equations.

A novel set of unified mechanism-based viscoplastic-damage constitutive equations has been developed. The equation set novelty takes into account the effects of annealing time and healing of damage and characterises the mechanical and microstructural behaviour. The equation set is able to model not only plastic flow behaviour but also the evolution of flow dislocation density, isotropic hardening, static recovery and recrystallisation, grain size evolution, plasticity-induced damage and the evolutions of microstructure. It enables dynamic/static microstructural changes to be described in a continuum.

9.1.3 Finite element analysis

Novel interrupted tensile tests with necked test-pieces together with numerical analysis were used to rationalise the effect of stress state on damage evolution during cold forming. Implementation of the developed stress-state dependent equation set into the

industrial-standard finite-element solver ABAQUS through a user-defined subroutine has resulted in an integrated model for damage evolution for different stress-states. Microstructural evolution during cold deformation can be predicted assuming the metal is a continuum, for the process. The experimental and simulated results are in good agreement. This demonstrates the accurate and detailed modelling capability of developed set of unified mechanisms-based stress-state dependent damage constitutive model.

9.1.4 Mesoscopic FE simulation

The understanding of damage development in a dual phase linepipe steels has been advanced and much of the work can be transferred to other related metals. From an investigation of microstructure, contrast to single phase steel, damage was seen to develop around interfaces between ferrite and pearlite for dual phase linepipe steel during cold deformation. Novel mesoscopic finite element simulations, generated from true material microstructures, were developed to visualise the basic damage initiation features. The damage evolution of the dual phase steel in cold forming can be rationalised with the use of the developed mesoscopic method.

9.2 Recommendations for future research

This research area has many new challenges, which, if addressed, will add to the understanding and modelling of cold forming processes and heat treatments. Three important topics to be dealt with are:

9.2.1 Damage healing mechanisms

Although healing of damage after cold deformation has been revealed, the mechanisms of healing process still remains uncertain. The micro-mechanism of diffusion should be investigated to determine the limiting size of void that can be healed without extra stress applied. Further experimental and theoretical study need to be carried out for the further development of damage equations.

9.2.2 Inclusion effects

It is experimentally evident that inclusions provide a nucleus for plasticity-induced damage. They have been assumed to be uniformly distributed spheres of the same size and have identical influence on damage accumulation. In order to produce a more realistic model of the effect of inclusions on damage evolution, the effects of size, geometry and disposition, should be determined and mathematically represented in the equation set.

9.2.3 Mesoscopic techniques

In cold forming, stress concentration due to crystal orientations and slip systems at different phase grain boundaries is worth studying in mesoscopic level, which contributes to damage initiation. To simulate damage evolution more revealingly, a more realistic description of the bonding between ferrite and Pearlite, considering their respective properties, needs to be produced. Further development of mesoscopic technique into three-dimensions with crystal plasticity theories would be a valuable tool for analysing the damage mechanism in dual phase steels.

REFERENCES

Abu Al-Rub, R. K. and Voyiadjis, G. Z. (2003). On the coupling of anisotropic damage and plasticity models for ductile material. International J. Solids Stru., 40, 2611-2643.

Andrade Pires, F. M., De Souza Neto, E. A. and Owen, D. R. J. (2004). On the finite element prediction of damage growth and fracture initiation in finitely deforming ductile materials. Computer Methods in Applied Mechanics and Engineering, 193, 5223-5256.

Argon, A. S. and Safoglum, J. R. (1975). Cavity formation from inclusions in ductile fracture. Metall. Trans. A 6, 825-837.

Ashby, M. F. and Dyson, B. F. (1984). Creep damage mechanics and micro-mechanisms. National Physical Laboratory.

Barnett, M. R., Jonas J. J. and Hodgson, P. D. (1994). Grain size after warm working and recrystallisation of a low carbon steel, Proceedings of 36th Mechanical Working and Steel Processing Conference, Baltimore, p. 385.

Beyerlein, I. J. and Tomé, C.N. (2008). A dislocation-based constitutive law for pure Zr including temperature effects, Int. J. Plasticity 24, 867-895.

Bocher, L., Delobelle, P., Robinet, P. and Feaugas, X. (2001). Mechanical and microstructural investigations of an austenitic stainless steel under non-proportional loadings in tension–torsion internal and external pressure. Int. J. Plasticity 17, 1491–1530.

Bogatov, A. A. (2003). The mechanics of the ductile damage under the metal forming. ESAFORM 2003.

Bonora, N. (1997). A nonlinear CDM model for ductile failure, Engineering Fracture Mechanics, 58, 11-28.

Bordeuil, C., Salle, E., Boyer, J. C. (2003). An orthotropic specific damage model with inclusion consideration. J. Mater. Processing Technology, 143-144, 337-341.

Bridgman, P. W. (1946). The effect of hydrostatic pressure on plastic flow under shearing stress. Journal of Applied Physics, 17, 692-698.

Bridgman, P. W. (1946). The effect of hydrostatic pressure on the fracture of brittle substances. Journal of Applied Physics, 18, 246-258.

Bridgman, P. W. (1952). Studies of large plastic flow and fracture. New York, McGraw Hill.

Brinckmann, S., Siegmund, T. and Huang, Y. (2006). A dislocation density based strain gradient model. Int. J. Plasticity, 22, 1784–1797.

Brunig, M. (2002). Numerical analysis and elastic-plastic deformation behaviour of anistropically damage solid. International Journal of Plasticity, 18, 1237-1270.

Brust, F. W. and Leis, B. N. (1992). A new model for characterizing primary creep damage. International Journal of Fracture, 54, 45-63.

Bucher A., Görke U. J. and Kreißig R. (2004). A material model for finite elasto-plastic deformations considering a substructure. Int. J. Plasticity 20, 619–642.

Cao J., Lin J. and Dean T. A. (2006). User's manual for OPT-CE: an optimizer for the determination of constitutive equations, Internal Report MFG2006-003, University of Birmingham, UK.

Cao J., Lin J. and Dean T. A. (2008). An implicit unitless error and step-size control method in integrating unified viscoplastic/creep ODE-type constitutive equations, Int J Numer Meth Eng, 73, 1094 – 1112.

Cao, J. and Lin, J. (2008). A study on formulation of objective functions for determining material models. Int J Mech Sci, 50, 193 – 204.

Cao, J., Zhuang, W., Wang, S. and Lin, J. (2009). Development of a VGRAIN system for CPFE analysis in micro-forming applications. The International Journal of Advanced Manufacturing Technology (In press).

Chaboche J. L. (1987). Continuum damage mechanics: present state and future trends, Nucl. Eng. Design 105, 19-33.

Cheong, B. H. (2002). Modelling of microstructural and damage evolution in superplastic forming. Manufacturing and Mechanical Engineering, University of Birmingham.

Cocks, A. C. F. and Ashby, M. F. (1980). Intergranular fracure during power-law creep under multiaxial stresses. Metal Scirnce, 14, 395-402.

Cocks, A. C. F. and Ashby, M. F. (1982). On creep fracture by void growth. Prog. Mat. Sci., 27, 189-203.

Considère, A. (1885). Ann. Ponts et Chaussées 9, 574–775.

Cuddy, J.K., Bassim, M.N. (1990). Ductile fracture mechanisms in AISI 4340 steel, Mater. Sci. Eng. A 125, 43-48.

Dai, P. Q., He, Z. R., Zheng, C. M., Mao, Z. Y. (2001). In-situ SEM observation on the fracture of austempered ductile iron, Mater. Sci. Eng. A 319-321, 531-534.

Dougherty, E. R., Lotufo, R. A. (2003), Hands-on Morphological Image Processing. SPIE PRESS, Vol. TT59.

Dunne, F.P.E. and Katramados, I. (1998). Micro-mechanical modelling of strain induced porosity under generally compressive stress states. International Journal of Plasticity, 14, 577-595

Dunne F. P. E., Nanneh M. M. and Zhou M. (1997). Anisothermal large deformation constitutive equations and their application to modelling titanium alloys in forging. Phil. Mag. A 75, 587-610.

Dyson, B. F., Verma, A. K. and Szkopiak, Z. C. (1981). The influence of stress state on creep resistance: experimentation and modelling. Acta. Met., 29, 1573-1580.

Estrin Y. (1996). Unified constitutive laws of plastic deformation, Academic Press, New York, p 69.

Estrin Y. (1998). Dislocation theory based constitutive modelling: foundations and applications, J. Materials Processing Technology 80-81, 33-39.

Estrin Y., Tóth L. S., Molinari A. and Bréchet Y. (1998). A dislocation-based model for all hardening stages in large strain deformation. Acta Mater. 46, 5509–5522.

Farrugia D. C. J. and Howe A. A. (1999). Alloy design: from composition to through process models. Materials Science and Technology 15, 15-21.

Foster A. D. (2007). Modelling damage evolution during the hot deformation of free machining steels. Manufacturing and Mechanical Engineering, University of Birmingham.

Foster A. D., Lin, J., Liu Y., Farrugia D. and Dean T. A. (2005). Constitutive modelling of damage accumulation during the hot deformation of free-cutting steels, Proceedings of the 8th Esaform conference I, 201-204.

Fisher, J. R., Gurland, J. (1981). Void nucleation in spheroidized carbon steels, part I: experimental and part II: model. Metal Science 15, 185–202.

Ghosh, A. K., Hamilton, C. H. (1979). Mechanical behaviour and hardening characteristics of a superplastic Ti–6Al–4V alloy. Metall. Trans. A **10a,** 699–706.

Goods, S. H., Brown, L. M. (1979). Overview No. 1: The nucleation of cavities by plastic deformation, Acta Metall. 27, 1-15.

Greenwood, J., Miller, D. R., Suiter, J. W. (1954). Intergranular cavitation in stressed metals. Acta Metall. 2, 250-258.

Griffith, A. (1920). The phenomena of rupture and flow in solids, Philosophical Transactions of the Royal Society of London. Series A, Containing Papers of a Mathematical or Physical Character, 221, 163–198.

Grong, Ø. And Shercliff, H. R. (2002). Microstructural modelling in metals processing. Progress in Materials Science, 47, 163-282.

Gurland, J. and Plateau, J. (1963). The mechanism of ductile rupture of metals containing inclusions, Trans ASM 56, 442–54.

Gurson L. (1979). Continuum theory of ductile rupture by void nucleation and growth: Part I - Yield criteria and flow rules for porous ductile media, J. Eng. Mater. Tech. 99, 2-15.

Han, J., Zhao, G. and Cao, Q. (1997). Study on internal crack recovery of 20MnMo steel, Sci. China (Ser. E), 27, 23–27.

Hesselbarth H. W. and Göbel I. R. (1991). Simulation of recrystallization by cellular automata. Acta Met Mat 39, 2135-2143.

Hoc T. and Forest S. (2001). Polycrystal modelling of IF-Ti steel under complex loading path. Int. J. Plasticity 17, 65-85.

Houtte, P. V., Li, S., Seefeldt, M. and Delannay, L. (2005). Deformation texture prediction: from the Taylor model to the advanced Lamel model. Int. J. Plasticity 21, 589–624.

Humphreys F. J. and Hatherly M. (1996). Recrystallization and related annealing phenomena, Pergamon.

Humphreys F. J. (1997). A unified theory of recovery, recrystallisation and grain growth, based on the stability and growth of cellular microstructures II - The effect of second-phase particles, Acta Mater. 45, 5031-5039.

Huper, T., Endo, S., Ishikawa, N., Osawa, K. (1999). Effect of Volume Fraction of Constituent Phases on the Stress-Strain Relationship of Dual Phase Steels, ISIJ Int. 39, 288-294.

Hurley, P. J., Muddle, B. C. and Hodgson, P. D. (2002). The production of ultrafine ferrite during hot torsion testing of a 0.11 wt pct C steel. Metallurgical and Materials Transactions A, 33, 2985-2993.

Iacoviello, F., Di Bartolomeo, O., Di Cocco, V., Piacente, V. (2008). Damaging micromechanisms in ferritic–pearlitic ductile cast irons. Mater. Sci. Eng. A, 478, 181-186.

Ishikawa, N., Parks, D. M., Socrate, S., Kurihara, M. (2000). Micromechanical Modeling of Ferrite–Pearlite Steels Using Finite Element Unit Cell Models. ISIJ Int. 40, 1170-1179.

ISSB (2008), Iron and Steel Statistics Bureau, http://www.issb.co.uk.

Khaleel M. A., Zbib H. M. and Nyberg E. A. (2001). Constitutive modelling of deformation and damage in superplastic materials, Int. J. Plasticity 17, 277-296.

Kocks U. F. (1976). Laws for work hardening and low-temperature creep. J. Eng. Mater. Techn. 98, 76-85.

Kocks U. F. and Mecking H. (2003). Physics and phenomenology of strain hardening: the FCC case, Prog. Mater. Sci. 48, 171-273.

Krajcinovic, D. (2000). Damage mechanics: accomplishments, trends and needs, J. Solids and Structure, 37, 267-277.

Kumanin, V. I., Kovaleva, L. A. and Sokolova, M. L. (1995). The use of recovery heat treatment to eliminate damage in metallic materials, Metalloved. Term. Obrab. Met., 4, 7–12.

Kwiecinski J. and Wyrzykowski J. W. (1993). The effect of recovery annealing after small plastic deformations on the yield strength of polycrystalline aluminium, Acta Metall. Mater. 41, 3089-3095.

Lemaitre, J. (1984). How to use damage mechanics. Nuclear Engineering and Design, 80, 233-235.

Lemaitre, J. (1985). A continuous damage mechanics model for ductile fracture. Journal of Engineering Materials and Technology, 107, 83-89.

Le Roy, G., Embury, J. D., Edwards, G. and Ashby, M. F. (1981). A model of ductile fracture based on the nucleation and growth of voids. Acta Metallurgica, 29, 1509-1522.

Li B., Lin J. and Yao X. (2002). A novel evolutionary algorithm for determining unified creep damage constitutive equations, Int. J. Mech. Sci. 44, 5987-1002.

Li, S., Hoferlin, E., Bael, A.V., Houtte, P.V. and Teodosiu, C. (2004). Finite element modeling of plastic anisotropy induced by texture and strain-path change. Int. J. Plasticity 20, 915–936.

Li, Z., Steinmann, P. (2006). RVE-based studies on the coupled effects of void size and void shape on yield behaviour and void growth at micron scales. Int. J. Plasticity, 22, 1195-1216.

Lin J., Foster A. D., Liu Y., Farrugia D. C. J. and Dean T. A. (2007). On micro-damage in hot metal working. Part 2: Constitutive modelling. Engineering Transactions, 55, 1-18.

Lin, J. and Yang, J. (1999). GA-based multiple objective optimisation for determining viscoplastic constitutive equations for superplastic alloys, Int. J. Plasticity 15, 1181-1196.

Lin, J., Liu, Y., Farrugia, D. C. J. and Zhou, M. (2005). Development of dislocation-based unified material model for simulating microstructure evolution in multipass hot rolling , Philos. Mag. 85, 1967-1987.

Lin, J. and Liu, Y. (2005). A set of unified constitutive equations for modelling microstructure evolution in hot deformation, J. Mater. Proce. Tech. 143, 281-285.

Liu, Y. (2004). Characterisation of microstructure and damage evolution in hot deformation. Manufacturing and Mechanical Engineering, University of Birmingham.

Liu Y., Foster A. D., Lin J., Farrugia D. C. J. and Dean T. A. (2006). On micro-damage in hot metal working. Part 1: Experimental investigation. Engng. Trans., 54, 4, 271-287.

Liu, Y., Lin, J., Farrugia D. C. J. and Dean T. A. (2005). A numerical and experimental study of cavitation in a hot tensile axisymmetric testpiece. Journal of Strain Analysis, 40, 571-586.

Majta J. and Zurek A. K. (2003). Modelling of ferrite structure after deformation in the two-phase region, Int. J. Plasticity 19, 707-730.

Martínez-de-Guerenu A., Arizti F., Díaz-Fuentes M. and Gutiérrez I. (2004 (a)). Recovery during annealing in a cold rolled low carbon steel. Part I: Kinetics and microstructure characterization, Acta Mater. 52, 3657-3664.

Martínez-de-Guerenu A., Arizti F. and Gutiérrez I. (2004 (b)). Recovery during annealing in a cold rolled low carbon steel. Part II: Modelling the kinetics, Acta Mater. 52, 3665-3670.

Marx V., Reher F. R. and Gottstein G. (1999). Simulation of primary recrystallization using a modified three-dimensional cellular automaton, Acta Mater 47, 1219-1230.

Mayama, T. K., Sasaki and Ishikawa H. (2007). A constitutive model of cyclic viscoplasticity considering changes in subsequent viscoplastic deformation due to the evolution of dislocation structures, Int. J. Plasticity 23, 915-930.

McClintock, F. A. (1968). A criterion for ductile fracture by the growth of holes. Journal of Applied Mechanics, 35, 363-371.

Mori, T., Tanaka, K. (1973). Average stress in matrix and average elastic energy of materials with misfitting inclusions, Acta Metall. 21, 571-574.

Nakamachi, E., Hiraiwa, K., Morimoto, H., Harimoto, M. (2000). Elastic/crystalline viscoplastic finite element analyses of single- and poly-crystal sheet deformations and their experimental verification, International Journal of Plasticity 16, 1419-1441.

Needleman, A. (1987). A continuum model for void nucleation by inclusion debonding. J. Applied Mechanics, 54, 525-531.

Needleman, A. and Tvergaard, V. (1984). An analysis of ductile rupture in notched bars. Journal of Mechanics and Physics of Solids, 32, 461.

Nes, E. (1998). Modelling of work hardening and stress saturation in FCC metals. Process in Materials Science 41, 129-193.

Ohata, M., Toyoda, M. (2004). Damage concept for evaluating ductile cracking of steel structure subjected to large-scale cyclic straining. Sci. Tech. Adv. Mat. 5, 241-249.

Okabe, A., Boots, B., Sugihara, K. (1992). Spatial Tessellations: Concepts and Applications of Voronoi Diagrams, New York.

Pardoen, T., Hutchinson, J. W. (2000). An extended model for void growth and coalescence. J. Mechanics and Physics of Solid, 48, 2467-2512.

Penny, R. K. and Marriott, D. L. (1995). Design of Creep, London, Chapman & Hall.

Priestner R. and Ibraheem A. K. (2000). Processing of steel for ultrafine ferrite grain structures, Mater. Sci. Tech. 16, 1267-1272.

Prior, A. M. (1994). Applications of implicit and explicit finite element techniques to metal forming. Jounal of Materials Processing Technology, 45, 649-656.

Riesch-Oppermann, H. (1999). Generation of 2-D random poisson-Voronoi mosaics as framework for the micromechamical modelling of polycrystalline materials. Report FZKA 6325, Karlsruhe, Germany.

Rice J. R. and Tracey D. M. (1969). On the ductile enlargement off voids in triaxial stress fields, J. Mech. Phys. Sol. 17, 201-217.

Rojek, J., Zienkiewicz, O. C., Oñate, E. and Postek, E. (2001). Advances in FE explicit formulation for simulation of metalforming processes. Journal of Materials Processing Technology, 119, 41-47.

Rudiono, Y., Tomota (1997). Application of the secant method to prediction of flow curves in multi-microstructure steels, Acta Mater. 45, 1923-1929.

Sakai, T. and Jonas, J. J. (1984). Overview no. 35 Dynamic recrystallization: Mechanical and microstructural considerations. Acta Metall. 32, 189-209.

Sandström, R. and Lagneborg, R. (1975). A model for hot working occurring by recrystallization, Acta Metall. 23, 387-398.

Sellars, C. M. (1980). The Physical Metallurgy of Hot Working. Hot Working and Forming Processes [Proc. Conf.], Sheffield, England, 3-15.

Sellars, C. M. (1990). Modelling microstructural development during hot rolling. Materials Science and Technology, 15, 1072-1081.

Sevillano, J. G., Houtte, P. and Aernoudt, E. (1980). Large strain work hardening and textures. Prog. Mater. Sci. 25, 69-134.

Shapiro, E. and Dieter, G. (1970). High temperature-high strain rate fracture of inconel 600. Metall. Trans., 1, 1711–1719.

Shikanai, N., Kagawa, H., Kurihara, M. (1992). Influence of Microstructure on Yielding Behavior of Heavy Gauge High Strength Steel Plates. ISIJ Int. 32, 335-342.

Socrate, S., Boyce, M. C. (2000). Micromechanics of toughened polycarbonate. J. Mech. Phys. Solids 48, 233-273.

Srolovitz, D. J., Grest, G. S., Anderson, M. P. and Rollett. A. D. (1988). Computer simulation of recrystallization — II. Heterogeneous nucleation and growth, Acta Metall, 36, 2155-2128.

Stoyan, D., Kendall, W.S., Mecke, J. (1987). Stochastic geometry and its application, New York.

Thomason, P. F. (1990). Ductile fracture of metals. Pergamon Press, Oxford.

Tinet, H., Klöcker, H. and Le Coze, J. (2004). Damage analysis during hot deformation of a resulfurised stainless steel. Acta Materialia, 52, 3825-3842.

Tomota, Y., Kuroki, K., Mori, T., Tamura, I. (1976). Tensile deformation of two-ductile-phase alloys: Flow curves of α-γ Fe---Cr---Ni alloys, Mater. Sci. Eng. 24, 85-94.

Trivedi, P., Field, D.P. and Weiland, H. (2004). Alloying effects on dislocation substructure evolution of aluminum alloys. Int. J. Plasticity 20, 459–476.

Tvergaard, V. (1981). Influence of voids on shear band instabilities under plane strain conditions. Int. J. Fract. 17, 389–407.

Tvergaard, V. (1982). On localization in ductile materials containing spherical voids. Int J Fract., 18, 237-52.

Tvergaard, V. (1990). Material failure by void growth to coalescence. Adv. App. Mech., 27, 83-147.

Tvergaard, V. and Needleman, A. (2001). The modified Gurson model. Handbook of Materials Behavior Models. London, Academic Press.

Uenishi, A. and Teodosiu, C. (2004). Constitutive modeling of the high strain rate behaviour of interstitial-free steel. Int. J. Plasticity, 20, 915–936.

Wei, D., Han, J., Tieu, A.K. and Jiang, Z.Y. (2004). An analysis on the inhomogeneous microstructure in steel crack healing area, Key Eng. Mater. 274–276, 1053–1058.

Wei, D., Han, J., Jiang, Z.Y., Lu, C. and Tieu, A.K. (2006). A study on crack healing in 1045 steel, J. Materials Processing Technology, 177, 233-237.

Wen S. W., Hilton P. and Farrugia D. C. J. (1999). Finite Element Modelling of a Submerged Arc Welding Process, Proceedings of the Inter. Conf. on Advances in Materials and Processing Technologies, 737-746.

Weyer, S., Fröhlich, A., Riesch-Oppermann, H., Cizelj, L. and Kovac, M. (2002). Automatic finite element meshing of planar Voronoi tessellations. Eng. Fract. Mech. 69, 945–958.

Wilsdorf, H.G. F. (1983). The ductile fracture of metals: A microstructural viewpoint, Mater. Sci. Eng. 59, 1-39.

Zhang, J. and Jiang, Y. (2005). An experimental investigation on cyclic plastic deformation and substructures of polycrystalline copper. Int. J. Plasticity 21, 2191–2211.

Zhang, P., Lee, H. (1993). Creep damage and fracture at high temperature. Eng. Fract. Mech., 44, 283-288.

Zhao, X., Guest R. P., Tin S., Cole D, Brooks J. W. and Peers M. (2004). Modelling hot deformation of Inconel 718 using state variables. Mater. Sci. Tech. 20, 1414-1420.

Zhu, H. X., Thorpe, S. M., Windle, A. H. (2001). The geometrical properties of irregular two-dimensional Voronoi tessellations. Philosophical magazine A, 81, 2765-2783.

PUBLICATIONS

Li, H., Lin, J., Dean, T. A., Wen, S. W., Bannister, A. C. (2009). Modelling mechanical property recovery of a linepipe steel in annealing process. International Journal of Plasticity, 25, 1049-1065.

Li, H., Lin, J., Dean, T. A., Wen, S. W., Bannister, A. C. (2007). Modelling of damage reduction and microstructure evolution by annealing. Proceedings of the 10th ESAFORM conference, Zaragoza**,** ISBN: 978-0-7354-0414-4, pp303-308.